TURUN YLIOPISTON JULKAISUJA
ANNALES UNIVERSITATIS TURKUENSIS

SARJA - SER. A I OSA - TOM. 412

ASTRONOMICA - CHEMICA - PHYSICA - MATHEMATICA

MAGNETIC RESONANCE EXPERIMENTS WITH ATOMIC HYDROGEN

by

Janne Ahokas

TURUN YLIOPISTO
UNIVERSITY OF TURKU
Turku 2010

From

Wihuri Physical Laboratory
Department of Physics and Astronomy
University of Turku
Turku, Finland
and
National Graduate School in Nanoscience
Jyväskylä, Finland

Supervised by

Docent Sergei Vasiliev
Wihuri Physical Laboratory
Department of Physics and Astronomy
University of Turku
Turku, Finland

Reviewed by

Prof. Matti Krusius
Low Temperature Laboratory
Aalto University
Finland

Prof. Leonid P. Mezhov-Deglin
Institute of Solid State Physics
Russian Academy of Sciences
Chernogolovka, Russia

Opponent

Prof. Nicholas P. Bigelow
Department of Physics and Astronomy
University of Rochester
Rochester, New York
United States of America

ISBN 978-951-29-4408-8 (PRINT)
ISBN 978-951-29-4409-5 (PDF)
ISSN 0082-7002
Painosalama Oy - Turku, Finland 2010

Acknowledgments

This work has been carried out in the years 2006-2010 in the Wihuri Physical Laboratory at the Department of Physics and Astronomy of the University of Turku. National Graduate School in Nanoscience and Jenny and Antti Wihuri Foundation are acknowledged for financial support.

I want to express my sincere gratitude to my supervisor Docent Sergei Vasiliev for his constant support and guidance and for teaching me most I know of low temperature experiments. To Profs. Reino Laiho and Kalle-Antti Suominen I am grateful for support throughout the work.

I wish to thank Docent Simo Jaakkola for giving me the opportunity as a young student to work in the group and for the comments and critical review of the thesis. I would also like to thank my past and present colleagues Dr. Jarno Järvinen, Dr. Steffen Novotny and M.Sc. Otto Vainio for their contributions and for the pleasant working environment. In addition, I want to thank our collaborators Prof. D. M. Lee, Dr. V. V. Khmelenko and Prof. G. V. Shlyapnikov.

Technical staff of the University had also a role in making this work possible. Especially the contributions of Mr. Timo Haili in making components for experimental apparatuses and Mr. Esa Lilja in providing helium are highly valued.

I am deeply grateful to my family for the encouragement and support I have always received. Also, thank you all my friends who made my studying years unforgettable.

And finally, I want to thank my beloved wife Mia for her love and care during these years.

Turku, October 2010

Janne Ahokas

Abstract

In this thesis three experiments with atomic hydrogen (H) at low temperatures $T < 1\,\mathrm{K}$ are presented. Experiments were carried out with two- (2D) and three-dimensional (3D) H gas, and with H atoms trapped in solid H_2 matrix. The main focus of this work is on interatomic interactions, which have certain specific features in these three systems considered. A common feature is the very high density of atomic hydrogen, the systems are close to quantum degeneracy. Short range interactions in collisions between atoms are important in gaseous H. The system of H in H_2 differ dramatically because atoms remain fixed in the H_2 lattice and properties are governed by long-range interactions with the solid matrix and with H atoms.

The main tools in our studies were the methods of magnetic resonance, with electron spin resonance (ESR) at 128 GHz being used as the principal detection method. For the first time in experiments with H in high magnetic fields and at low temperatures we combined ESR and NMR to perform electron-nuclear double resonance (ENDOR) as well as coherent two-photon spectroscopy. This allowed to distinguish between different types of interactions in the magnetic resonance spectra. Experiments with 2D H gas utilized the thermal compression method in homogeneous magnetic field, developed in our laboratory. In this work methods were developed for direct studies of 3D H at high density, and for creating high density samples of H in H_2.

We measured magnetic resonance line shifts due to collisions in the 2D and 3D H gases. First we observed that the cold collision shift in 2D H gas composed of atoms in a single hyperfine state is much smaller than predicted by the mean-field theory. This motivated us to carry out similar experiments with 3D H. In 3D H the cold collision shift was found to be an order of magnitude smaller for atoms in a single hyperfine state than that for a mixture of atoms in two different hyperfine states. The collisional shifts were found to be in fair agreement with the theory, which takes into account symmetrization of the wave functions of the colliding atoms. The origin of the small shift in the 2D H composed of single hyperfine state atoms is not yet understood. The measurement of the shift in 3D H provides experimental determination for the difference of the scattering lengths of ground state atoms.

The experiment with H atoms captured in H_2 matrix at temperatures below

1 K originated from our work with H↓ gas. We found out that samples of H in H_2 were formed during recombination of gas phase H, enabling sample preparation at temperatures below 0.5 K. Alternatively, we created the samples by electron impact dissociation of H_2 molecules *in situ* in the solid. By the latter method we reached highest densities of H atoms reported so far, $3.5(5) \times 10^{19}\,\mathrm{cm}^{-3}$. The H atoms were found to be stable for weeks at temperatures below 0.5 K. The observation of dipolar interaction effects provides a verification for the density measurement. Our results point to two different sites for H atoms in H_2 lattice. The steady-state nuclear polarizations of the atoms were found to be non-thermal. The possibility for further increase of the impurity H density is considered. At higher densities and lower temperatures it might be possible to observe phenomena related to quantum degeneracy in solid.

Preface

This thesis is based on a series of experiments carried out during the years 2005-2009 and eight original papers listed below.

P1. J. Ahokas, J. Järvinen, and S. Vasiliev, Cold collision frequency shift in two-dimensional atomic hydrogen, Phys. Rev. Lett. **98**, 043004 (2007).

P2. J. Ahokas, J. Järvinen, and S. Vasiliev, Magnetic resonance studies of cold atomic hydrogen gas, J. Low Temp. Phys. **150**, 577 (2008).

P3. J. Ahokas, J. Järvinen, G. V. Shlyapnikov, and S. Vasiliev, Clock shift in high field magnetic resonance of atomic hydrogen, Phys. Rev. Lett. **101**, 263003 (2008).

P4. J. Ahokas, J. Järvinen, G. V. Shlyapnikov, and S. Vasiliev, A reply to the comment by A. I. Safonov *et al.*, Phys. Rev. Lett. **104**, 099302 (2010).

P5. J. Ahokas, O. Vainio, S. Novotny, J. Järvinen, and S. Vasiliev, Magnetic resonance line shifts in the quantum gas of atomic hydrogen, Phys. Scr. T **140** (2010) 014012.

P6. J. Ahokas, J. Järvinen, V. V. Khmelenko, D. M. Lee, and S. Vasiliev, Exotic behavior of hydrogen atoms in solid H_2 at temperatures below 1 K, Phys. Rev. Lett. **97**, 095301 (2006).

P7. J. Ahokas, O. Vainio, J. Järvinen, V. V. Khmelenko, D. M. Lee, and S. Vasiliev, Stabilization of high density atomic hydrogen in H_2 films at $T < 0.5\,\mathrm{K}$, Phys. Rev. B **79**, 220505(R) (2009).

P8. J. Ahokas, O. Vainio, S. Novotny, J. Järvinen, V. V. Khmelenko, D. M. Lee, and S. Vasiliev, Magnetic resonance study of H atoms in thin films of H_2 at temperatures below 1 K, Phys. Rev. B **81**, 104516 (2010).

Other publications not included in this thesis:

Ref. [26] J. Järvinen, J. Ahokas, S. Jaakkola, and S. Vasilyev, Three-body recombination in two-dimensional atomic hydrogen gas, Phys. Rev. A **72**, 052713 (2005).

Ref. [12] J. Järvinen, J. Ahokas, and S. Vasiliev, Thermal compression of atomic hydrogen on helium surface, J. Low Temp. Phys. **147**, 579 (2007).

My contribution to the papers is following:

P1, P2 I took part in making modifications to the existing experimental cell. I made part of the experiments and analyzed most of the data.

P3, P4, P5 I was responsible for the design, assembly and testing of the new experimental cell. I made part of the experiments and analyzed most of the data.

P6 I took part in making modifications to the existing experimental cell. I made the ENDOR, nuclear relaxation and stability measurements, and analyzed the data.

P7, P8 I was responsible for the assembly and testing of the new experimental cell. I made most of the experiments and simulations, analyzed the data, and prepared the manuscripts.

Contents

Chapter 1

Background

1.1 Introduction

Hydrogen is the most abundant element in the universe. Being the lightest and simplest element, understanding the properties of hydrogen atom (H) had a significant role in the development of quantum physics. On earth, however, hydrogen atoms are usually bound to molecules. Hydrogen can be found in atomic state in vast interstellar clouds in space, but at very small densities of few atoms per cubic centimeter. Atomic hydrogen can be produced by electric discharge in molecular hydrogen (H_2), but the atoms typically quickly recombine into H_2 molecules, resulting in a short lifetime of the H gas. Because of its high reactivity, a very basic application of hydrogen has been a source of chemical energy. Burning (oxidation) of H_2 is the simplest example. However, because the chemical energy per mass unit obtained in recombination of H is even larger, it motivated attempts to stabilize large quantities of H. Later properties of H at low temperatures became a prime interest, which was motivated by the possibility of observing Bose-Einstein condensation (BEC) in a weakly interacting H gas.

In general, two different methods have been employed to obtain stable and high density atomic hydrogen: matrix isolation and spin-polarization in the gas phase. Stabilization means here that the lifetime of the atoms is increased by several orders of magnitude enabling experiments from minutes to days. First, trapping and stabilizing H atoms in solid matrices at rather high concentrations was demonstrated in the late 1950's [1, 2, 3]. In the matrix isolation method the matrix prevents trapped species from approaching each other and recombining [4]. Generally low temperatures are required to prevent thermally activated motion of the trapped atoms. The temperature of liquid helium (4 K) suffices for H in H_2.

The possibility that atomic hydrogen could exist as stable gas was realized already in 1959 [5], but stabilization of gas phase H was achieved two decades later [6]. The method turned out to be more complicated than the matrix stabilization and required lower temperatures ($< 1\,\mathrm{K}$) and high magnetic fields. In such conditions the electron spins of the atoms are polarized and atoms interact

via the repulsive triplet potential which supports no bound states. The atoms must be confined in a container and thermal contact with walls provides cooling of the atoms. The choice of liquid helium as wall coating material turned out to be essential because H adsorbs and recombines far more effectively on other surfaces.

The experiments with spin-polarized H (H$\downarrow$) were motivated for a long time by the goal of observing BEC. However, BEC was first reached in alkali atom vapors in 1995 [7, 8] and only in 1998 in H$\uparrow$ [9]. In the same year evidence for the formation of a so-called quasi-condensate was observed in magnetically compressed two-dimensional (2D) H$\downarrow$ [10]. Since the magnetic compression method did not allow direct observation of 2D quantum degeneracy, experiments were continued with thermal compression [11, 12] which allows direct studies by magnetic resonance methods. In thermally compressed 2D H$\downarrow$ the phase space density has been a factor of two below the transition limit [12].

In this thesis experiments employing both methods to obtain high density of H are presented. The studies with 3D gas could be performed in different conditions: At low density the properties of H atoms are close to those for free (non-interacting) atoms, while at higher densities collisions become important. In the 2D system the density of H was even higher and the measurements can bring information on dimensionality effects. The highest densities of H atoms were achieved in the solid H_2 matrix. The behavior of H in H_2 differ dramatically because atoms do not experience collisions with each other and long-range interactions with the solid matrix and with H atoms dominate.

The chief interest in the experiments with 2D and 3D H$\downarrow$ were the measurements of line shifts due to atomic collisions. Similar shifts exist in atomic frequency standards where they have imposed the main limitation to the accuracy [13]. Compared to frequency standards we have much worse accuracy of determining the position of the atomic transition but our experiments are carried out at $\sim 6-8$ orders of magnitude higher density, typically in the collisional (hydrodynamic) regime. At low temperatures the collisional shift is commonly referred to as cold collision or clock shift (CS).

Our interest in the subject first arose from the experiments with 2D H$\downarrow$, where the cold collision shift appeared to be negligibly small [14]. Thus a special experiment was performed for an accurate determination of the shift [P1], confirming the previous conclusion. Motivated by the unexpected result, we performed similar experiments with 3D H$\downarrow$. As in the 2D case the shift was found to be negligible for atoms in single hyperfine state, but close to the expected value for a mixture of atoms in two different hyperfine states [P3]. This observation stimulated us to find the correct theoretical interpretation of the results [P3]. The 3D H$\downarrow$ measurement provided also experimental determination of the difference of the scattering lengths for ground state atoms.

The third experiment with H in H_2 originated from our work with H$\downarrow$ gas. In order to improve the stability of H$\downarrow$, the walls of experimental cell were typically coated by solid H_2 layer. Occasionally in experiments with 2D H we found that

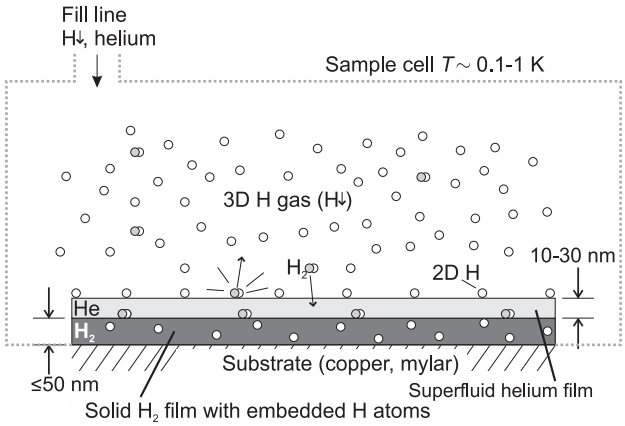

Figure 1.1: Illustrating H in different phases in the sample cell and the structure of the films covering the cell walls. H adsorbed on the helium surface forms a 2D gas which is in dynamic equilibrium with the 3D gas [15]. The H_2 molecules resulting from recombination penetrate through the helium film [16, 17] and create a layer of H_2 on the walls [12]. H atoms were found to get trapped in the H_2 film in the recombination process [18, P6, P8].

atoms are also captured in the H_2 film. Rather high concentrations of H in H_2 were obtained, which motivated us continuing the H in H_2 study. Since the experimental methods are nearly the same, it turned out to be possible to study H↓ gas and H in H_2 in the same sample cell. That is why both topics are combined in this thesis. The systems of gas phase H↓ and H in H_2 in the cell are illustrated in fig. 1.1.

The experiments with H in H_2 had two different goals. The first one was to study the properties of H atoms in H_2 at temperatures below 1 K which were previously not accessible. The second was to reach the highest possible density of H atoms in H_2 at low temperatures with the motivation of observing phenomena related to quantum degeneracy of atoms in solid [19]. The latter goal needs developments in the sample accumulation methods because a lot of excess heat is released in the present methods catalyzing recombination in the solid and hence limiting the maximum density.

The thesis is organized as follows: In chapter 1 basic properties of 3D and 2D H↓ gas are presented. Also a general introduction to magnetic resonance methods and on the experimental setup is provided. Chapter 2 contains a review of interactions that influence magnetic resonance experiments. In chapters 3 and 4 experiments with 2D and 3D H↓ are presented. A common introduction to these experiments is presented in sec. 2.2.3. Finally in chapter 5 experiments on H in H_2 are presented. Because the subjects of matrix isolation and quantum solids are somewhat different from quantum gases, chapter 5 contains its own introductory

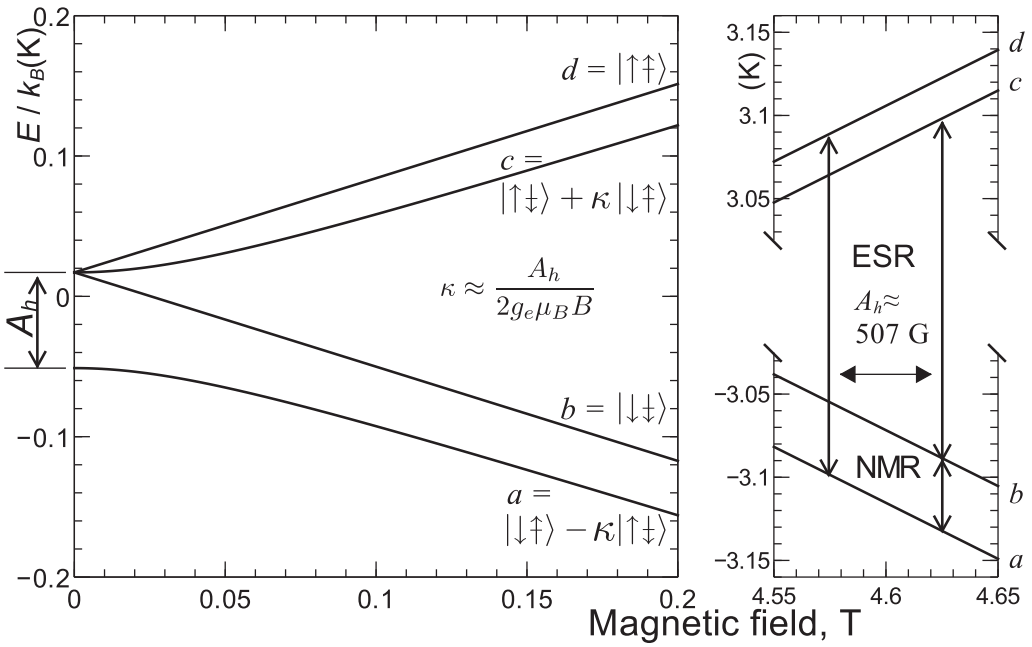

Figure 1.2: Hyperfine level diagram of atomic hydrogen in magnetic field. On the right-hand side the states in experimental fields are shown with the ESR and NMR transitions considered in these experiments. The arrows (↑, ↓) denote the directions of the electron and nuclear spins.

part. The eight original publications are attached.

1.2 Properties of hydrogen atom in magnetic field

In this thesis we study atomic hydrogen in its electronic ground state. The spin part of the Hamiltonian for H atom in an external magnetic field $\mathbf{B}$ is given by

$$\hat{H} = g_e \mu_B \mathbf{S} \cdot \mathbf{B} - g_n \mu_n \mathbf{I} \cdot \mathbf{B} + A_h \mathbf{S} \cdot \mathbf{I}, \tag{1.1}$$

where g_e and μ_B are the g-factor and Bohr magneton for the electron, g_n and μ_n are the respective quantities for the nucleus and A_h is the hyperfine coupling constant. The first and second terms are the Zeeman interaction terms for the electron and the nucleus, and the third term is the hyperfine interaction between the electron and the nucleus.

One obtains four energy eigenstates for the Hamiltonian (1.1), often referred to as the hyperfine states. In zero magnetic field the states labeled as b, c and d are degenerate, separated from the state a by the energy A_h due to the hyperfine interaction. The Zeeman interaction lifts the degeneracy, as shown in fig. 1.2. The

states a and c are mixed, containing the fraction $\kappa \approx A_h/2g_e\mu_B B$ of the opposite electron spin direction in the high field limit, while b and d are "pure" states. The allowed transitions in high fields are the electron spin flip transitions $a-d$ and $b-c$, and the nuclear spin flip transitions $a-b$ and $c-d$. The transitions relevant to this work are shown in fig. 1.2.

Because H atoms in the electron spin-down states a and b (H$\downarrow$) are attracted to high magnetic field, while the spin-up states c and d (H$\uparrow$) are repelled from it, it is possible to accumulate H$\downarrow$ to a region of high magnetic field. At the temperature of $T = 0.5\,\mathrm{K}$ and $B = 4.6\,\mathrm{T}$, the fraction of atoms in the electron spin-up state is $n\,(\mathrm{H}\uparrow)\,/n\,(\mathrm{H}\downarrow) \approx \exp\left(-2\mu_B B/k_B T\right) \sim 10^{-10}$, rapidly decreasing with decreasing temperature. Because a maximum of static magnetic field cannot be created in free space, a sample accumulated to high field must be confined by physical walls. Interaction between H and He is weak enough so that at temperatures down to 100 mK it is possible to stabilize H$\downarrow$ gas in a chamber with walls covered by liquid helium for a time of several minutes to several hours.

1.3 High density nearly degenerate systems of H atoms

We consider atomic hydrogen in three different environments:

1. 3D H gas confined by the walls of an experimental chamber at densities $10^{12} - 10^{18}\,\mathrm{cm}^{-3}$,

2. 2D H gas adsorbed on the surface of liquid helium at densities $10^{11} - 5 \times 10^{12}\,\mathrm{cm}^{-2}$,

3. H atoms captured in solid H_2 matrix at densities $10^{17} - 3.5 \times 10^{19}\,\mathrm{cm}^{-3}$.

The main characteristic feature of all these systems is the very high density of H atoms, more than three orders of magnitude higher than in any experiment with cold alkali vapors. In our temperature regime of 70-500 mK the thermal velocities of H atoms are of the order $v_{th} \sim 5 \times 10^3\,\mathrm{cm/s}$. At low density ($\lesssim 10^{16}\,\mathrm{cm}^{-3}$) the atoms mainly collide with walls of the sample cell, while at our highest densities atoms collide frequently with each other. Interactions with the walls and with each other sway the properties of atoms in the 3D and 2D gases. In contrast, in the system of H in H_2 atoms are isolated from one another by the H_2 lattice and remain rather stationary moving only via quantum tunneling. Hence weaker long range interactions of the atoms between each other and with the solid matrix govern.

We characterize the properties of H atoms in different environments by the following quantities (table 1.1):

- Mean distance between atoms $\bar{r} = n^{-1/3}$ (or $\sigma^{-1/2}$). n and σ are the volume and the surface densities.

Table 1.1: Characteristic quantities for comparison of H atoms in different environments. For the symbols see the text.

System	Density	$\bar{r}$	$\bar{l}$	$\bar{l}_{ex}$	ϖ	$\lvert\Delta B_{dip}\rvert$
3D H gas	$10^{12}\,\mathrm{cm}^{-3}$	$1\,\mu$m	16 m	0.2 m	10^{-8}	10^{-7} G
(0.4 K)	$10^{18}\,\mathrm{cm}^{-3}$	10 nm	$16\,\mu$m	200 nm	0.02	0.1 G
2D H gas	$10^{11}\,\mathrm{cm}^{-2}$	32 nm	$4\,\mu$m	200 nm	0.03	0.07 G
(0.1 K)	$5\times10^{12}\,\mathrm{cm}^{-2}$	5 nm	70 nm	4 nm	1.6	4 G
H in H_2	$5\times10^{17}\,\mathrm{cm}^{-3}$	13 nm	-	-	$10^{-5}-10^{-2}$	0.04
(0.1 K)	$3.5\times10^{19}\,\mathrm{cm}^{-3}$	3.1 nm	-	-	$0.01-0.9$	2 G

- Scattering length characterizing interatomic interaction: $a_t \approx 0.7\,$Å for triplet, $a_s \approx 0.25\,$Å for singlet [20].
- Thermal de Broglie wavelength $\lambda_{th} = \left(2\pi\hbar^2/mk_BT\right)^{1/2} \approx 1.74\,\mathrm{nm{\cdot}K}^{1/2}/\sqrt{T}$. One can expect quantum effects to manifest when $\lambda_{th} \gg a$, *i.e.* at the quantum gas limit. When $\lambda_{th} \geq \bar{r}$ the system is quantum degenerate ($\varpi \geq 1$, see below).
- Mean free path for elastic collisions $\bar{l} \approx (n\xi)^{-1}$ (2D: $(\sigma 4a)^{-1}$). Here ξ is the scattering cross section $\xi \approx 4\pi a^2$ with the scattering length $a_t \approx 0.7\,$Å [20, 21].
- Mean-free path for spin-changing collisions $\bar{l}_{ex} \approx \left(n\pi\lambda_{th}^2/4\right)^{-1}$ (2D: $(\sigma\lambda_{th})^{-1}$).
- Quantum degeneracy parameter $\varpi = n\lambda_{th}^3$ (2D: $\sigma\lambda_{th}^2$). BEC occurs in uniform non-interacting 3D gas when $\varpi \approx 2.612$. In 2D Bose gas the Berezinskii-Kosterlitz-Thouless (BKT) transition to superfluid occurs when $\sigma\lambda_{th}^2 = 4$. Formation of a quasi-condensate in 2D H↓ was observed at $\varpi > 3$ [10]. In the case of H in H_2 the effective mass $m^\star \sim \hbar^2/c^2\Delta$ was used to estimate λ_{th} [P7]. Here Δ is the bandwidth of the tunneling motion $\Delta/k_B = 0.01 - 1\,$K [22] and $c = 0.379\,$nm is the lattice constant for H_2 [23].
- Physical size of the sample $L \approx 0.1 - 5\,$cm (3D H↓).
- Average dipolar field ΔB_{dip} in the samples reflects the strength of dipolar interactions. Evaluation of the dipolar field for 3D and 2D H↓ is presented in sec. 2.3.2, and for H in H_2 in sec. 5.5.3 [P8].

With 3D H gas our experiments covered a density range of six orders of magnitude. At $n < 10^{16}\,\mathrm{cm}^{-3}$ the mean free path $\bar{l}$ is $> 1\,$cm, thus atoms are in the collisionless regime. However for $\bar{l}_{ex} \ll L$ spin-changing collisions occur and may lead to spin transport. At $n \gtrsim 5\times10^{16}\,\mathrm{cm}^{-3}$ and $\bar{l} < 0.2\,$cm atoms undergo several collisions during the time between wall collisions and H-H interactions influence the magnetic resonance experiments. The 2D H system is even more dense, with $\bar{l} \lesssim 7\,\mu$m. The smallest mean interatomic distance $\bar{r} \gtrsim 3.1\,$nm is for H in H_2.

1.4 Adsorption of atomic hydrogen on helium surface

Experiments with H↓ gas are performed in a sample cell with its inner surfaces covered by liquid helium film. The interaction potential of H on helium surface is rather steep, with the minimum of 4 K [24]. There exist a single bound state of H on both ^{4}He and ^{3}He surfaces with binding energies $E_a/k_B = 1.14(1)\,\mathrm{K}$ for ^{4}He and $E_a/k_B = 0.39\,\mathrm{K}$ for ^{3}He [25, 26]. Such a weak binding is however large enough to increase the surface density of H strongly. At $T \to 0$ practically all H is adsorbed on He surface. A review of 2D H↓ is given in ref. [24].

The adsorbed H atoms can move freely along the helium surface, representing the most natural realization of a two-dimensional gas [24]. However, the adsorbed gas is not strict two-dimensional due to the quantum delocalization of atoms in the direction perpendicular to the surface [24]. The delocalization defines an effective "thickness" of the gas, given by $l_d = \sqrt{\hbar^2/mE_a}$, which yields 0.5 nm for ^{4}He surface. The ratio of l_d to the scattering length $a \approx 0.07\,\mathrm{nm}$ is $l_d/a \approx 7$, implying that the scattering between atoms can be treated practically as three-dimensional. Then the surface density σ can be transformed to an effective volume density n by the relation $n = \sigma/l_d$. Using such a scaling approach many properties of 2D gas can be evaluated from those for 3D gas [27, 28]. However, this approach has been questioned [26, 29].

The adsorbed H↓ gas is in dynamic equilibrium with the bulk gas. Continuous exchange of atoms between the bulk and surface-adsorbed phases takes place at a rate depending exponentially on temperature [24]. In the classical regime, the surface density is given by the well-known adsorption isotherm [24, 30]

$$\sigma = \left(\frac{T_{3D}}{T_{2D}}\right)^{\frac{3}{2}} n\lambda_{th} \exp\left(\frac{E_a}{k_B T_{2D}}\right). \tag{1.2}$$

The prefactor $(T_{3D}/T_{2D})^{3/2}$ takes into account a possible temperature difference between the bulk (T_{3D}) and and adsorbed gases (T_{2D}).

The surface residence time is given by

$$\tau_a = \frac{2\pi\hbar}{s k_B T_{2D}} \exp\left(\frac{E_a}{k_B T_{2D}}\right), \tag{1.3}$$

where $s \approx 0.33 \times T_{2D}\,\mathrm{K}^{-1}$ is the sticking probability [24]. At high densities and low temperatures one has to take into account corrections due to quantum correlation effects and H-H interaction energy in eqs. (1.2) and (1.3) [30].

Due to the exponential temperature dependence of the surface density, it is possible to obtain a large increase in the surface density on a so-called cold spot on the wall of sample cell. However, the surface gas temperature will be higher than the surface temperature due to incomplete thermal accommodation of the adsorbed atoms and heat released by recombination and one cannot directly use eq. (1.2) to obtain σ. In some of our experiments the bulk and surface densities

n and σ could be measured independently enabling determination of T_{2D} from eq. (1.2) [12]. The method of thermal compression was first put into practice by Matsubara *et al.* [31].

The experiments presented here extend to the limit of 2D quantum degeneracy $\sigma\lambda_{th}^2 \approx 1$ which is reached at 100 mK for $\sigma \approx 3\times10^{12}\,\mathrm{cm}^{-2}$. The highest densities reached in the thermal compression experiments were $5\times10^{12}\,\mathrm{cm}^{-2}$, corresponding to $\sigma\lambda_{th}^2 \approx 1.6$ [26, 12]. We have not observed yet any signs of quantum degeneracy, and that is not discussed here.

1.5 Recombination of H↓ gas

Recombination of H atoms to H_2 molecules is the main obstacle in obtaining H↓ gas at high density. In our experiments with 3D and 2D H↓ several different recombination and relaxation mechanisms are operative, but here we outline the most important ones only. A review of recombination and relaxation processes in H↓ can be found in ref. [15].

In order to form a molecule, two atoms must interact via the singlet potential. Because the probability for recombination with emission of radiation is negligible, a third body is required for the conservation of energy and momentum [15] and recombination proceeds via the reaction

$$\mathrm{H{+}H{+}X} \rightarrow \mathrm{H_2{+}X}. \tag{1.4}$$

In 3D gas the third body X can be a H or He atom, while in the adsorbed phase helium surface plays the role. Our experiments are carried out at temperatures below 0.6 K where the vapor density of helium is negligible. Generally at temperatures below 300 mK and at densities less than about $10^{17}\,\mathrm{cm}^{-3}$ recombination mainly occurs on surfaces, while at higher densities and temperatures recombination in 3D becomes significant.

In electron spin-polarized gas (H↓) consisting of a and b atoms, two-body recombination occurs in $a+a$ and $a+b$ collisions because of the finite probability of a-state atoms being in opposite electron spin state (cp. fig. 1.2). Therefore, the recombination rate constants K_{aa} and K_{ab} depend on the magnetic field as $\propto \kappa^2$ [15]. In addition, the $a+b$ rate constant K_{ab} decreases as a function of decreasing temperature because it produces *ortho*-H_2 with odd angular momentum, and consequently the atoms must overcome a centrifugal barrier [15, 25]. The $a+a$ recombination leads to the *para*-H_2. Due to the preferential recombination of a-state atoms, an unpolarized ("equilibrium") sample tends to evolve to a doubly polarized, non-equilibrium state consisting only of b-state atoms ($K_{aa}/K_{ab} \approx 4$ at $T = 0.4\,\mathrm{K}$, $K_{aa}/K_{ab} \approx 10$ at $T = 0.1\,\mathrm{K}$ [25]). Because two-body recombination is rather fast, maximum densities which can be reached in nuclear spin-unpolarized gas are relatively low and recombination mainly occurs on surfaces. An attempt to increase the density of such gas leads to rapid recombination.

In doubly polarized gas H$\downarrow\downarrow$ two-body recombination is inhibited, but recombination may occur in $b + b + b$ three-body collisions. It rapidly increases with density, operates both in the bulk and surface phases, and presents therefore the main limitation to the highest achievable densities.

Also electron and nuclear relaxation processes occur in H$\downarrow$. The electron spin relaxation is thermally activated and can be neglected at $\lesssim 0.5\,\mathrm{K}$, but it may lead to a thermal runaway ("explosion") in compressions of 3D H$\downarrow$ when the gas becomes strongly overheated by the recombination [32]. Due to the preferential recombination of a-state atoms, nuclear relaxation $b \to a$ is also responsible for recombination in H$\downarrow\downarrow$ gas. Two different relaxation processes may occur in experiments: impurity induced one-body relaxation and two-body dipolar relaxation [15]. The former takes place on surfaces and can be reduced to a negligible level by careful preparation of the experimental cell and insulating its possible magnetic impurities from the H$\downarrow\downarrow$ gas with coating of the surfaces by an solid H_2 layer [33, 12]. The two-body relaxation may occur both on surfaces and in bulk H$\downarrow$. Due to the anisotropy of dipolar interaction, the two-body relaxation rate is zero for surfaces perpendicular to the polarizing magnetic field [15].

1.6 Magnetic resonances in hydrogen atom

Because H atom has both electron and nuclear spin, electron spin resonance (ESR) and nuclear magnetic resonance (NMR) are apparent choices to study H. Optical transitions lay in the far ultraviolet region, so that utilizing them for diagnostics is technically difficult. In our magnetic resonance experiments the specific features of H are full electron spin-polarization, control of nuclear spin polarization and a wide range of densities.

For a hydrogen atom there are two allowed ESR transitions, $a-d$ and $b-c$, which are induced by a transverse excitation field. The possible NMR transitions are $a-b$ and $c-d$. The $a-c$ transition comprises simultaneous flip of both electron and nuclear spins, is induced by a longitudinal excitation field and is suppressed by a factor $\kappa^2 \sim 10^{-5}$ at 4.6 T, hence it is strongly forbidden in high magnetic fields. The $b-d$ transition is completely forbidden. However, the two forbidden transitions are allowed for two-photon absorption. The ESR and NMR transitions important in this work are shown in fig. 1.2.

The saturation and relaxation behavior of gas phase H$\downarrow$ differ from that of solid state systems like H in H_2, where the ESR excited atoms relax to thermal equilibrium due to spin-lattice interaction [34]. In the case of gas phase saturation is not reached because the ESR excited upper state (H$\uparrow$) atoms recombine rapidly. The ESR absorption is proportional to the excitation power as long as the ESR induced destruction does not essentially change the total density of H in the experimental chamber.

In the case of NMR the situation is more complicated because the lifetime and concentration of a-state atoms depend strongly on temperature. Because of the preferential recombination of a-state atoms, the sample typically evolves to the doubly polarized b-state. When the recombination of the a-state population is slow, it is possible to saturate the NMR transition and thus equalize the a and b populations. At rather high surface densities of $\sigma > 10^{11}\,\mathrm{cm}^{-2}$ the NMR induced a-state atoms are quickly removed due to preferential recombination and the saturation behavior resembles the ESR case (sec. 1.6.2).

1.6.1 Electron spin resonance

An ESR spectrum of H$\downarrow$ gas is presented in fig. 1.3. The two transitions correspond to the $a \to d$ (a-line) and $b \to c$ (b-line) transitions, separated by $A_h/g_e\mu_B \approx 507\,\mathrm{G}$.

The ESR resonance frequencies obtained from the Breit-Rabi equations [35] are

$$f_{bc} = -\frac{1}{2}\frac{A_h}{h} + \frac{1}{2}\frac{\mu^- B_{bc}}{h} + \frac{1}{2}\frac{\mu^+ B_{bc}}{h}\sqrt{1+\left(\frac{A_h}{\mu^+ B_{bc}}\right)^2} \tag{1.5}$$

$$\approx -\frac{1}{2}\frac{A_h}{h} + \frac{g_e\mu_B B}{h} + \left\{\frac{A_h^2}{4h\mu^+ B} - \ldots\right\}, \tag{1.6}$$

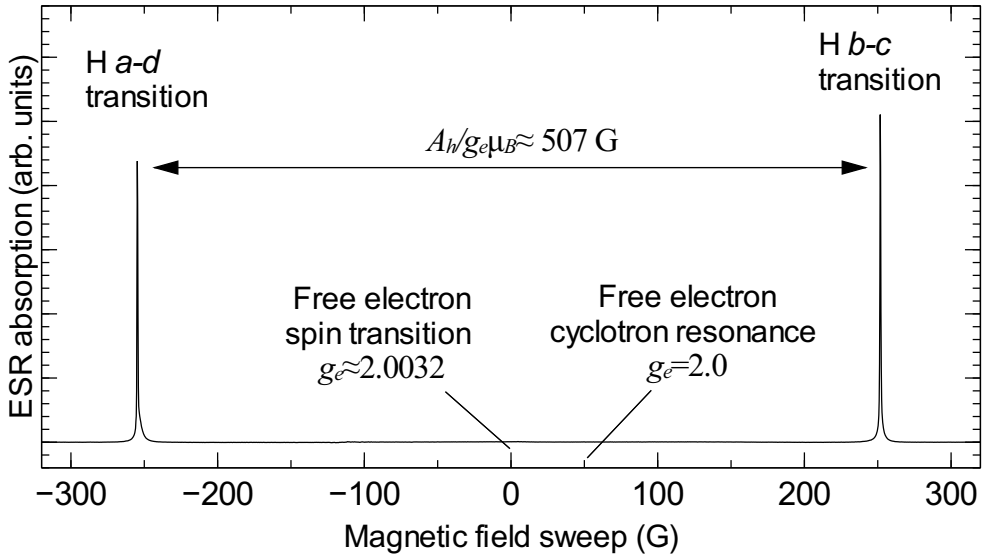

Figure 1.3: ESR spectrum of atomic H. The free electron ESR transition ($g_e \simeq 2.0023$) field is at 0 G on the field sweep axis corresponding to $\approx 46\,\mathrm{kG}$ (4.6 T) and the cyclotron resonance field is at 53 G.

$$f_{ad} = \frac{1}{2}\frac{A_h}{h} + \frac{1}{2}\frac{\mu^- B_{ad}}{h} + \frac{1}{2}\frac{\mu^+ B_{bc}}{h}\sqrt{1+\left(\frac{A_h}{\mu^+ B_{bc}}\right)^2} \tag{1.7}$$

$$\approx -\frac{1}{2}\frac{A_h}{h} + \frac{g_e\mu_B B}{h} + \left\{\frac{A_h^2}{4h\mu^+ B} - \ldots\right\}, \tag{1.8}$$

where $\mu^\pm = g_e\mu_B \pm g_n\mu_n$. The approximate expressions (1.6) and (1.8) are valid for $B > 0.051\,\mathrm{T}$. When evaluating small line shifts at high fields of several T it is adequate for our purposes to consider the two first terms in eqs. (1.6) and (1.8).

Because H atoms are electron spin-polarized in the temperature range considered in this work ($T < 2\,\mathrm{K}$), the ESR absorptions of $a-d$ and $b-c$ transitions are proportional to the populations of the a and b states. Different methods for calibration of the absolute density of H have been employed in the past [36, 37]. In this work the calibration is performed either calorimetrically by measuring the heat released in recombination of H↓ sample [12] or by monitoring the decay with a pressure gauge (sec. 4.2.2).

The resonance spectra of H↓ gas coincides with the free atom spectrum in the low density limit when the line broadening and shifts are very small (sec. 2.6). Then the ESR lines can be used to find the absolute value of magnetic field. This feature is utilized in all experiments included here.

1.6.2 Nuclear magnetic resonance

The $a-b$ NMR transition frequency (fig. 1.2) is given by

$$f_{ab} = \frac{1}{2}\frac{A_h}{h} - \frac{1}{2}\frac{\mu^- B}{h} + \frac{1}{2}\frac{A_h}{h}\sqrt{1+\left(\frac{\mu^+ B}{A_h}\right)^2} \tag{1.9}$$

$$\approx \frac{1}{2}\frac{A_h}{h} + \frac{g_n\mu_n B}{h} + \left\{\frac{A_h^2}{4h\mu^+ B} - \ldots\right\}. \tag{1.10}$$

For $B = 4.6\,\mathrm{T}$ the hyperfine term $A_h/2h \approx 710\,\mathrm{MHz}$ is much larger than the Zeeman term $g_n\mu_n B/h \approx 200\,\mathrm{MHz}$. Therefore, compared to the ESR transitions the NMR transition is more sensitive to changes in the hyperfine constant A_h. However, in practice NMR has much lower sensitivity than ESR and its direct detection is not possible for the small samples considered in this work. The $a-b$ transition can in addition be used to manipulate nuclear polarization and saturation of this transition has been used to equalize the a and b state populations for recombination studies of H↓ [25, 38]. NMR induced a-state atoms have also been used to probe the surface density of H↓↑ [10, 25]. We employed NMR to manipulate the nuclear polarization of H in H_2. In addition, we have used different approaches to enable NMR detection in our experiments, as described below.

1.6.3 Thermal detection for gas phase H

The properties of gas-phase H give alternate possibility for detection of the NMR transition. The large energy (4.5 eV/H_2) released in the formation of H_2 molecules has been previously employed for detection of ESR [39]. The ESR induced c or d atoms rapidly recombine which is detected with a fast heat sensor, a bolometer. However, in that case the sensitivity is lower than in conventional methods [39, 40].

Thermal detection of the NMR transition is more complicated because the recombination rate of a-atoms depends on the density and temperature. For a fast response the a atoms must recombine quickly. Hence the bolometric method is only useful for studies of H↓↑ gas at conditions when the lifetime of a atoms is short enough.

1.6.4 Electron-nuclear double resonance

An alternative way to overcome the sensitivity problem of NMR is to detect the NMR transition via a change in the ESR signal, by using the electron-nuclear double resonance (ENDOR) [41]. The application of NMR transition modifies the a and b populations and hence changes the ESR absorption of the $a-d$ and $b-c$ transitions. A prerequisite for such an experiment is a high degree of nuclear polarization

$$P = \frac{n_a - n_b}{n_a + n_b}. \tag{1.11}$$

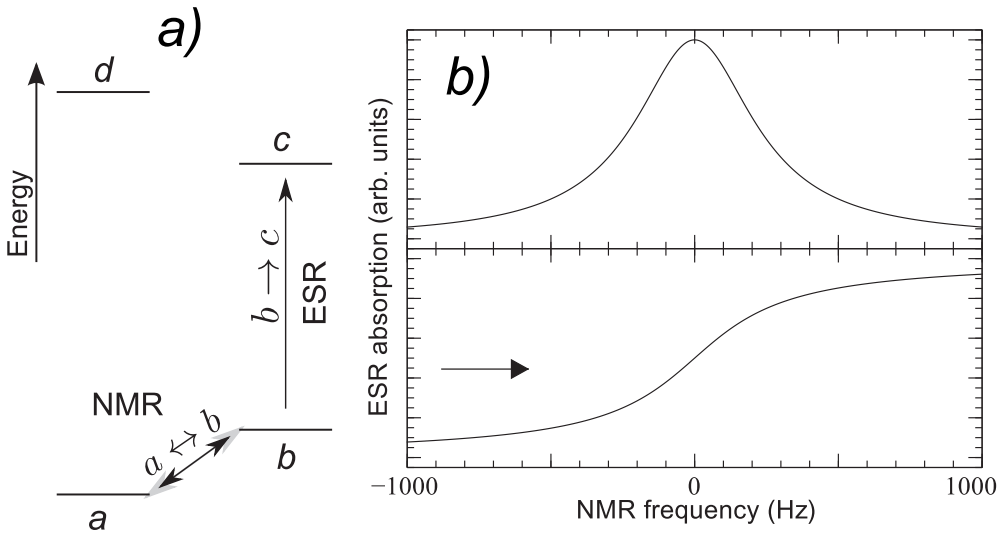

Figure 1.4: ENDOR experiment. *a*) The hyperfine states of H and the relevant transitions for ENDOR. *b*) ENDOR line shapes when initially $P \approx 1$. Upper panel: fast relaxation. Lower panel: very slow relaxation. The signal recorded as a function of the rf frequency represents the total number of atoms transferred from a to b since the beginning of the sweep. Note that the ESR dispersion remains constant in both cases.

A high value of P was obtained in all experiments here.

In an ENDOR experiment the sweep field is first stopped at an ESR transition, for example at the $b-c$ transition. Then rf power is applied to the NMR resonator and its frequency is swept across the NMR $a-b$ transition. The hyperfine levels of H and the transitions involved are shown in fig. 1.4*a*. The sign of the ENDOR responses are different for H$\downarrow$ and H in H_2 because initially for H$\downarrow$ a negative nuclear polarization $P \approx -1$ is obtained due to the preferential recombination of a-atoms. For H in H_2 $P \approx 1$ is typical because of relaxation via the $a-c$ transition (sec. 1.6.5). Thus for H$\downarrow$ the $b-c$ ESR absorption decreases from what it was before the NMR transition, while for H in H_2 the ESR absorption grows at the NMR transition from nearly zero.

Two different passage conditions of ENDOR sweeps were realized (fig. 1.4*b*):

1. Fast $a-b$ relaxation (fig. 1.4*b*, upper panel). The a and b populations relax to equilibrium nearly instantaneously after the NMR excitation. The ENDOR spectrum reflects the NMR transition rate, thus actual spectrum is recorded.

2. Slow $a-b$ relaxation (fig. 1.4*b*, lower panel). The signal recorded as a function of the rf frequency represents the total number of atoms transferred from a to b since the beginning of the sweep. The actual ENDOR spectrum, *i.e.* the transition rate as a function of frequency, is obtained by the derivative of the spectrum.

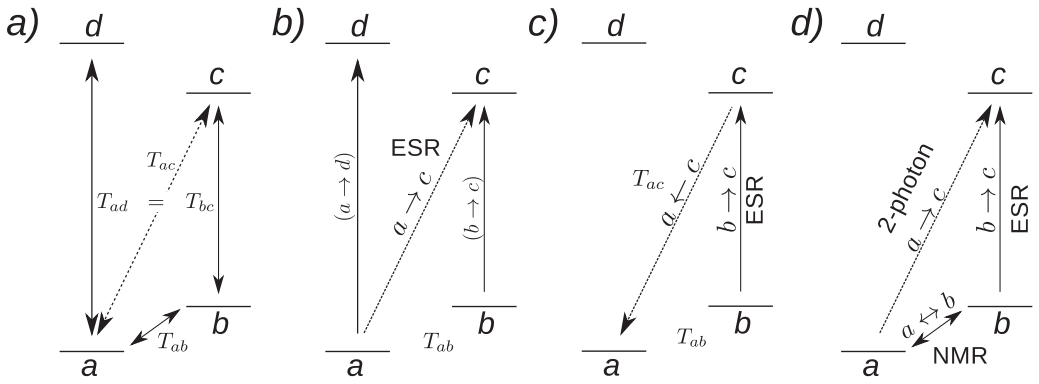

Figure 1.5: *a*) Electron and nuclear relaxation times important in our experiments. *b*) ESR pumping of $a \to c$ transition in H$\downarrow$. *c*) ESR pumping of the $b \to c$ transition following relaxation via the forbidden $c \to a$ transition. *d*) Two-photon excitation of the $a - b - c$ transition.

One should note that the term relaxation rate reflects here the recovery time needed for the a and b populations and thus the ESR absorption to recover after inducing the NMR transition. The term does not necessarily indicate that the relaxation would proceed via the nuclear and electron spin relaxation processes. In H$\downarrow\downarrow$ gas the NMR induced a atoms can be replaced from a b atom buffer (in fact nuclear relaxation in this case would produce a-atoms). As discussed in chapter 3, there is a complication in the interpretation of ENDOR in 2D H$\downarrow\downarrow$.

1.6.5 Dynamic nuclear polarization

Different types of dynamic nuclear polarization may occur in atomic hydrogen. To obtain nuclear polarization, nuclear relaxation via the $a - b$ transition (T_{ab}, fig. 1.5) must be much slower than the process creating nuclear polarization. Under condition when nuclear $b \to a$ relaxation is slower than two-body recombination, a nuclear unpolarized sample (H$\downarrow$) evolves to a doubly polarized state (H$\downarrow\downarrow$) due to the preferential recombination of a-state atoms. This can be considered as chemically induced dynamic nuclear polarization.

Magnetic resonance is a natural method for manipulating nuclear polarization. In the case of H$\downarrow$ it would seem that one can produce doubly polarized gas of b-state (a-state) by ESR excitation ("pumping") of the $a \to d$ ($b \to c$) transition with subsequent recombination of the d (c) state atoms (fig. 1.5*b*). However, because of the fast spin-exchange $d + b \leftrightarrow a + c$, the ESR pumping of $a \to d$ ($b \to c$) transition effectively equalizes the a and b populations [15, 42]. Another possibility is to pump the "forbidden" $a \to c$ transition (fig. 1.5*b*), demonstrated for H$\downarrow$ in ref. [42]. In that case spin exchange further enhances the nuclear polarization.

Relaxation via the forbidden $a - c$ transition has been employed for enhancing nuclear polarization in H in H_2. In ref. [43] it was found that $b \to c$ excited atoms

relaxed relatively fast to the a-state via the forbidden $a-c$ transition, allowing to transfer a large fraction of the b-state atoms to the a-state via pumping the $b-c$ transition (fig. 1.5c). From the relation of the $a-c$ transition probability one would expect $T_{ca}/T_{ad} \propto \kappa^2 \approx 10^{-5}$. The $c \to a$ relaxation time T_{ca}≈500 s was found to be about ten times shorter ($T_{ca}/T_{ad} \approx 10^{-4}$) [43]. In our experiments even shorter $c-a$ relaxation times have been found ($T_{ca}/T_{ad} \approx 0.1-1$) [P6, P8].

1.6.6 Coherent two-photon spectroscopy

In incoherent ENDOR there is no coherence between the NMR and ESR induced excitation, thus the excitations work independently and can be written as $a-b; b-c$. The forbidden $a \to c$ (and $b \to d$) transition becomes allowed for coherent two-photon absorption which in the previous notation can be written $a-b-c$ (fig. 1.5d). In the level scheme where $a-b$ and $b-c$ are allowed transitions coupled by rf excitations, and $a-c$ is forbidden for single photon absorption, effects related to electromagnetically induced transparency (EIT) may appear [44]. A classical example of the EIT effect is modification of absorption due to destructive/constructive interference of the $a-b$ and $b-c$ excitations.

1.7 Basic experimental setup

The main blocks of typical experimental setup used at Turku to stabilize H↓ are illustrated in fig. 1.6a. The H gas is produced in the cryogenic dissociator by rf discharge [45, 46]. Experiments with H↓ are performed in the sample cell (SC), located in the center of a superconductive solenoid in the magnetic field of $B \approx 4.6$ T. Electron spin-polarized atoms in the a and b states are pulled by the magnetic field gradient to the SC via the fill line. The SC can be cooled to 100 mK temperatures by a dilution refrigerator. The main diagnostic tool in our setup is the ESR spectrometer comprising of the ESR resonator and the mm-wave bridge.

Differences between our experimental setup and other setups are the cryogenic ESR spectrometer and the construction of the ESR resonator [36, 37, 47]. The spectrometer has the detection sensitivity of about 10^9 spins/G at low excitation power of 20 pW [40], enabling experiments with small samples while still maintaining negligible ESR power related effects. The ESR resonator is of Fabry-Perot type with half-open construction [48]. The Fabry-Perot resonator (FPR) made possible the experimental cells used in this thesis. Previously closed cylindrical cavities have been used [36, 37, 47].

A typical construction of the sample cells used in this work is shown in fig. 1.6b. Atomic hydrogen is detected in the FPR where the atoms interact with the mm-wave field. Also the profile of the mm-wave excitation field B_1^2 in the FPR is shown in fig. 1.6b. The sides of the resonator are open enabling a fast exchange of H↓ atoms between the FPR and the SC. Depending on the experiment, the FPR consists of flat and spherical mirrors or of two spherical mirrors. To perform NMR

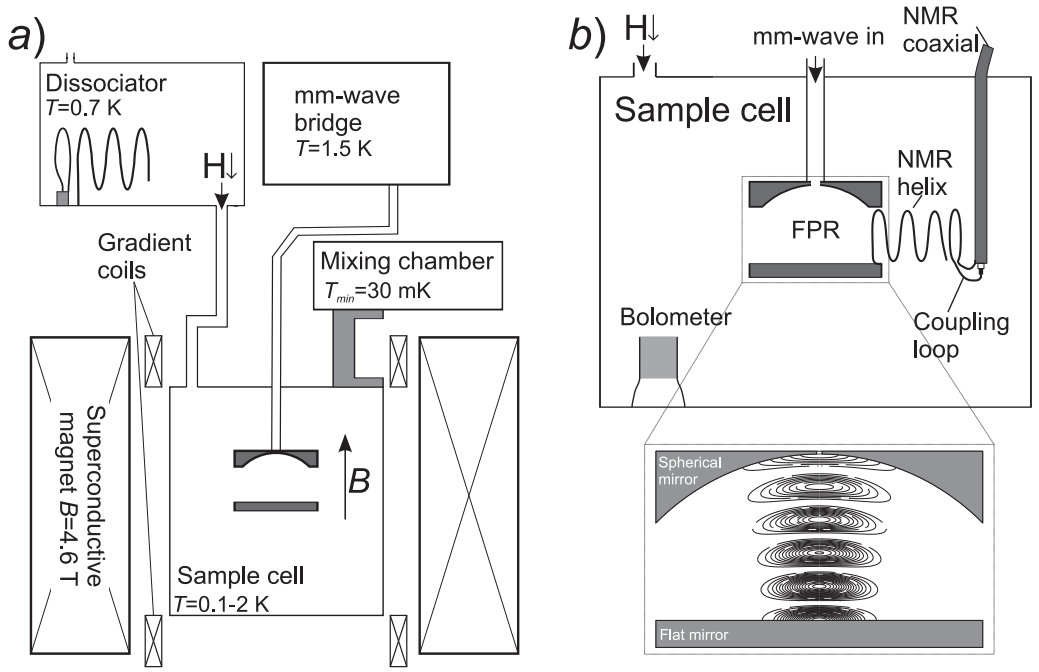

Figure 1.6: *a*) Block diagram of the experimental setup. *b*) A typical sample cell used in the experiments. Bolometer is one example of an additional device in SC [P1]. A contour plot of the mm-wave excitation field B_1^2 in the Fabry-Perot resonator (FPR) is presented in the inset.

and ENDOR experiments, we constructed helical rf resonator [49] located close to the FPR, so that part of the field from the rf resonator extends to the region of mm-wave field in FPR. Additional devices like bolometer [39] or quartz microbalance [50] could be incorporated in the SC. More details on the construction of the sample cells used for each experiment considered in this thesis will be given in the respective chapters.

The ESR spectrometer operates in the continuous-wave (CW) mode with a constant mm-wave frequency $f_{ESR} \equiv f_{bc} \equiv f_{ad}$, normally tuned to the center of the FPR resonance. The superconductive magnet includes a separate sweep coil which is used to sweep the magnetic field across the resonance values B_{bc} and B_{ad} for the ESR $b-c$ and $a-d$ transitions. Additional gradient coils were used to tune the magnetic field homogeneity. Typical performance of the magnet was following. The field inhomogeneity could be reduced to less than 2 G/cm by optimizing the gradient coil currents. The field decay rate was about 0.2 mG/s. In the last experiments [P7, P8] with a new magnet both quantities were improved at least an order of magnitude.

Chapter 2

Influence of interactions on magnetic resonance

This thesis describes experiments where magnetic resonance spectra for H atoms in different systems were studied. In this chapter we review interactions which cause shifts and broadening of the resonance lines. Special attention is paid to the systems of 2D and 3D H$\downarrow$ gas. For H in H_2 a detailed consideration of these effects is included in chapter 5.

2.1 Types of interactions

In section 1.2 we considered the interaction of a single H atom with magnetic field. Here we include interactions with other H atoms and with the environment, *e.g.* helium film on the walls of the sample cell.

Mechanisms of the interactions discussed in the following sections are different. First we consider short range interaction in atomic collisions, the contact interaction, which is effective when the interatomic distance is of the order of the atomic size r (for H $r \sim 0.53\,\text{Å}$, the Bohr radius). In the following section effects due to the dipolar interaction are discussed. It operates at longer distances and is effective also in solids. In section 2.4 different effects that can lead to changes in the hyperfine interaction of H atom are presented. Finally in section 2.5 influence of instruments and effects of atomic motion are considered.

Quantum gases which have "strong" dipolar character have been under considerable interest and were recently reviewed by Lahaye *et al.* [51]. At low temperatures collisions occur only via the lowest partial waves, in particular via the s-waves and H is in this cold collision regime at temperatures below 1 K [52]. Then the interaction potential can be approximated [51] by

$$U_{contact} = \frac{4\pi\hbar^2}{m} a \delta(\boldsymbol{r}) . \tag{2.1}$$

Here a is the s-wave scattering length. In this approach in order to interact particles must approach each other to the collision distance $r \sim a$ when their electronic wave functions start overlapping. Usually this kind of interaction is attributed to the exchange effects due to the indistinguishablity of electrons. Accounting for the total spin of the electron pair sets certain limitations to the symmetry of the wave function. This leads to an additional term in the Coulomb interaction, called the exchange integral which is either added to or subtracted from the interaction energy [53]. Therefore, the interaction appears to depend on the total spin of the electrons of the colliding atoms and on the overlap of the wave functions. This interaction is short range and effective in interatomic collisions when the atoms approach closely each other.

The magnetic dipole-dipole interaction is much weaker than the contact interaction and is typically neglected. However, some atoms or molecules possess a large magnetic dipole moment which can lead to new effects [51]. For spin-polarized atoms the dipolar interaction energy is given [51] by

$$U_{dd}(\boldsymbol{r}) = \frac{C_{dd}}{4\pi}\frac{1-3\cos^2\theta}{r^3}, \tag{2.2}$$

where $C_{dd} = \mu_0\mu^2$ is the dipolar coupling constant with μ being the magnetic moment of the particles and θ is the angle between the direction of polarization and the relative position of the particles. Compared to the isotropic contact interaction this interaction is anisotropic and operates at longer distances. In ref. [51] an effective parameter $\varepsilon_{dd} = a_{dd}/a$ is introduced to measure the relative strength of the dipolar interaction versus the contact interaction. Here $a_{dd} = C_{dd}m/12\pi\hbar^2$. For H $\varepsilon_{dd} \approx 0.008$, similar to ^{87}Rb, but for ^{52}Cr which has $\mu = 6\mu_B$, $\varepsilon_{dd} \approx 0.16$ [51]. On the grounds of this comparison H is not a special dipolar gas. Yet, at high density the long range character of the dipolar interaction leads to shift and broadening of the magnetic resonance lines in our systems. For species with electric dipole moment, ε_{dd} can be larger than 100 [51].

2.2 Effects of collisions

2.2.1 Cold collision shift in different systems

We consider shifts in magnetic resonance (and optical) spectra due to atomic collisions. These effects are closely related to atomic time and frequency standards where they put one of the main limitations to the accuracy of such devices. For a gas in the cold collision regime the shift is commonly referred to as the cold collision shift or clock shift (CS).

Collisional shifts were first discovered in atomic frequency standards operating at room temperature [54]. Since the late 1970s a possibility of a cold frequency standard based on H was studied because a H maser operating at $\sim 1\,\mathrm{K}$ was predicted to have an improved accuracy over existing standards [54]. The experiments

by Hardy and coworkers in the early 1980s with zero-field resonance of H down to 0.1 K provided important parameters for atomic hydrogen in a liquid helium coated chamber [55, 56]. Cryogenic H masers operating at 0.5 K were realized in 1986 by several groups [57, 58, 59]. However, Verhaar and coworkers found out that another kind of shift previously not considered, due to hyperfine interactions between atoms during collisions, could severely limit the accuracy of the device [60, 61]. Hayden *et al.* [62] found that the shift of H maser frequency has opposite sign compared to that predicted by the theory [63].

A rapid progress in frequency standards has taken place due to the development of laser cooling and trapping methods. A great deal of studies have been conducted since the beginning of the 1990s with ultra-cold ($\lesssim 1\,\mu$K) trapped atoms. Gibble and Chu observed the cold collision shift for ^{133}Cs atoms in 1993 [13]. In 1999 an ultra-cold cesium fountain replaced the old room temperature primary frequency standard of the National Institute of Standards and Technology (NIST) in USA [64].

Theories of the collisional line shifts at low temperatures are generally thought to be well understood and have been confirmed in many experiments [65]. There is however cases where the theory and experiment disagree even now. The theories failed to explain the shift of the cryogenic H maser frequency [63, 66]. The behavior of optical $1s-2s$ transition shift in Bose-condensed H$\uparrow$ gas disagreed with simple theory [9, 67, 68, 69]. Recently the shift of optical transition for indistinguishable fermions has generated substantial interest [70, 71]. Because of the $\sim 10^6$ times smaller wavelength of optical transitions compared to rf transitions, inhomogeneities in optical excitation field can be significant [70]. Our experiments differ from the above mentioned because we work at high magnetic field, where the Zeeman interaction is much stronger than the hyperfine interaction.

Various schemes have been proposed and developed to overcome the collisional shifts. The cold collision shift can be canceled by carefully adjusting the hyperfine populations of atoms [72]. Collisional shifts do not exist for indistinguishable fermions interacting via the s-waves [70, 73]. Collisions can be also inhibited by fixing atoms in an optical lattice [74]. Another possibility is a single ion frequency standard [75]. Operation at optical frequencies in new clocks provides additional accuracy. However, the improvements reveal new effects limiting the accuracy such as shifts due to the black-body radiation and local gravitational potential. The fractional frequency inaccuracy of the NIST Cs standard is 4×10^{-16} [64], three orders of magnitude lower than that of H masers. New optical clocks approach 10^{-18} level [75].

2.2.2 The mean-field approximation

In the cold collision regime one can apply the mean-field theory to account for the shifts of the spectral lines [69, 76, 77, 78]. The energy level shift of atoms in state

i due to atoms in state j is given by

$$\delta\mu_i = \frac{4\pi\hbar^2}{m} n_j a_{ij} g_{ij}. \tag{2.3}$$

Here n_j is the density of atoms in state j, a_{ij} is the scattering length in collisions between states i and j and g_{ij} is the two-body correlator. For indistinguishable bosons $g_{ij} = 2$, for distinguishable particles $g_{ij} = 1$ and for indistinguishable fermions $g_{ij} = 0$. If the states i and j are coupled by excitation, the atoms in these states remain indistinguishable and $g_{ij} = 2$. For bosons the shift of a single energy level i due to all atoms is given in a more general form by

$$\delta\mu_i = \frac{4\pi\hbar^2}{m} \times \sum_j n_j a_{ij} g_{ij}. \tag{2.4}$$

Here the sum $\sum_j$ is over all energy states, including the state i. In the case of a ground state H atom $j = a, \ldots d$, the scattering length for atoms having anti-parallel electron spins is a_s (singlet), and for parallel spins a_t (triplet). We obtain the cold collision shift for the transition $i - k$:

$$h\Delta f_{CS}^{ik} = \delta u_k - \delta u_i. \tag{2.5}$$

We will hereafter use the notation Δf_{CS} to account for the cold collision shift. Usually, the Δf_{CS} depends on all populations n_j, but in the case of H$\downarrow$ only n_a and n_b are significant. The shifts $\Delta f_{CS}^{ad}(n_a)$ and $\Delta f_{CS}^{bc}(n_b)$ are called intrastate shifts, *i.e.* the shifts of the $a - d$ transition frequency as a function of n_a and the $b - c$ transition frequency as a function of n_b, respectively. Similarly, the shifts $\Delta f_{CS}^{ad}(n_b)$ and $\Delta f_{CS}^{bc}(n_a)$ are called the interstate shifts. The cold collision shift for the $a - b$ transition vanishes because the electron spin is conserved.

For transitions involving a spin flip the evaluation of the shift is less straightforward and requires careful symmetrization of the wave function for the colliding atoms [P3]. Although it turns out that the above simple evaluation is not correct, it provides estimates for the magnitudes of the shifts originally expected in our experiments. Results of the more sophisticated theory of the intrastate and interstate shifts for 2D and 3D H$\downarrow$ is discussed in sec. 2.2.3 and in chapters 3 and 4.

To our knowledge, so far only Bashkin [76] has considered the collisional shifts in high field magnetic resonance. Maan *et al.* [79] presented theoretical studies of cryogenic H maser at $B \neq 0$ ($B \approx 0.05\,\mathrm{T}$, $T \approx 0.6\,\mathrm{K}$). They found a difference to the zero-field case, and the shift depended on the populations of the hyperfine states and the coherence of atoms in different states [79]. Kokkelmans *et al.* [77] applied the mean-field approximation to the theory first developed for H maser, leading to eqs. (2.4) and (2.5). Killian *et al.* [78] interpreted the shift of the optical $1s$-$2s$ transition in H by using the mean field theory. Later a similar approach has been adopted in several papers [69, 73, 71].

We do not know of any works on collisional shifts in 2D H↓ gas. Morrow and Berlinsky [80] considered the zero-field resonance line shift of adsorbed H at temperatures below 4 K but on the grounds of later developments in the theory of such frequency shifts [60, 61] the result of ref. [80] seems to be incorrect.

2.2.3 Cold collision shift in high magnetic field

Interest in the cold collision shift in high field magnetic resonance of atomic hydrogen rose after 2000 when such shifts had been observed in other systems [13, 77, 78]. It was realized [14] that the observed shift of the 2D H↓ ESR line [81] was ~ 100 times smaller than predicted by the theory available at that time (sec. 2.2.2). Earlier the collisional shifts were not taken into account either in 3D or 2D H↓ [47, 37]. The densities in ESR experiments with 3D H↓ were in addition several orders of magnitude too small to observe such shifts.

A straightforward application of the "simple" theory (sec. 2.2.2) to doubly polarized gas H↓↓ gives for the intrastate shift

$$h\Delta f_{CS}^{bc}(n_b) = \frac{h^2}{\pi m} 2n_b (a_s - a_t) . \tag{2.6}$$

This yields the shift about $-4 \times 10^{-18} \times n_b \,\mathrm{G \cdot cm^3}$ or $\Delta f_{CS}/f \approx -10^{-4} \times 10^{-18} \times n_b \,\mathrm{cm^3}$. The interstate shift

$$h\Delta f_{CS}^{ad}(n_b) = \frac{h^2}{\pi m} n_b (a_s - a_t) , \tag{2.7}$$

is a factor of two smaller than the intrastate shift because in this case we have distinguishable atoms and the two-body correlator is $g = 1$.

To estimate the shift for 2D H↓, we use a scaling approach where the effective 3D density of 2D H is obtained from the surface density σ through the relation $n = \sigma/l_d$, where $l_d \approx 0.5\,\mathrm{nm}$ (refs. [27, 28], sec. 1.4). From eq. (2.6) we get for the intrastate cold collision shift in 2D H↓↓

$$h\Delta f_{CS}^{bc}(\sigma_b) = \frac{h^2}{\pi m} 2\frac{\sigma_b}{l_d} (a_s - a_t) . \tag{2.8}$$

Eq. (2.8) yields $\sim 80 \times 10^{-12} \times \sigma_b \,\mathrm{G \cdot cm^2}$ which is two orders of magnitude larger than the observed shift.

In the first experiments with 2D H↓ in Turku [12, 81, 82] it was not possible to separate the cold collision shift from the dipolar field effects. Modifications in the experimental setup allowed to use NMR besides ESR to resolve the contributions of these effects [P1]. The experiment confirmed the very small cold collision shift in 2D H↓↓ gas. Motivated by this observation we designed for 3D H↓ an experiment [P3], which verified the small intrastate shift but the interstate shift was found to be an order of magnitude larger. These observations were the motivation to find a new theoretical interpretation which has been given in our papers P3 and P4,

and by Safonov *et al.* [83, 84] who pointed out a factor of two error in P3. In P4 we suggested that the result of P3 is correct in the hydrodynamic regime where also the experiments have been performed.

Because the hyperfine interaction mixes the spin states, the total spin $\mathbf{F} = \mathbf{I}+\mathbf{S}$ has to be used as the quantum number in zero and low field. In the high-field limit $\left(\frac{g_e \mu_B B}{A_h} \gg 1\right)$ projections of the electron and nuclear spins $m_S, m_I = \pm\frac{1}{2}$ are good quantum numbers (fig. 1.2). Since H atoms are bosons, at low temperatures ($T < 1\,\mathrm{K}$ for H) only the lowest-energy even partial wave (s-wave) contributes to the interatomic interaction. This leads to the interstate shifts [84]

$$h\Delta f_{CS}^{ad}(n_b) = \frac{1}{2}\frac{h^2}{\pi m} n_b (a_s - a_t) \tag{2.9}$$

$$h\Delta f_{CS}^{bc}(n_a) = \frac{1}{2}\frac{h^2}{\pi m} n_a (a_s - a_t), \tag{2.10}$$

which are a factor of two smaller than the result of sec. 2.2.2 and eq. (2.7). According to P4 this is valid in the collisionless regime at $\lesssim 10^{16}\,\mathrm{cm}^{-3}$ while in the hydrodynamic regime the shift should be twice smaller due to a rapid loss of coherence and recombination of spin-up atoms. The ESR intrastate frequency shift is zero because atoms are excited into a coherent superposition of spin states interacting only via the triplet potential (also ref. [85]). The ESR induced H↑ atoms recombine after the coherence of the superposition state is lost in collisions with atoms of the third state and with the walls.

2.3 Dipolar interaction

Magnetic dipole-dipole interactions may influence both line position and width. For gas phase H↓ these interactions exist only between H atoms but in solids the presence of other magnetic species may cause similar effects. When considering interatomic collisions the dipolar interaction is much weaker than the contact interaction and is typically neglected. However, the dipolar interaction is responsible for three-body recombination and two-body relaxation in H↓↓, limiting the highest densities attainable [15]. At long range the effect of dipolar interaction is equivalent to internal magnetic field. Inhomogeneities in this field lead to broadening and average field shifts the resonance lines.

2.3.1 Dipolar broadening

The dipolar broadening is caused by a spread in the local magnetic fields experienced by atoms. In general both random orientations of the spins (magnetic moments) of the atoms and random positions of the atoms lead to this effect. In our experiments atoms are electron spin polarized and the broadening is solely caused by random positions. If the atoms were fixed in space and would form

a lattice the dipolar broadening would vanish. To estimate the strength of the dipolar interaction, we use the field at $\mathbf{r}_j$ induced by a dipole located at $\mathbf{r}_i$:

$$\mathbf{B}_d(\mathbf{r}_{ij}) = \frac{\mu_0}{4\pi} \frac{3(\mathbf{m}\cdot\mathbf{r}_{ij})\,\mathbf{r}_{ij} - \mathbf{m}\,|\mathbf{r}_{ij}|^2}{|\mathbf{r}_{ij}|^5}. \tag{2.11}$$

Here $\mathbf{m} = g_e\mu_B\hat{k}/2$ ($\hat{k} \uparrow\uparrow \mathbf{B}_0$) is the magnetic moment of the H atom at $\mathbf{r}_i$ and $\mathbf{r}_{ij} = \mathbf{r}_j - \mathbf{r}_i$. At the distance of the H_2 lattice constant $r = 0.379\,\mathrm{nm}$ [23] the field is $|B_d| \approx 500\,\mathrm{G}$. In gas phase the local fields for atoms spread over several hundred G but due to motional narrowing the broadening is small [47]. In the case of H atoms in solids, the spread of the dipolar fields is smaller because the atoms are located on fixed lattice sites and cannot approach each other closer than a few lattice constants [P8].

2.3.2 Dipolar shift

If the degree of spin-polarization and the density of the atoms is sufficient, the average dipolar field ΔB_{dip} (magnetization) in the sample results in a shift of magnetic resonance lines. This effect has been observed previously in paramagnetic substances [86] and in experiments with 2D H$\downarrow$ adsorbed on helium surfaces [47, 12].

2D H The dipolar field was qualitatively calculated for 2D H by Shinkoda and Hardy [47], who integrated the field over a plane having a homogeneous distribution of dipoles. Because of the divergence of eq. (2.11) at $r = 0$, one must assume a closest approach r_c to the point where the field is calculated. The result depends on r_c and the orientation of the external magnetic field with respect to the plane and may be given as

$$\Delta B_{dip} = -\alpha_d P_2(\cos\theta)\sigma. \tag{2.12}$$

Here α_d is a proportionality constant and θ is the angle between $\mathbf{B}_0$ and the surface normal. The Legendre polynomial is for a plane perpendicular and parallel to polarizing magnetic field respectively $P_2(1) = 1$ and $P_2(0) = -1/2$. The parameter α_d is inversely proportional to r_c. More sophisticated calculations have been performed (see ref. [47] and references therein), but their result $\alpha_d = 1.2\times10^{-12}\,\mathrm{G\cdot cm^2}$ do not match very well the experimental value $\alpha_d = 7.4(7)\times10^{-13}\,\mathrm{G\cdot cm^2}$ [P1].

3D H The internal field for bulk H$\downarrow$ gas was estimated considering the magnetization, given by $|\mathbf{M}| = n\cdot g_e\mu_B/2$ [15]. For a long cylindrical sample polarized in the direction of the cylinder axis as in [P3], the internal field at the end of the cylinder is

$$\Delta B_{dip} = \mu_0\mu_B n/2. \tag{2.13}$$

For the density $n = 10^{18}\,\mathrm{cm}^{-3}$ one obtains the field $\Delta B_{dip} \approx 58\,\mathrm{mG}$ which may be observable.

2.3.3 Resonant interaction between spins

Eq. 2.11 is valid in the local field approximation [87, 88], in which the so-called resonant interaction between like spins is neglected. Under an rf excitation the like spins (of identical atoms) experience an additional resonance in the dipolar interaction leading to a factor 3/2 enhancement in the broadening and shift [88, 89]. For a precise calculation one has to use the method of moments developed by Van Vleck [90] (see also refs. [34, 91, 92]). However, it appears to be less straightforward to distinguish between like and unlike spins contributing to a resonance line. In general, spins contributing to a homogeneously broadened line are like. The subject has been shortly discussed by Svare and Seidel [86]. Drabold and Fedders [93] considered a diluted and unpolarized system. They identified unlike spins by the large shift of their local fields from the resonance center and separated the contributions of like and unlike spins to different line shapes. In paper P8 (sec. 5.5.3) we did not use such method and simply atoms in the same hyperfine state were considered like.

The question is more complicated in the case of H↓. For example the dipolar field may have a contribution from atoms residing outside the rf field region of the sample. In these experiments the ESR lines of H↓ were thought to be inhomogeneously broadened, and the effects of like spins may be omitted.

2.4 Hyperfine interaction

The hyperfine interaction of H can be thought as a magnetic contact interaction of the electron and nucleus [91]. For an isolated H atom it is responsible for the hyperfine structure (sec. 1.2). The interaction with the environment, other atoms and molecules in the system, can modify the hyperfine interaction giving rise to a shift of magnetic resonance lines [54]. A spread in the change of the hyperfine interaction can also broaden the lines. Due to the relative strengths of the nuclear and electron Zeeman interactions, the changes in the hyperfine interaction are more pronounced for NMR and zero-field resonance than for ESR. An approximate value for the hyperfine interaction constant is given by [91]

$$A_h = -\frac{8\pi}{3}\mu_e\mu_n\,|\psi(0)|^2\,, \tag{2.14}$$

where $|\psi(0)|^2$ is the probability density of the electron centered on the nucleus.

Interactions with the environment can modify the electron wave function of H atom leading to a change in $|\psi(0)|^2$. The wave function is distorted by van der Waals attraction and Pauli repulsion which have opposite influence on A_h. The relative strengths of the two interactions depend on the environment and the

distances between the interacting species. Consequently the magnitude and the sign of ΔA_h depend on the environment [94].

2.4.1 Pressure shift

If a H atom undergoes collisions at a high enough rate, the electronic wave function can experience a small average change leading to a change in the hyperfine interaction. In addition to the interaction potential between the colliding species, this shift, called the pressure or buffer gas shift, depends also on the collision energy and rate. The sign of the shift depends on whether the colliding atoms sample mainly the attractive or repulsive part of the interatomic interaction potential [54].

Pressure shifts have been extensively studied for room temperature frequency standards but their theoretical calculation is difficult [54]. The pressure shift has been measured in zero-field resonance for H atoms due to H-He collisions at temperatures $\lesssim 1.3\,\mathrm{K}$ [55, 95]. It was found to vary as $-11.83 \times 10^{-18} \times n_{He}\,\mathrm{Hz} \cdot \mathrm{cm}^{-3}$ with the helium vapor density, being $-20\,\mathrm{Hz}$ at 1 K. Our experiments are performed in the temperature range where n_{He} is negligible and collisions only occur between H atoms. A pressure shift for H-H collisions also exists but to our knowledge it has not been calculated and it is expected to be much smaller than the H-He shift. If the H-H pressure shift was of the same order as the H-He shift, it would in 2D H$\downarrow$ change the hyperfine constant by about $200 \times 10^{-12} \times \sigma\,\mathrm{Hz} \cdot \mathrm{cm}^{-2}$ which would be resolvable by NMR techniques.

2.4.2 Wall shift

Adsorption of an atom on a surface is another mechanism, called the wall shift, to change the hyperfine constant. Van der Waals interaction between the adsorbed atom and the surface can distort the wave function of the adatom and lead to a change ΔA_{wall} in the hyperfine constant. The wall shift for H adsorbed on helium has been found to be $\Delta A_{wall} \sim -50\,\mathrm{kHz}$ (cp. table 2.2). In non-zero magnetic field the orientation dependence of ΔA_{wall} is expected to reflect the anisotropy in the hyperfine interaction [96].

The conditions where we have studied the wall shift differ from many earlier experiments which were typically performed in zero field and at higher temperatures. In those experiments the hyperfine transition $a - c$ experiences a fractional shift due to wall collisions [97, 54]. In our case the surface residency time at $T \lesssim 100\,\mathrm{mK}$ is about 1 s and we observe a separate resonance for 2D atoms shifted from the 3D resonance. One can easily detect ΔA_{wall} by NMR but it is hard to resolve it by ESR. A summary of different wall shift measurements is presented in table 2.2.

Method		Substrate	ΔA_{wall} (kHz)	Ref.
Zero-field resonance	-	^{4}He	-49(2)	[55]
Zero-field resonance	-	^{3}He	-23(2)	[56]
H maser	-	^{4}He	-71.5(3)	[98]
NMR, $B = 7\,\mathrm{T}$	-	^{4}He	-44.8(10)	[99]
NMR, $B = 7.6\,\mathrm{T}$	$\parallel$	^{4}He	-43.2(10)	[96]
ENDOR, $B = 4.6\,\mathrm{T}$	$\perp$	^{4}He	-45.58(4)	[P1]
ENDOR, $B = 4.6\,\mathrm{T}$	$\perp$	^{4}He+^{3}He	-43.16(10)	[P1]

Table 2.2: Wall shift ΔA_{wall} obtained for H in different experiments. Orientation of the surface with respect to the magnetic field is indicated in the second column: $\parallel$ surface parallel and $\perp$ surface perpendicular to the magnetic field. In ref. [99] there was no preferential orientation of the surface.

2.5 Other sources of line shift and broadening

2.5.1 Instrumental sources

Characteristics of the ESR spectra for 3D H$\downarrow$ are often governed by instrumental effects, of which important in our experiments are spectral line width of the mm-wave source, homogeneity of the magnetic field and non-linear response of the ESR cavity.

Frequency stability The mm-wave source starts to limit spectral resolution when its line width approaches the intrinsic line width of H. The spectral line width of our mm-wave source is 10^{-9} [40], at least two orders of magnitude smaller than the broadening of other sources in experiments.

Homogeneity of magnetic field A common cause of broadening in high-field ESR and NMR experiments is the inhomogeneity of the magnetic field. The minimum width of the 3D H$\downarrow$ ESR line we achieved by optimizing the field homogeneity differed between experiments because of different constructions of the experimental cells. In the most recent experiments [P7, P8] a new magnet with improved properties was used. The minimum line widths were limited to 50 mG [P3] (ch. 4), [P7, P8] (ch. 5); and to 100 mG [P1] (ch. 3), [P6] (ch. 5).

Effects related to ESR resonator and H density A strong absorption of mm-wave power in dense H$\downarrow$ changes the response of ESR resonator [36, 37, 85] leading to the effect called radiation damping. More strictly speaking this takes place when the number of H atoms in the ESR resonator is large enough. When increasing the density of H, one finally enters a region where the mm-wave absorption starts to saturate. The H sample absorbs all power fed to the resonator and

the cavity response becomes non-linear. In a typical ESR resonator employed in experiments here the non-linear regime is reached at $n \sim 10^{15}\,\mathrm{cm}^{-3}$. Aiming at accurate spectroscopical studies we want to minimize these effects. In P3 the cavity filling factor η was reduced by 10^3 to enable experiments in the linear regime at densities up to $10^{18}\,\mathrm{cm}^{-3}$. The ESR lines can be also shifted by the cavity pulling effect [54]. However, this effect is negligible in our experiments and it is minimized by zero detuning of the ESR frequency. The effects related to radiation damping are important for 3D H↓ only because the product ηn is much smaller for 2D H↓ and H in H_2.

2.5.2 Effects of atomic motion

Time-of-flight broadening The "time-of-flight" (TOF) broadening is caused by the finite time during which the gas atoms interact with the rf field. This effect is important in 3D at sufficiently low densities $\lesssim 10^{16}\,\mathrm{cm}^{-3}$ when the atomic motion is ballistic. At higher H↓ densities the atomic motion is diffusive due to the higher collision rate and atoms interact longer with the rf field. The TOF broadening can be also suppressed by confining the atoms in a small space where the excitation field is homogeneous. The line shape due to the TOF broadening is obtained as a Fourier transform of the excitation field the atom experiences flying through the rf field region.

The TOF broadening can be estimated from the time it takes for an atom to fly through the region of the mm-wave excitation field. The width of the excitation field maximum is about 1 mm. For the average thermal velocity $v_{th} \approx 5\times10^3\,\mathrm{cm/s}$ atoms interact with the rf field on the average about $5\times10^{-5}\,\mathrm{s}$ causing a broadening of the order 10 mG.

Doppler broadening Because of the thermal motion, the Doppler effect shifts the frequency of the mm-wave excitation the atoms feel. The Doppler broadening is given [54] by

$$\Delta f_D \approx f_0 \frac{v_{th}}{c}, \tag{2.15}$$

and it leads to a Gaussian line shape. In magnetic field units the Doppler broadening for H is given by $\Delta f_D \approx 10T^{1/2}\,\mathrm{mG{\cdot}K^{-1/2}}$, which yields $\Delta f_D \approx 6\,\mathrm{mG}$ at 0.3 K. This effect is comparable to the TOF broadening. Like the TOF broadening, Doppler broadening is suppressed at high densities when the atomic motion is diffusive. Then collisions cause rapid changes and averaging of the velocities of the atoms and hence line narrowing.

Motional narrowing In liquids and gases the thermal motion can lead to averaging of the local field experienced by the atoms and to narrowing of the resonance lines. This is very effective in free and 2D H but is absent for H in H_2.

2.6 Modifications of the ESR and NMR transitions due to interactions

We were always able to measure the ESR line position for low density H↓ gas where the effects of interactions are negligible and the H↓ line serves as a magnetic field marker enabling measurements of line shifts relative to this zero density value. It is convenient to analyze the shifts by comparing the approximated resonance equations for free and interacting atoms.

Interaction effects can be taken into account by the substitutions:
$f \to f + \Delta f_{CS}$ for the cold collision shift,
$B \to B + \Delta B_{dip}$ for the dipolar shift and
$A_h \to A_h + \Delta A$ for the change in the hyperfine interaction. Then the $a-d$ ESR transition resonance equations from eq. (1.8) for free (non-interacting) and interacting atoms get, respectively, the forms

$$hf^0_{ad} = \frac{1}{2}A_h + g_e\mu_B B^0_{ad} \tag{2.16}$$

$$hf^0_{ad} = \frac{1}{2}(A_h + \Delta A) + g_e\mu_B\left(B^0_{ad} + \Delta B_{dip} + \Delta b_{ad}\right) + h\Delta f^{ad}_{CS}. \tag{2.17}$$

Similarly we obtain for the $b-c$ transition from eq. (1.6)

$$hf^0_{bc} = -\frac{1}{2}A_h + g_e\mu_B B^0_{bc} \tag{2.18}$$

$$hf^0_{bc} = -\frac{1}{2}(A_h + \Delta A) + g_e\mu_B\left(B^0_{bc} + \Delta B_{dip} + \Delta b_{bc}\right) + h\Delta f^{bc}_{CS}. \tag{2.19}$$

We recall that the ESR spectrometer operates in the continuous wave mode at the fixed frequency $f_{ESR} \equiv f^0_{ad} \equiv f^0_{bc}$ and that the magnetic field is swept through the resonance. For free atoms the resonance fields are B^0_{ad} and B^0_{bc}. The quantities Δb_{ad} and Δb_{bc} are the observed shifts of the ESR line from the free atom line due to cumulative effects of Δf_{CS}, ΔB_{dip} and ΔA. Subtracting the free atom equation from the interacting atom equation we obtain

$$\Delta b_{ad} = -\frac{1}{2}\frac{\Delta A}{g_e\mu_B} - \Delta B_{dip} - \frac{h}{g_e\mu_B}\Delta f^{ad}_{CS} \tag{2.20}$$

$$\Delta b_{bc} = \frac{1}{2}\frac{\Delta A}{g_e\mu_B} - \Delta B_{dip} - \frac{h}{g_e\mu_B}\Delta f^{bc}_{CS}. \tag{2.21}$$

We see that one obtains the change in the hyperfine interaction constant ΔA by measuring Δb_{ij} for both $a-d$ and $b-c$ transitions. Because the cold collision shift Δf_{CS} and dipolar shift ΔB_{dip} are both proportional to the density, the measurement of the ESR line shifts as such does not, however, provide enough information to distinguish between these effects.

In NMR either the magnetic field or the frequency f_{NMR} can be swept. The $a-b$ NMR transition equations for free and interacting atom are (cp. eq. 1.10)

$$hf^0_{ab} = \frac{1}{2}A_h + g_n\mu_n B^0_{NMR} \tag{2.22}$$

$$hf_{ab} = \frac{1}{2}\left(A_h + \Delta A\right) + g_n\mu_n\left(B_{NMR} + \Delta B_{dip}\right). \tag{2.23}$$

The main difference from the ESR is that the cold collision shift is zero, since a and b atoms interact via the same potentials.

In an ENDOR measurement magnetic field is fixed at the maximum of ESR line and the frequency is swept. Denoting $B^0_{NMR} = B^0_{bc}$ and $B_{NMR} = B^0_{bc} + \Delta b_{bc}$ we find from eqs. (2.22) and (2.23)

$$hf_{ab} - hf^0_{ab} = \frac{1}{2}\Delta A + g_n\mu_n\left(\Delta B_d + \Delta b_{bc}\right). \tag{2.24}$$

Combining eqs. (2.18)-(2.19) and (2.24) we finally obtain [P1]

$$f_{ab} - f^0_{ab} = \frac{\Delta A}{2h}\left(1 + \frac{g_n\mu_n}{g_e\mu_B}\right) - \frac{g_n\mu_n}{g_e\mu_B}\Delta f^{bc}_{CS}. \tag{2.25}$$

The term $g_n\mu_n/g_e\mu_B \approx 0.002$ can be neglected with respect to unity. Eq. 2.25 provides a possibility to measure the cold collision shift of the ESR transition under the assumption that $\Delta f^{ab}_{CS} = 0$. Measuring the density dependence of the f_{ab} gives then the cold collision shift as the slope and ΔA as the intercept.

2.6.1 2D H

A specific feature of two-dimensional H is that it is doubly polarized (H$\downarrow\downarrow$). Therefore, only the intrastate shift must be considered. The shift of the 2D ESR line from the 3D line has been measured to be $\Delta b^{2D}_{bc} = 1.1(1) \times 10^{-12} \times \sigma\,\mathrm{G{\cdot}cm^2}$ [82, 12]. This is close to two orders of magnitude smaller than the cold collision shift predicted by eq. (2.8) and includes the effects of both dipolar and exchange interactions. Because there is no precise calculation of the dipolar shift available, it is not possible to figure out by ESR measurement the contribution of the cold collision shift to the 2D ESR line shift. However, according our to present knowledge the $a-b$ transition is free of the cold collision shift. Therefore, NMR on 2D H provides independent measurement of the dipolar shift allowing to separate the contributions of the cold collision and dipolar shifts in the 2D ESR line shift.

Another possibility to find out the cold collision shift is the measurement of the ESR line shift for different surface orientations with respect to the polarizing magnetic field. Then the sign and magnitude of the dipolar shift change [47] (sec. 2.3.2) while the cold collision shift is expected to remain constant.

2.6.2 3D H

Similarly to 2D H↓, the cold collision shift for three-dimensional H↓ predicted by eqs. (2.6) and (2.7) is two orders of magnitude larger than the dipolar shift. The main difference to 2D H is that with 3D H experiments can be made for a mixture of hyperfine states a and b. Therefore, measurements are possible on both $a-d$ and $b-c$ transitions and both intra- and interstate shifts can be determined. In principle, also ENDOR measurement could be made for 3D H. However, the longer lifetime of the NMR induced a-atoms leads to an uncertainty in the a-state density.

Chapter 3

Cold collision shift in 2D H

A short report on the experimental results for the cold collision shift in 2D H is published in paper P1. Paper P2 contains also a more detailed description of the double resonance method. The development of the NMR and ENDOR methods allowed us to resolve the effects of the dipolar field and cold collision shift. Here we present the experiment and observations of the incoherent and coherent ENDOR with 2D H↓. Motivation and introduction for the cold collision shift experiments is presented in sec. 2.2.3.

The experiments utilized the thermal compression method of 2D H in homogeneous magnetic field developed at the University of Turku. The experimental setup and the thermal compression method have been described in ref. [12] and in the PhD thesis of Järvinen [100]. Therefore only a brief account of these aspects is given here.

3.1 Experimental cell

In the thermal compression method a small area on the sample cell wall is cooled below the temperature of the surroundings. Due to the exponential temperature dependence of the surface density $\sigma \propto \exp(1.14\,\mathrm{K}/T)$ (eq. (1.2)), a decrease of T easily leads to a large increase in the density. This results in fast recombination in the compressed 2D H [12, 26] but the small size of the colder region enables a relatively long duration for a single experiment and decreases overheating of the 2D gas due to the even distribution of the recombination heat all over the SC [101].

The sample cell is shown in fig. 3.1. The high density 2D H is obtained in the Fabry-Perot resonator (FPR) which consists of two spherical mirrors. Its volume is divided into two parts by a Mylar foil, the lower part is filled with H↓ and the upper part with dilute ^{3}He-^{4}He mixture from the dilution refrigerator. The part of the Mylar surface refrigerated by the liquid is called the cold spot. The upper part of the FPR is well thermally insulated from the rest of the cell body

making it possible to cool it down to temperatures close to the mixing chamber temperature while the rest of the SC can stay above 100 mK. Rapid temperature adjustments of the cold spot are possible because only part of the dilute stream of the dilution refrigerator is directed to the cold spot maintaining a stable operation of the refrigerator.

For the double resonance experiments we placed a helical NMR resonator close to the FPR (fig. 3.1). A disadvantage of the helix is the strongly inhomogeneous excitation field, centered 1 cm from the cold spot. An aquadaq-film resistor was also mounted in the SC as a bolometer for thermal detection of the NMR transition. Because of the weak thermal coupling to the SC through its leads, the bolometer is a sensitive sensor of recombination heat appearing in the SC [39].

Typically H↓ experiments have been performed by monitoring the evolution of H↓ samples in the SC [12, 15, 26], *i.e.* measuring the density decay of H↓. The surface and bulk densities are not stable during such experiment. Aiming at accurate spectroscopical studies in this work, we utilized a method where recombination of atoms is balanced by a small steady atom flux from the dissociator keeping the density constant. In previous experiments H↓ was first accumulated in the SC by running the dissociator at maximum efficiency [26, 12]. During accumulation the cold spot was heated to prevent recombination on it, enabling highest possible 3D densities. After accumulation the SC is cooled to < 200 mK. Then the H↓ gas is let to evolve into the doubly polarized state (H↓↓). Finally the cold spot could be cooled to below 100 mK for thermal compression and the decay of H↓↓ in the SC was monitored.

To increase the nuclear polarization of H↓ entering the SC we constructed a device called the polarizer. It is a part of the H↓ filling line, cooled to $100-200$ mK by the lowest step heat exchanger of the dilution refrigerator and located at $B \approx 3.5$ T. Because of the low temperature, ratio of the $a-a$ and $a-b$ recombination rate constants can be up to $K_{aa}/K_{ab} \approx 10$ [25]. The polarizer has a large surface area and high A/V ratio to enable effective two-body recombination.

3.2 Experimental procedure

In order to realize constant density and steady conditions, temperatures of the SC and cold spot were stabilized and the dissociator was run at a reduced power. The H↓ flux from the dissociator had to be significantly decreased from the maximum that is used to accumulate a H↓ sample in the SC. The cold spot temperature was regulated by stabilizing the mixing chamber temperature and heating the coolant. The density of 2D H was adjusted mainly by the H↓ flux controlled by the power fed to the dissociator. The SC and cold spot temperatures had to be regulated in order to get a wider density range.

In the constant-density method the highest densities were $\sigma \approx 2 \times 10^{12}\,\mathrm{cm}^{-2}$ without the polarizer and $\sigma \approx 3.0 \times 10^{12}\,\mathrm{cm}^{-2}$ with the polarizer. To extend the measurements to higher surface densities we tried the decay method mentioned

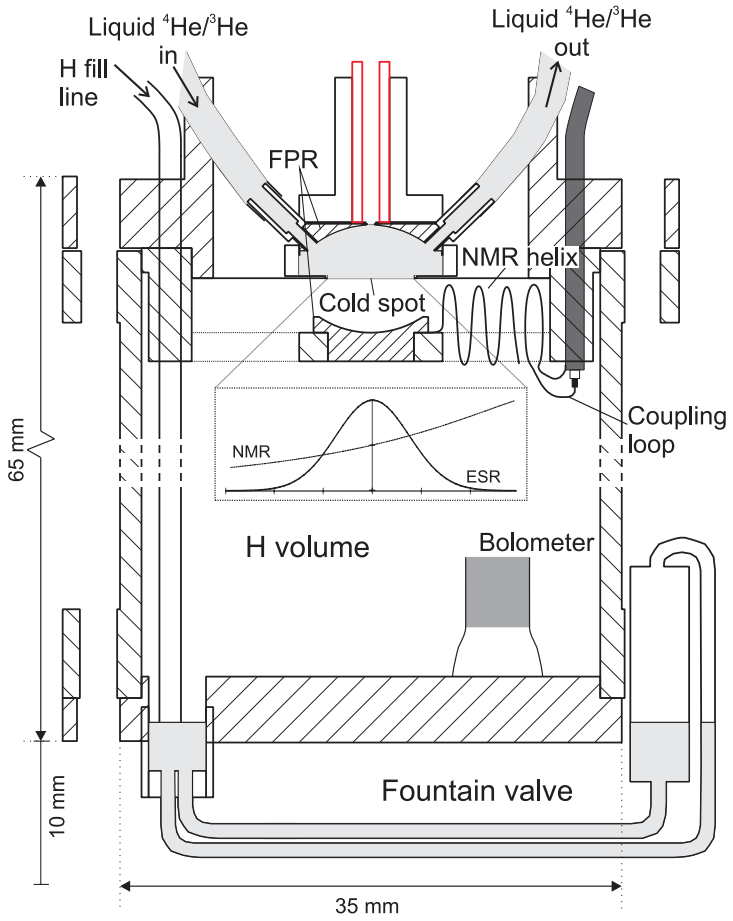

Figure 3.1: Sample cell for thermal compression of 2D H. The fountain valve is not used in these experiments. The ESR and NMR excitation field profiles on the cold spot are shown in the inset.

in the previous section. In this case the surface density was relatively stable for $\lesssim$50 s only. The decay method yielded surface densities up to about $\approx 3.5 \times 10^{12}\,\mathrm{cm}^{-2}$ for the ENDOR measurements. However, the decay method suffered from a density uncertainty and poor spectrum quality due to ESR signal drifts and short measurement time. Neither ENDOR nor thermal detection at higher surface densities was successful because of too fast recombination and strong overheating of the 2D gas.

The ESR calibration of the 3D H density was made by the calorimetric method where the recombination heat is measured and integrated [12]. The surface density was inferred from the shift Δb_{bc}^{2D} of the 2D line from the 3D line [12]. The latter dependence was carefully studied earlier in our laboratory [12, 100].

3.3 Observed spectra

3.3.1 ESR spectra

Typical CW ESR spectrum of 2D and 3D H is shown in fig. 3.2a. The effects that contribute to the 2D H line shape have been discussed by Järvinen *et al.* [12, 100] and by Shinkoda and Hardy [47]. The surface line is shifted from the bulk one towards a higher field due to the dipolar field and presumably due to the cold collision shift [P1]. In fig. 3.2*b* the ESR spectrum is shown together with a bolometer trace when the 3D density is below detection limit, representing conditions of NMR and ENDOR experiments. The NMR excitation frequency was set to such that both ESR and NMR transitions are resonant nearly in the same magnetic field. A bolometer response is observed at the ESR 2D line and there is another peak due to the NMR $a-b$ transition of surface atoms. The sensitivity of the bolometer depends on several factors. Magnitude of the bolometer signal obviously depends on the heat produced by the ESR or NMR induced recombination, balanced by cooling by H$\downarrow$ gas. The sensitivity was highest at lowest temperatures and lowest 3D H densities and it was rather good in conditions where the ENDOR experiments were carried out.

3.3.2 ENDOR spectra

The ENDOR experiment was planned for classical incoherent method $(a-b; b-c)$, but unexpectedly it turned out to be possible to carry out also coherent ENDOR, *i.e.* two-photon excitation of the NMR and ESR transitions $a-b-c$. In the experiment magnetic field is stopped at the maximum of the ESR 2D line. Then NMR frequency is swept while recording the ESR signal. The ENDOR spectrum where both effects are demonstrated is presented in fig. 3.2*c*, together with a simultaneously recorded bolometer trace. The feature *i*) in fig. 3.2*c* was attributed to incoherent ENDOR and feature *ii*) to coherent ENDOR. The bolometer response indicates NMR induced recombination for the incoherent line *i*).

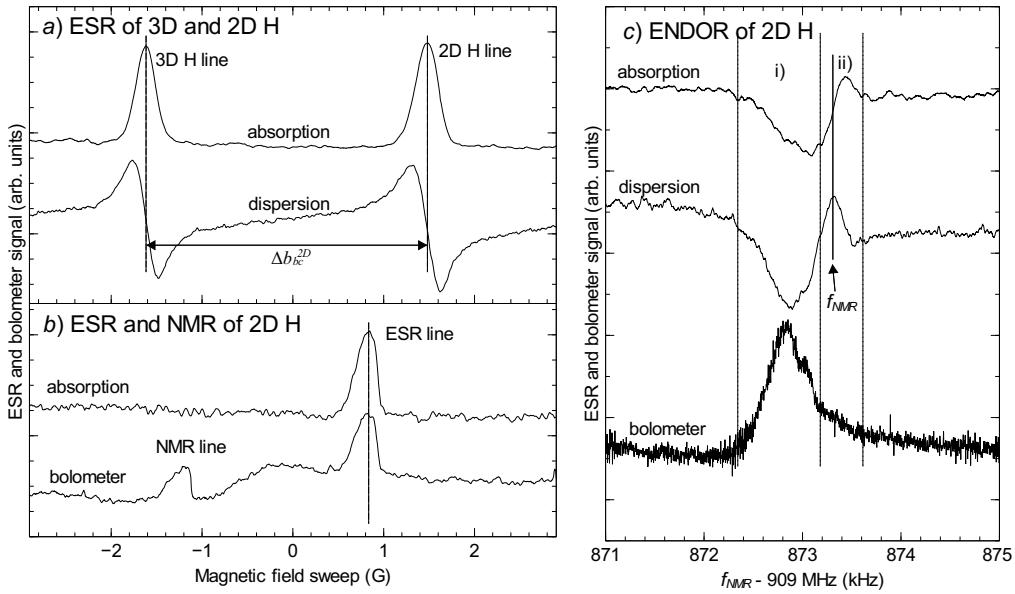

Figure 3.2: *a*) ESR spectrum of 3D and 2D H. *b*) ESR spectrum and accompanying bolometer response at conditions where only 2D resonance is observed. The NMR frequency f_{NMR} was set so that the NMR line in the bolometer trace is located in the sweep window. *c*) ENDOR spectrum of 2D H demonstrating the incoherent and coherent features. *i*) Incoherent $a-b$ excitation, *ii*) coherent $a-b-c$ excitation.

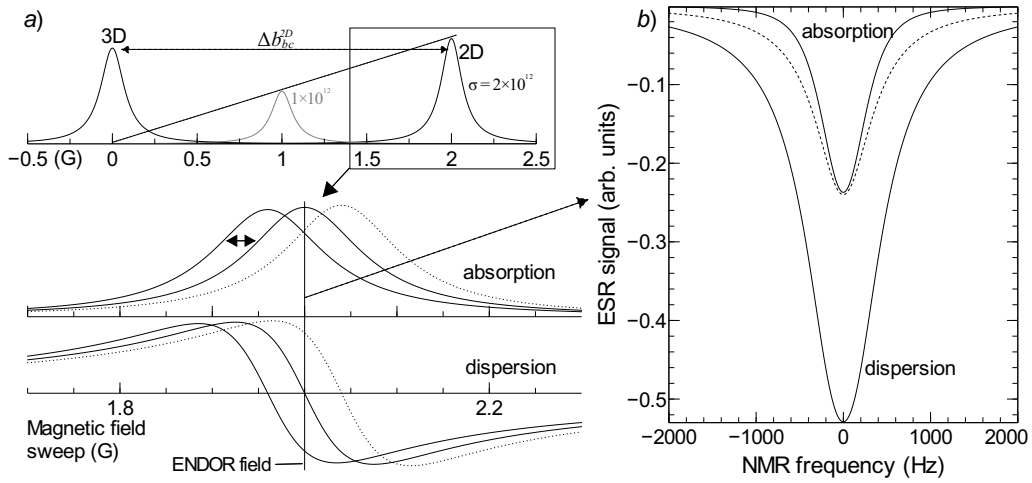

Figure 3.3: *a*) Illustrating the behavior of 2D ESR line. Upper plot: Simulated line position and amplitudes at densities $1 \times 10^{12}\,\mathrm{cm}^{-2}$ (1 G) and $2 \times 10^{12}\,\mathrm{cm}^{-2}$ (2 G). Lower plot: Shifts of the 2D line position due to $\mp 2\%$ density changes. Vertical axis marks the field where the ENDOR spectrum is recorded. *b*) Simulated incoherent ENDOR line shape. At the NMR transition the 2D line is shifted to a lower field, thus both absorption and dispersion decrease at the position where ENDOR spectrum is recorded. The ESR line amplitude is scaled to 1. The dashed line represents the line shape of the NMR transition, which is 800 Hz wide and causes a maximum -2% change in the 2D H density at 0 Hz. Lorentzian line shape is used for approximating the NMR and ESR line shapes.

As illustrated in fig. 3.3, the incoherent ENDOR line *i*) shows a nonlinear response of the 2D ESR line to a density change. The line amplitude is proportional to the density, as is the shift $\Delta b_{bc}^{2D} = 1.1 \times 10^{-12} \times \sigma\,\mathrm{G} \cdot \mathrm{cm}^2$ of the 2D line from the 3D line [12]. NMR excitation leads to a decrease in the density of 2D H, hence both the amplitude and the shift decrease and for a small ($\lesssim 5\%$) density change one observes a decrease in both ESR absorption and dispersion (fig. 3.3*b*). The ESR line shift has the largest effect on ENDOR spectrum because the line width is an order of magnitude smaller than the shift. The simulated ENDOR spectrum in fig. 3.3*b* agrees qualitatively with the observed spectra.

The feature *i*) disappeared when the cold spot temperature was lowered, leaving only the feature *ii*) in the ENDOR spectrum (fig. 3.4*a*) [P2]. The dispersive line shape of the ESR absorption in the latter feature cannot be explained by changes in the surface density. A density increase would shift the 2D line off resonance leading to a decrease in the absorption (fig. 3.3*a*). Also the narrow width of the *ii*) line is intriguing. On the basis of preceding arguments, and because of the absence of the bolometer response, we conclude that the line *ii*) is not related to a surface

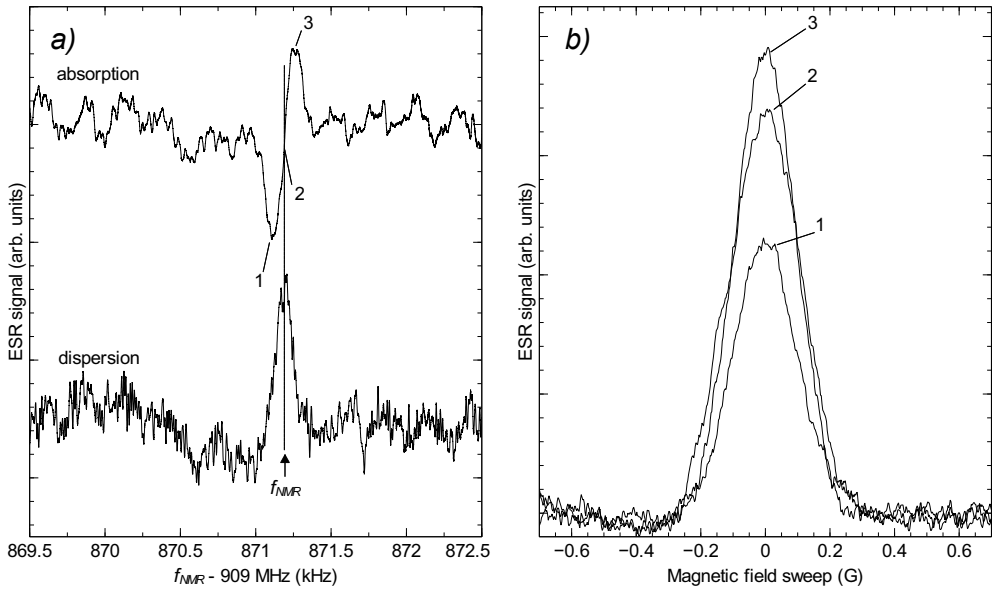

Figure 3.4: *a*) ENDOR spectrum showing the coherent two-photon line only [P2]. *b*) ESR spectra of the 2D line at fixed NMR frequencies 1, 2 and 3 indicated in *a*) [P2]. It should be noted that the ESR dispersion amplitude remained constant in *b*). f_{NMR} indicates the position chosen for the NMR transition.

density change. Since the ESR absorption is modified while the surface density is constant, this may point to the phenomenon of electromagnetically induced transparency and absorption (EIT) [44]. The absence of recombination in *ii*) implies that no atoms are transferred into states a and c, which agrees qualitatively with the effect of coherent population trapping (CPT) [44].

An additional proof of EIT and CPT is obtained in the following experiment: We recorded ESR spectra at a constant NMR frequency corresponding to either minimum, center or maximum denoted respectively by numbers 1, 2, 3 in fig. 3.4*a* [P2]. The ESR spectra for each NMR excitation frequency are presented in fig. 3.4*b*. The ESR absorption is observed to be modified by $\approx \mp 30\%$ for the detunings 1 and 3, while the line position remains constant. This observation implies that the surface density does not change while absorption is increased (decreased) for blue (red) detuning. From these observations we conclude that the ENDOR line *ii*) is due to coherent two-photon absorption and that the observed effect resembles the EIT and CPT phenomena [P2].

Line width The coherent ENDOR line width is much narrower than the incoherent one. We suggest the following explanation: The excitation field profiles for ESR and NMR are different on the cold spot. The ESR has axially symmetric

field centered at the cold spot while the NMR field is smoothly changing over the cold spot area as illustrated in fig. 3.1. Therefore NMR excites atoms more or less homogeneously over the whole area of the cold spot while ESR excites mainly inside the $\approx 3\,\mathrm{mm}$ diameter waist at the cold spot center. Then the two-photon excitation takes place only in the center of the cold spot in the most homogeneous field region while the NMR incoherent excitation is maximum on the edge of the cold spot. Hence the centers of the lines are different due to the different local magnetic fields. In addition, the incoherent line shape strongly depends on the radial magnetic field gradient while the coherent line does not. We found the coherent line width to be independent of temperature and density.

Temperature dependence At relatively high temperatures $\approx 70\,\mathrm{mK}$ both ENDOR lines were observed. However, at lowest temperatures $\lesssim 60\,\mathrm{mK}$ the incoherent line disappeared and only coherent line remained. At the surface gas temperatures of $\gtrsim 80\,\mathrm{mK}$ the coherent line was no longer observed. We suggest that the coherent two-photon excitation occurs only when the surface residency time of 2D atoms is long enough to enabling long interaction time with the excitation fields [P2]. The spectra in fig. 3.4 were recorded at lowest temperatures. In those conditions there was no incoherent line.

Coherent ENDOR line shape Qualitatively the ENDOR line shapes presented in fig. 3.4*a* can be obtained by solving the density matrix equations for the ladder type of level system as is usually done in quantum optics [44]. This work is in progress and will be published elsewhere [102].

3.4 Evaluation of the cold collision shift from data

ENDOR was used as the main method for the measurement of cold collision shift (figs. 3.2*c* and 3.4*a*). Due to its very small width the coherent ENDOR line was used for the determination of the NMR transition frequency. Results of the ENDOR transition frequency as a function of the ESR 2D line shift are shown in fig. 3.5. Relation (2.25) (of paper [P1]) between the NMR line shift $f_{ab} - f_{ab}^0$ and the cold collision shift Δf_{CS}^{2D} was used to extract the experimental results $\Delta f_{CS}^{2D} = -1.0(1) \times 10^{-6}\,\mathrm{Hz\,cm^2} \times \sigma$ and $\Delta A_w = -45.58(4)\,\mathrm{kHz}$ for the cold collision shift and the wall shift. We obtain the dipolar shift ΔB_{dip} from the 2D ESR line shift Δb_{bc}^{2D} as (eq. 2.21) $\Delta B_{dip} = -\Delta b_{bc}^{2D} - h\Delta f_{CS}^{2D}/g_e\mu_B = -7.4(7) \times 10^{-13} \times \sigma\,\mathrm{G \cdot cm^2}$ where $h\Delta f_{CS}^{2D}/g_e\mu_B = 3.6(4) \times 10^{-13} \times \sigma\,\mathrm{G \cdot cm^2}$.

The data for ^{4}He films was collected at different stages of the experiment, *i.e.*, with and without the polarizer and with the decay method. Although the 2D H$\downarrow$ temperature was different at different stages, the shift Δf_{CS}^{2D} was found to be independent on the temperature in the range $T \approx 50 - 90\,\mathrm{mK}$ [P1].

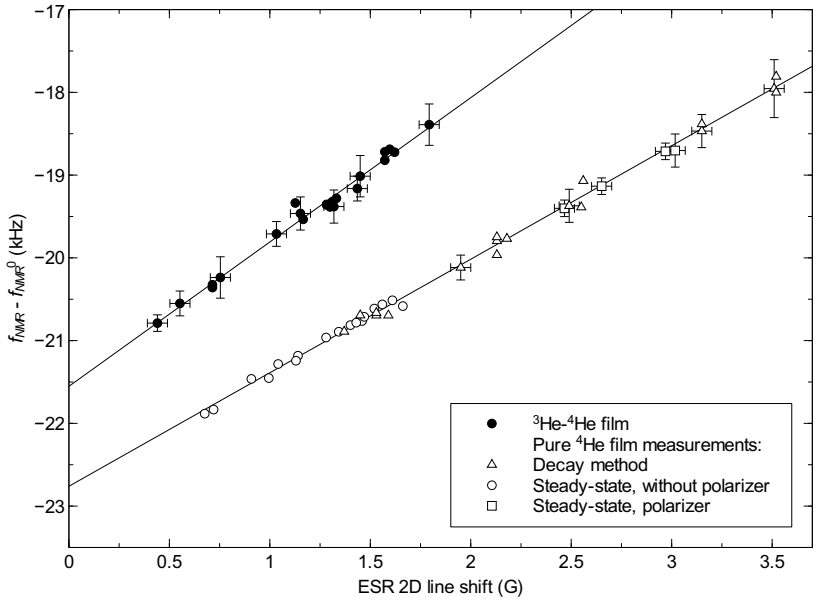

Figure 3.5: The measurements of cold collision shift in 2D H on ^{4}He and ^{3}He-^{4}He films [P1].

In addition, we made measurements with the constant frequency method where also the NMR frequency was fixed and the magnetic field was swept. In this case the bolometer line is used for the determination of the NMR transition field (fig. 3.2*b*). The NMR measurement was found to agree with the ENDOR measurement [P1].

3.5 Discussion

The absence of a large cold collision shift in 2D H↓ was understood in our experiments on the cold collision shift in 3D [P3] and it is discussed in sec. 2.2.3 and 4.5. For ^{3}He-^{4}He films a small increase in the Δf_{CS}^{2D} is observed [P1]. This effect does not seem to result from the scaling approach (sec. 1.4 and sec. 2.2.3), according to which the shift should decrease because of the increased out-of-plane delocalization resulting in a smaller effective 3D density.

Hazzard and Mueller [103] attempted to explain the small (but non-zero) cold collision shift by ripplons on the helium surface mediating interactions between atoms. Safonov *et al.* [104] proposed that the finite cold collision shift could be accounted for by an interstate shift $\Delta f_{CS}^{bc}(\sigma_a)$ due residual a-state atoms acting on the $b-c$ transition and by a density dependent wall shift acting on the $a-b$ transition. The former effect depends on the density of the a-state atoms which

may be present in the gas because of one-body and two-body relaxations. However, ref. [104] falls into error in assuming of the two-body dipolar relaxation rate being anomalously large [15, 96]. Moreover, in our experiments the a-state density varied with and without the polarizer. On the other hand, Safonov *et al.* [104] point out an important fact that the small cold collision shift could be caused by a density dependent change in the hyperfine constant $\Delta A(\sigma)$. The estimate they give amounts only to 1/6 part of the measured value. It is not clear either what kind of effect the reduced binding on the ^{3}He-^{4}He films have on the shift. Our experiments do not give a possibility to verify the suggestion of Safonov *et al.* [104].

Chapter 4

Cold collision shift in 3D H

In this chapter details of the experiments on 3D H are presented. The results were published in paper P3 and their theoretical interpretation stimulated an intense discussion [84, P4].

Background for the collisional shifts in high field magnetic resonance of H is presented in sec. 2.2.3. Motivated by the results with 2D H↓ we designed a similar control experiment for 3D H. Because the ESR lines are relatively wide, typically $\gtrsim 100\,\mathrm{mG}$, one has to carry out the experiment at densities $\gtrsim 10^{17}\,\mathrm{cm}^3$ to observe the predicted shift (sec. 2.2.3). However, ESR on dense 3D H↓ faces the problem of strong radiation damping. Although the effective density of 2D H is even ~ 1000 times higher, one does not run in to the same problem because of the very small filling factor of 2D H in the ESR resonator. The damping problem was solved by a different construction of the sample cell.

4.1 Experimental cell for hydraulic compression

The sample cell used in compression experiments is presented in fig. 4.1. A fountain valve is used to manipulate the liquid helium level in the SC. H↓ gas is compressed by reducing the volume of H↓ by filling the compression volume by liquid helium. This space consists of the so-called buffer and evanescent volumes. Compression factors up to ~ 200 can be achieved by raising the liquid helium level from the fill line outlet to the top of the buffer volume. A channel connects the bottom of the buffer volume to the resonator volume. It was built for testing and calibration purposes since such construction of ESR resonator with evanescent field had not been tested earlier in our laboratory.

The ESR Fabry-Perot resonator follows the common design used in experiments with H↓ in our laboratory [48]. However, a distinctive difference is the the evanescent (field) volume, a small hole of 0.5 mm diameter and 3 mm length made through the center of the flat mirror to the buffer volume situated below. The top of this channel is sealed with a $22\,\mu$m thick Mylar foil glued on the flat

mirror. The hole does not disturb the performance of the FPR significantly because its diameter is much smaller than the wavelength of the mm-wave excitation $\lambda_{ESR} \approx 2.3\,\mathrm{mm}$. Yet, a small fraction of the B_1 field called the evanescent field, penetrates from the FPR to the channel, enabling detection of H at the top of the evanescent volume. The filling factor of H in the evanescent volume is 10^3 times smaller than that of the resonator volume, enabling a linear response of the FPR up to H densities of the order $10^{18}\,\mathrm{cm}^{-3}$ in the evanescent volume [P3].

The fountain valve makes use of the fountain effect in superfluid helium [105]. Thermal link of the fountain reservoir (FR) to the SC is weak, making it possible to heat the reservoir to $\sim 700\,\mathrm{mK}$ while the SC temperature remains at $\lesssim 400\,\mathrm{mK}$. There is superleak in the tube connecting the fountain reservoir and the SC. A temperature difference between SC and reservoir creates a pressure difference across the superleak, resulting in transfer of superfluid helium from the colder side to the warmer side, raising helium level in the latter. The helium height difference below 0.7 K is given by the approximate relation $\Delta h = h_{FR} - h_{SC} = 17\,\mathrm{cm}\cdot\mathrm{K}^{-4}\left(T_{FR}^4 - T_{SC}^4\right)$ [105].

Helium level in the fountain reservoir is measured with a capacitive level gauge which comprises of the outer shield of the reservoir and a thin inner tube. This coaxial capacitor is connected in series with an inductor, providing an LC resonance circuit for a tunnel diode oscillator [106]. The oscillator frequency is inversely proportional to the helium level in the level gauge. The output frequency of the oscillator, typically $\approx 24\,\mathrm{MHz}$, is amplified and heterodyned to frequencies below 1 MHz and finally detected by a frequency counter with 1 Hz resolution. A $\approx 200\,\mathrm{kHz}$ frequency change of the tunnel diode oscillator was observed after filling up fountain reservoir with helium, providing calibration for the level gauge.

Temperature of SC was regulated by a temperature controller. The fountain reservoir did not require separate temperature stabilization and thus reservoir temperature was regulated by applying heat to it manually. The reservoir temperature stabilized within a few seconds after the heat change when the SC temperature remained stabilized. To avoid helium level disruptions, the helium level was changed by sweeping the heating power at such rate that the SC temperature remained constant. The one hour stability of the level gauge turned out to be below 10 Hz, corresponding to $\pm 50\,\mu\mathrm{m}$ level change in the compression region. The reproducibility of the gauge reading was tested by recording the level gauge values versus applied heat after repeated helium level changes. Typically the reproducibility was better than 10 Hz.

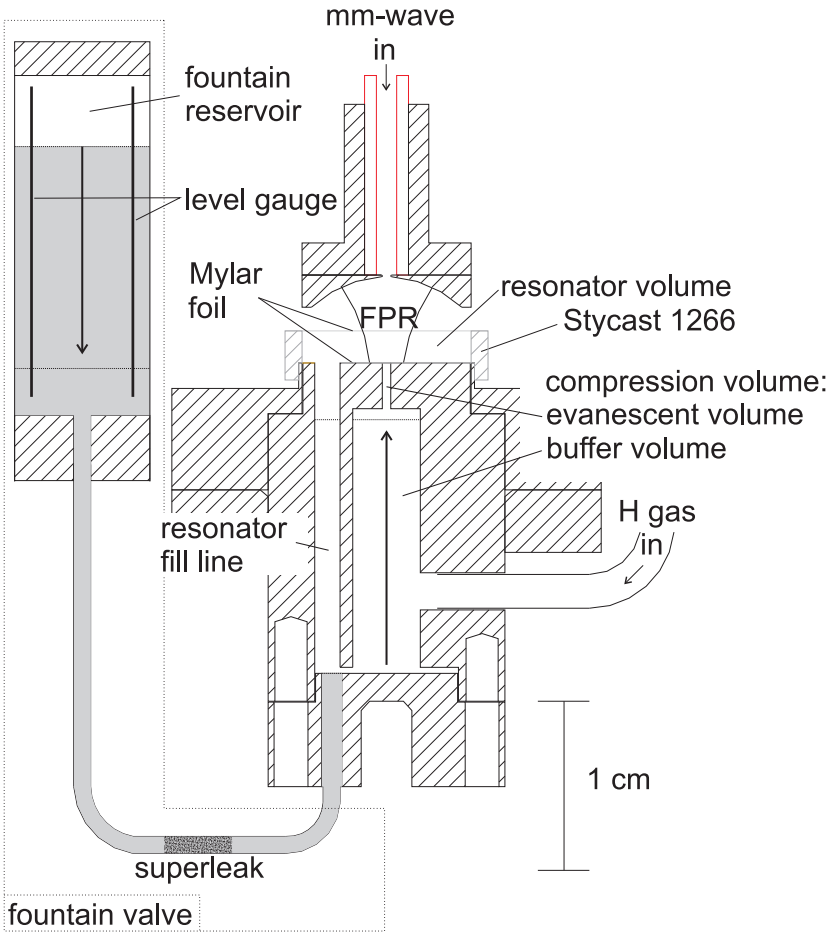

Figure 4.1: Sample cell for hydraulic compressions of 3D H↓. The buffer volume and the evanescent volume form the space (compression volume) where H is compressed. Arrows indicate movements of the helium levels when compressing. By-pass line for the superleak is not shown. The fountain reservoir is not drawn to scale.

4.2 Experimental procedures

4.2.1 Compression procedure

A typical compression sequence was the following: First H↓ gas was loaded to the compression volume. Then the H fill line was closed and the sample was let to acquire nuclear polarization. Compressing a sample with low nuclear polarization too quickly could result in a thermal explosion [32]. Compressions were performed by raising the helium level in the compression volume slowly to avoid U-tube oscillations. After reaching the intended compression level SC and fountain reservoir temperatures were stabilized, thus fixing the helium level difference, and a measurement could began. Three different compression types that depend on the helium level (fig. 4.1) and the compression strength were used:

1. Precompression. The helium level is kept below the evanescent volume. Samples of low density and low nuclear polarization could be studied by this method.

2. Compression to the evanescent volume. This compression is performed so that the liquid does not fill the evanescent volume when the H↓ sample has recombined. These compression were used for the measurement of H↓ density by the level gauge.

3. Strong compression. In the end of the compression helium fills the whole evanescent volume. A H↓ sample may evolve into a bubble before its final collapse.

Measurements with stabilized temperatures and fixed helium level difference allowed extracting the H↓ density or the sample size from level gauge data.

The maximum hydrostatic pressure and thus the density of compressed H↓ was limited by the flow of helium into the resonator volume via the resonator fill line. Appearance of bulk liquid on the flat mirror shifts the frequency of FPR making measurements impossible. When the helium level is less than 1 mm below the flat mirror plane, the film thickness on the flat mirror starts to grow rapidly. Since the total length of the evanescent volume channel is 3 mm, the maximum hydrostatic head of helium before entering the evanescent volume is $h_{hyd} \approx 2\,\mathrm{mm}$, limiting the hydrostatic pressure applied to H to $p_{He} = \rho g_0 h_{hyd}$ and the density of H at 300 mK to $n_H = \rho g_0 h / k_B T \approx 6 \times 10^{17}\,\mathrm{cm}^{-3}$. Here g_0 is the standard gravity and $\rho = 145.47\,\mathrm{kg/m}^3$ is the density of helium. However, compression to the evanescent volume is enhanced due the capillary rise of helium, allowing maximum densities around $10^{18}\,\mathrm{cm}^{-3}$. The additional pressure due to surface tension is given by $p_s = 2\sigma/r$, where $\sigma = 3.54 \times 10^{-4}\,\mathrm{N/m}$ is the surface tension for helium [107] and r radius of curvature of the sample. This produces a 2 mm capillary rise of the helium level in the evanescent volume.

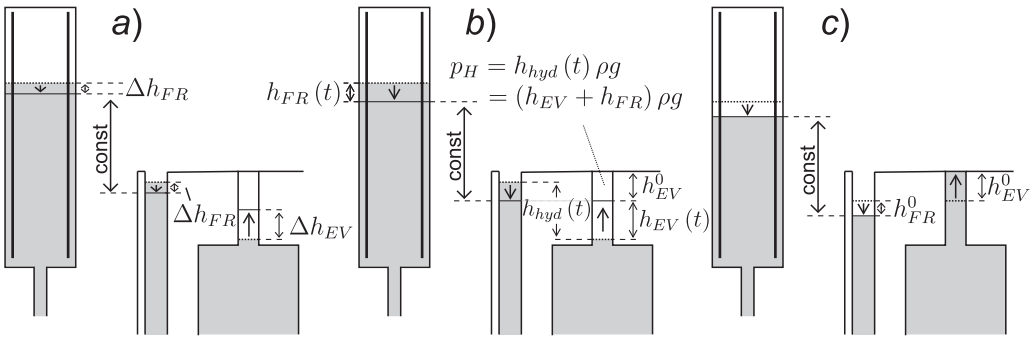

Figure 4.2: Determination of the H density and the He level in the evanescent volume (EV). To fix level height difference temperatures of the SC and fountain reservoir (FR) are kept constant. *a*) Changes in the level heights due to a H↓ pressure decrease Δp_{H}. *b*) Helium level changes during H↓ density decay to $n \to 0$ (fig. 4.3*a* (1)). *c*) Determination of the volume at the end of the compression. (fig. 4.3*a* (2)-(3)). Arrows denote the movement of the He levels, and the dotted and solid lines present the positions of He level respectively in the beginning and end of each step. For simplicity the capillary rise in EV is not shown. When liquid is in EV the capillary rise is 2 mm.

4.2.2 Calibration of H density and sample size

The fountain reservoir (FR) with the evanescent volume (EV) and the fill line form a three-branched U-tube system. Maintaining a fixed temperature difference between FR and SC provides a fixed helium level difference between FR and fill line. The level in the EV may change because of changes in the pressure of the H↓ gas, shifting also the helium level in the fountain reservoir and the fill line.

The H↓ density was calibrated with the type 2 compressions. In such compression helium is in the EV, but does not fill it completely when the H↓ sample has recombined ($n_{\mathrm{H}} \to 0$). First we consider the change of the helium levels in FR and SC during the density decay of the H↓ sample, as illustrated in fig. 4.2*a*. In the beginning of compression H↓ gas has displaced helium from the EV to the other volumes, fill lines and FR. Helium is transferred during the time Δt to EV from the other volumes to compensate for the reduction of the H↓ pressure (Δp_{H}) due to recombination. The volume ΔV_{EV} of helium transferred to EV is removed from the FR (ΔV_{FR}) and fill lines (FL, ΔV_{FL}), thus $-\Delta V_{EV} = \Delta V_{FR} + \Delta V_{FL}$. Because the level difference between SC and FR is fixed, the helium level will decrease by the same amount in both. We obtain the following relation between the helium level changes in the EV and the FR:

$$\Delta h_{EV} \quad = \quad \frac{\Delta h_{FR}\,(A_{FR} + A_{FL})}{A_{EV}}. \tag{4.1}$$

To obtain the change in the hydrostatic pressure acting on H↓ during Δt, which

equals to the H↓ pressure change, we need to account for the helium level change in the fill line and in the evanescent volume (fig. 4.2). The hydrostatic head of helium is $\Delta h_{hyd} = \Delta h_{EV} + \Delta h_{FR}$ and the H↓ pressure change is then

$$\Delta n_H k_B T = \left[\Delta h_{EV} + \Delta h_{FR}\right] \rho_{He} g_0. \tag{4.2}$$

We can simplify the calibration procedure by allowing H↓ to recombine to $n \approx 0$. We define $t_{end} = \infty$ as the time when the pressure (and the corresponding density) of H↓ has decreased to zero. An example of such a measurement recorded by the level gauge is shown in time period (1) of fig. 4.3*a*. We write EV sample height as $h_{EV}(t) + h^0_{EV}$ where $h_{EV}(t)$ is the helium level displacement due to H↓ ($h_{EV}(\infty) = 0$, fig. 4.2*b*). Now we can generalize the equations to obtain the pressure at time t. After substitutions $\Delta h_{EV} \to h_{EV}(t)$ and $\Delta h_{FR} \to h_{FR}(t)$ the pressure $p_H(t)$ becomes

$$p_H(t) = n_H(t) k_B T = \left[h_{EV}(t) + h_{FR}(t)\right] \cdot \rho_{He} g_0. \tag{4.3}$$

The H density extracted from the data of fig. 4.3*a* is presented in fig. 4.3*b*. The density decay of the sample (fig. 4.3) was accelerated by applying high power ESR which leads to recombination of the ESR induced H↑ atoms.

We can extend the measurement to obtain also the $n_H = 0$ position h^0_{EV} of helium in EV. By decreasing FR heating we raise the helium level in EV until it is completely full and then return to the previous heating setting. Due to its surface tension helium remains "stuck" filling the whole evanescent volume. The final height of the sample h^0_{EV} is obtained from the change in the level gauge reading using eq. (4.1). Period (2) of fig. 4.3*a* is an example of such a measurement. The reproducibility of the level gauge is demonstrated in period (3) of fig. 4.3*a*. After filling the evanescent volume the helium level was first lowered to buffer volume to get it out of EV ("unstuck"). Then after returning to the heating in the compression measurement the level gauge returns to the $n_H \approx 0$ baseline. When the whole EV is filled in the $n_H \to 0$ limit, the level gauge data can be used to obtain the absolute height of the sample from eq. (4.1).

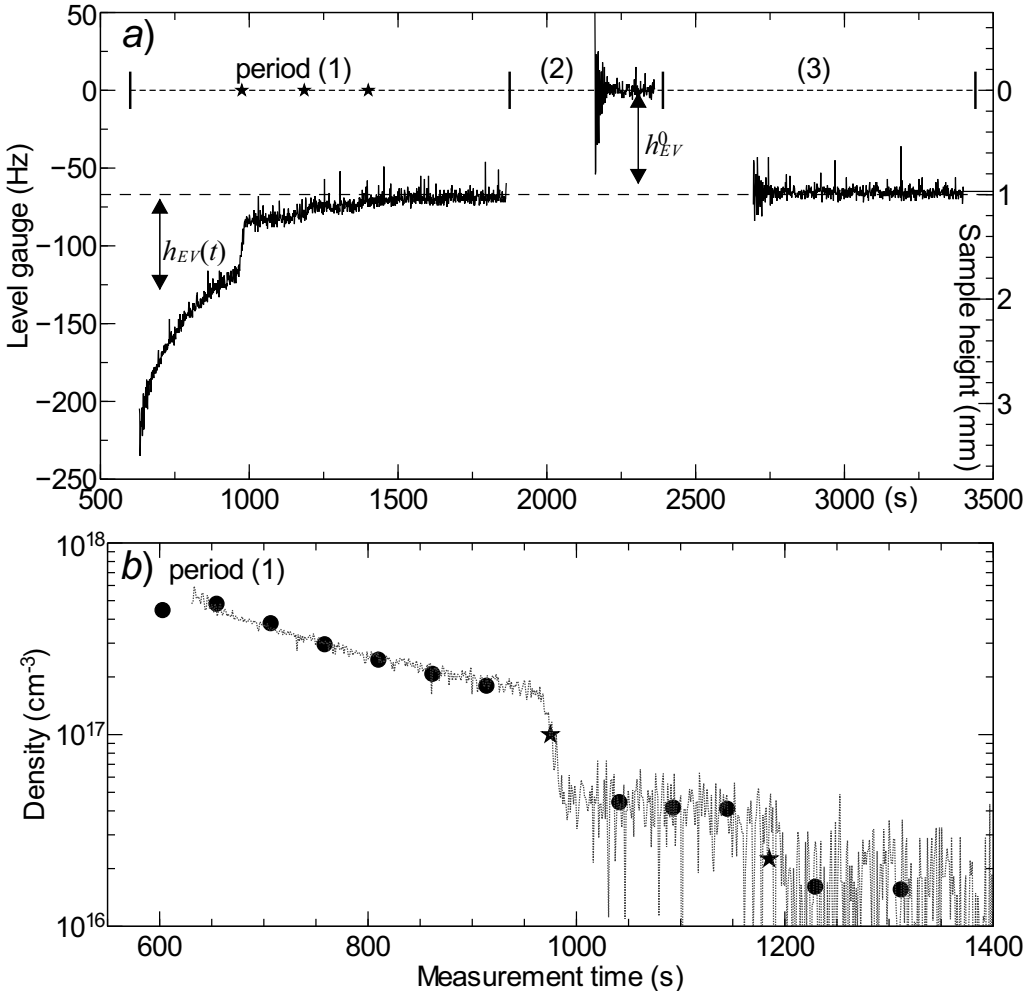

Figure 4.3: *a*) Level gauge data in a compression experiment. Period (1) Recombination of the sample. At the small steps indicated by $\star$ H$\downarrow$ density is reduced by ESR-induced recombination. The end of period (1) yields the $n_H \approx 0$ baseline. (2) Determining the final sample size by filling up the EV with helium. (3) Reproducibility of the $n_H \approx 0$ baseline after removing the liquid from the EV. *b*) Time evolution of H$\downarrow$ density measured by level gauge (trace) and ESR ($\bullet$) in experiment *a*). To obtain an absolute calibration for ESR the relative ESR density was set to match the level gauge density at $1000 < t < 1200\,\mathrm{s}$.

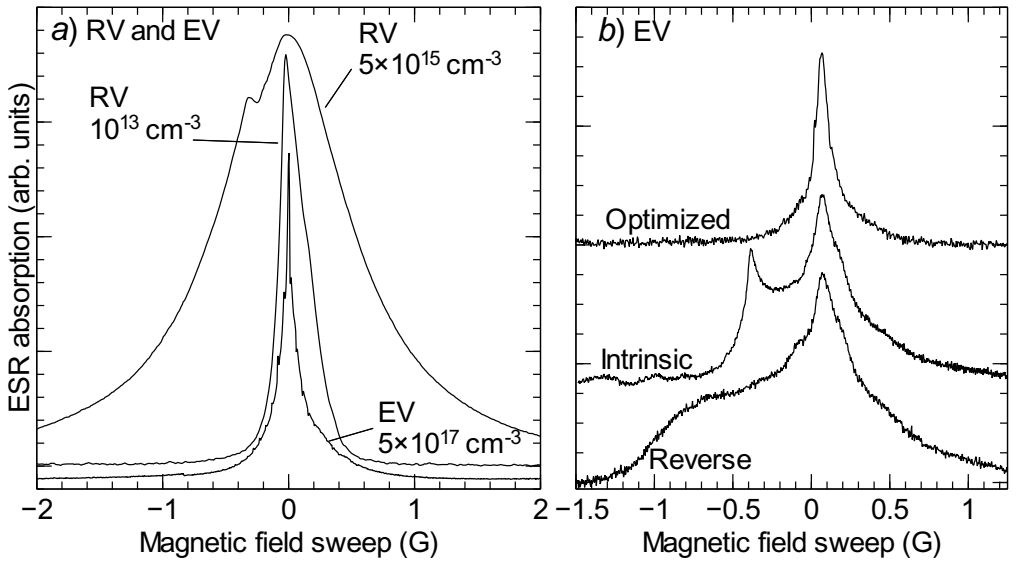

Figure 4.4: *a*) Example ESR spectra for samples in the resonator (RV) and evanescent volumes (EV). *b*) EV line under different field gradients at low density $\approx 10^{16}\,\mathrm{cm}^{-3}$. The middle spectrum was measured in intrinsic gradient without shim coils. Narrowest lines were obtained with an axial gradient of 20 G/cm. Applying the reverse gradient the EV line could be significantly broadened.

4.3 ESR of H in the compression volume

Typical spectra for H↓ in the resonator volume and in the EV are shown in fig. 4.4*a*. Due to the very small spatial size of the EV sample, its ESR line width in the low density limit is three times smaller than the width of the resonator volume sample. The FPR response enters the nonlinear regime already at the H density of about $10^{15}\,\mathrm{cm}^{-3}$ in the resonator volume, significantly broadening and distorting the ESR line (fig. 4.4*a*).

An extra complication for ESR in EV was caused by magnetization of the sample cell body. Diamagnetic effects of the copper around EV can be calculated by integrating the field due to the equivalent magnetization surface current density $\mathbf{J_{ms}} = \mathbf{M} \times \hat{n}$ [108]. Here $\hat{n}$ is a unit vector normal to surface and $\mathbf{M}$ is the magnetization vector. In this approach most of the gradient is caused by a small 0.5 mm diameter solenoid on EV surface. Thus the copper produce a rather strong gradient at the ends of EV. A spectrum for H↓ in EV broadened by this "intrinsic" gradient is shown in fig. 4.4*b*. The homogeneity of the field could be improved with the help of shim coils which generate an extra axial gradient (fig. 4.4*b*). The smallest line widths obtained by such an optimization were about 50 mG. We could also apply a strong axial gradient to image the axial profile of B_1 field (fig. 4.4*b*). We measured that the ESR B_1 field extends about 0.2 mm in to EV below

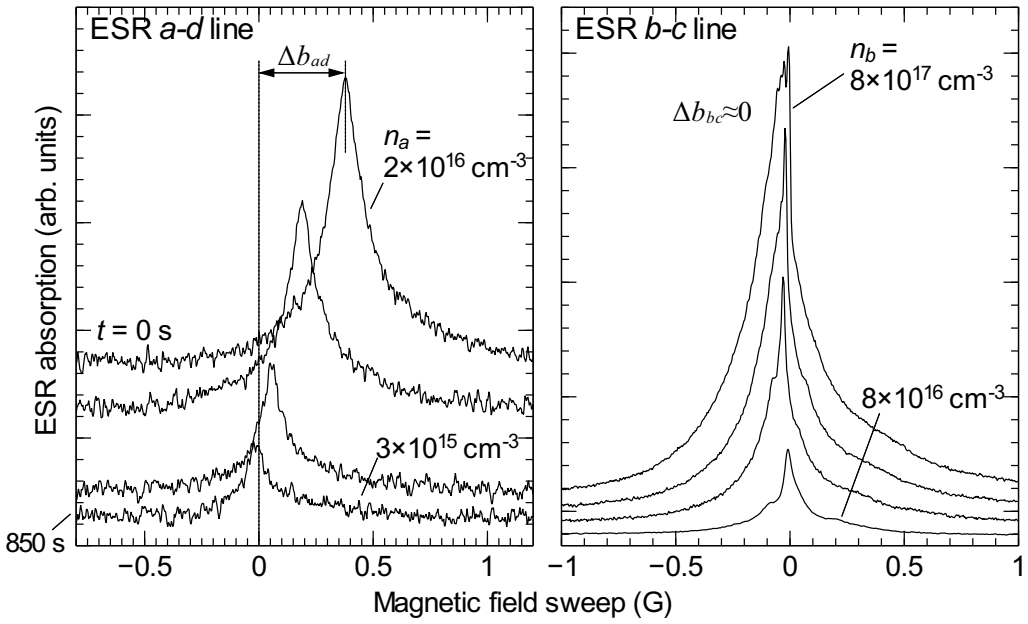

Figure 4.5: Evolution of ESR $a-d$ and $b-c$ transition spectra in a compression. The spectra were recorded at $\approx 210\,\mathrm{s}$ intervals.

the Mylar film.

At high densities $> 10^{17}\,\mathrm{cm}^{-3}$ another effect limited the accuracy of finding the line positions (see fig. 4.5, right panel). The line shapes were modulated by a structure resembling spin waves [109]. The spin wave "spectrum" was observed to depend on field gradient, sample height and density [P5]. The analysis of spin waves is not within the scope of this work. However, the accuracy of finding the line position for $b-c$ transition is limited by the spin waves.

4.4 Measurement of the cold collision shift

ESR spectra of the $a-d$ and $b-c$ lines during identical compressions are presented in fig. 4.5. It is seen that similar to the 2D experiments the $b-c$ line is not shifted hardly at all. On the contrary, the $a-d$ line exhibits a rather large shift.

As discussed in chapter 2 and sec. 2.6.2, the ESR lines can be shifted due to atoms in both a and b hyperfine states, *i.e.* by interstate and intrastate collisions. For example, the $b-c$ line is shifted by interstate collisions $b+a$ and intrastate collisions $b+b$. Similar shifts contribute to the $a-d$ line position. Then the cold collision shifts in magnetic field units for the ESR $a-d$ and $b-c$ transitions are

$$\Delta b_{ad} = C_{aa} n_a + C_{ab} n_b \tag{4.4}$$

$$\Delta b_{bc} = C_{bb} n_b + C_{ba} n_a. \tag{4.5}$$

The terms $C_{aa}n_a$ and $C_{bb}n_b$ account for the intrastate shifts and the terms $C_{ba}n_a$ and $C_{ab}n_a$ for the interstate shifts, *e.g.* $C_{ab}n_b = (-h/g_e\mu_B)\,\Delta f_{CS}^{ad}\,(n_b)$ (cp. eqs. (2.9)-(2.10), and eqs. (2.20)-(2.21)). It turns out that the intrastate coefficients C_{aa} and $C_{bb} \approx 0$ are much smaller than the interstate ones C_{ab} and C_{ba} [P3]. The dipolar interaction is neglected here and its effect is included in the error bars of the results. It produces a small contribution $-\Delta B_{dip} n \lesssim -5 \times 10^{-20} \times n\,\mathrm{G{\cdot}cm^3}$ (eqs. (2.20) and (2.21)), which is equal on both lines and proportional to the total density $n = n_a + n_b$ and depends on the sample shape (sec. 2.3.2).

The determination of some of the coefficients in eqs. (4.4) and (4.5) can be simplified by changing the nuclear polarization of the sample. By varying the gas temperature, compression speed and final density we could manipulate the ratio n_b/n_a in the range from about 5 to 1000. In the case of maximum n_b/n_a and the $b-c$ transition the term $C_{ba}n_a$ can be neglected in eq. (4.5) and we obtain C_{bb}. In another case, having not so high n_b/n_a so that $a-d$ transition is discernible, we measure the shift of $a-d$ transition as a function of b-state density. Now we can neglect $C_{aa}n_a$ in eq. (4.4) because $n_a \ll n_b$ (also because $C_{aa} \ll C_{ab}$). For samples of low polarization, composed of a mixture of atoms in the a and b hyperfine states (compression type 1, precompression), the shift constants for each transition were extracted from a multiple linear fit with two fitting parameters C_{aa} and C_{ab} to eq. (4.4) or C_{bb} and C_{ba} to eq. (4.5).

However, during a single compression experiment ESR spectra can be recorded only for either $a-d$ or $b-c$ transition. This is because changing the magnetic field from B_{ad}^0 to B_{bc}^0 or vice verse between the ESR transitions spoils the line position measurement and the temperature stability. Therefore, to find out both a- and b-state densities, we performed separate identical compression sequences with the field tuned to $a-d$ and $b-c$ transitions.

The results of the cold collision shift measurements are presented in fig. 4.6. The shift $\Delta b_{bc}\,(n_b)$ in doubly polarized gas of b-state atoms, which was found to be very small, yields the intrastate coefficient $C_{bb} = 2(2) \times 10^{-20}\,\mathrm{G{\cdot}cm^{-3}} \approx 0$. The shifts of $b-c$ and $a-d$ lines in a mixture of a and b state atoms were found significant. Because of the relatively fast recombination of the a-state atoms measurements for $n_a \sim n_b$ were limited to densities $n_a \lesssim 5 \times 10^{16}\,\mathrm{cm^{-3}}$ and $n_b \lesssim 2 \times 10^{17}\,\mathrm{cm^{-3}}$. Then we obtained the shift coefficients $C_{ba} = C_{ab} = 8(2) \times 10^{-19}\,\mathrm{G{\cdot}cm^{-3}}$ and $C_{aa} = C_{bb} = 5(5) \times 10^{-20}\,\mathrm{G{\cdot}cm^{-3}}$. Because of the vanishingly small intrastate shift, the intrastate density dependences for $\Delta b_{bc}\,(n_a)$ and $\Delta b_{ad}\,(n_b)$ in fig. 4.6 are neglected. Finally we measured the shift $\Delta b_{ad}\,(n_b)$ of the $a-d$ transition at very high b-state densities. The shift coefficient was found to be $C_{ab} = 7(1) \times 10^{-19}\,\mathrm{G{\cdot}cm^{-3}}$.

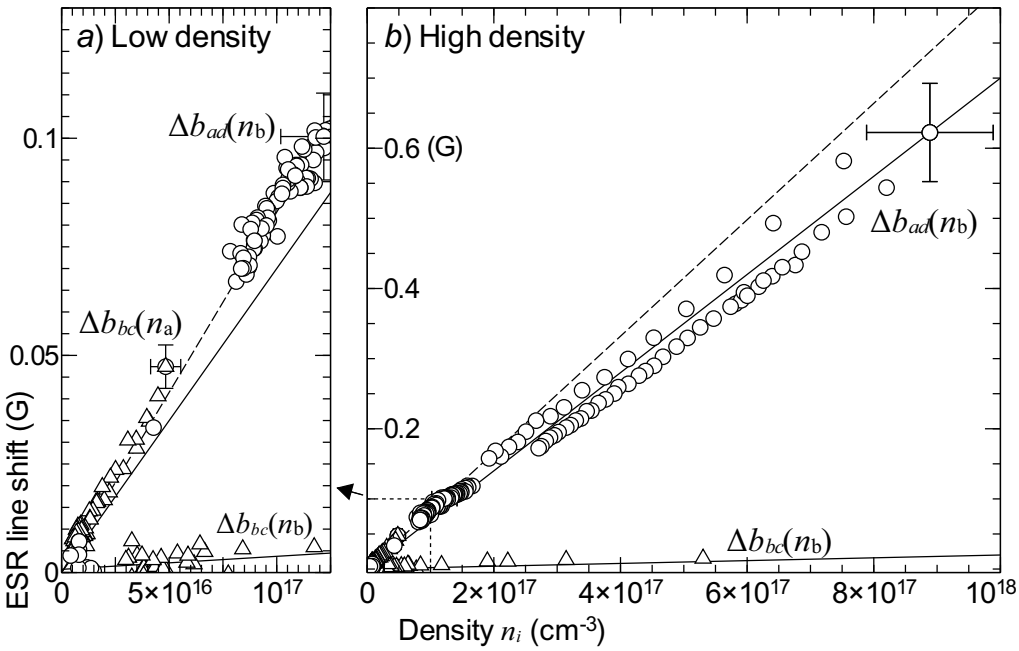

Figure 4.6: Measured density variations of the cold collision shifts [P3]. The solid lines represent fits to the data. The dashed lines are a fit to the low density data.

4.5 Discussion

Theoretical interpretation of our results has been given in papers P3 and P4 and by Safonov *et al.* [83, 84]. The conclusions are summarized in sec. 2.2.3. Using the interstate shift coefficient $C_{ab} = C_{ba}$ and the revised theory (sec. 2.2.3 and sec. 2.6, and eqs. (4.4) and (4.5)) the relation

$$C_{ab} = C_{ba} = \frac{1}{2}\frac{1}{g_e\mu_B}\frac{h^2}{\pi m}(a_t - a_s) \tag{4.6}$$

gives the scattering length difference $\Delta a = a_t - a_s \approx 30(5)\,\mathrm{pm}$. The intrastate shift vanishes because the ESR excitation produces a coherent superposition of spin states interacting via the triplet potential only.

Eq. (4.6) is due to Safonov *et al.* [84] who found an error in [P3]. A possible explanation why [P3] is valid in our case is given in [P4]. According to [P4] $\Delta a = a_t - a_s \approx 60(10)\,\mathrm{pm}$ (the constant $\frac{1}{2}$ is replaced by $\frac{1}{4}$ in eq. 4.6) which is in better agreement with theoretical values ranging from $\Delta a = 40\,\mathrm{pm}$ to $80\,\mathrm{pm}$ [20, 21]. Experiments do not yet allow to conclude which theory is correct but are hoped to do so in future [110]. Also theoretical calculations of the scattering lengths have recently received attention [20, 21].

The experimental cell demonstrated the usability of our setup in ESR studies of high density H↓ in a strong magnetic field. However, the setup had some drawbacks which should be removed for future experiments. The magnetic field of the magnet drifted relatively much in the persistent mode reducing the accuracy of the line position measurement. Actually the drift has been already reduced at least by three orders of magnitude with a new magnet. Another disadvantage was the poor homogeneity of magnetic field in the evanescent volume due to the magnetization of the cell body. Increased homogeneity would result in narrower resonance lines, also improving the accuracy of finding the line positions. Removal of the resonator volume would make stronger H↓ gas compression possible. Experiments with described setup are currently taking place [110].

Chapter 5

Experiments with H in H_2

In this chapter we present the experiments with atomic hydrogen in solid molecular hydrogen. Results of the first experiments were published in paper P6. Results of the second experiments were published in papers P7 and P8. Paper P8 contains a more detailed description of both experiments and general discussion of the results. The introductory part of this chapter is divided into two sections, the first one considers H in H_2 from the viewpoint of quantum solids and the second from the perspective of matrix isolation. Then a general introduction to the experiments is presented. In the end we discuss an improved sample preparation method.

5.1 Introduction to quantum solids

At low temperatures the lightest elements form solids which have unique properties compared to solids formed by heavier elements. In the light solids the attractive forces are weak compared to the zero-point energy. One may expect to observe quantum effects in them, and that is why they are called quantum solids. A measure of their quantum nature is given by the ratio of the zero-point energy to binding potential, characterized by the quantity $\Lambda = h/b\sqrt{m\epsilon}$ named according to de Boer who considered solids with weak interactions and small mass [111]. Here b and ϵ are parameters which determine the potential energy of the interaction. The de Boer parameter is largest for helium and hydrogen isotopes and therefore those solids are the most promising for the search of quantum effects. Even though H_2 is lighter than He, due to the weaker binding potential the de Boer parameter is largest for helium, $\Lambda = 3.0$ for ^{3}He and 2.6 for ^{4}He. For H_2 and D_2 the de Boer parameters are 1.7 and 1.2, respectively. Another measure for "quantumness" can be seen in the motion of the atoms or molecules due to the zero-point energy. For ^{4}He amplitude of the zero-point motion is 25% of the lattice constant and for H_2 18% [23].

In the late 1960's several authors considered the behavior of defects in quantum solids. To explain experimental observations in solid ^{3}He, Hetherington proposed

that vacancies were delocalized and should be considered as wave-like excitations [112]. Guyer and coworkers performed thorough studies of tunneling and exchange reactions of atoms and vacancies in solid ^{3}He [113] and Andreev and Lifshitz presented a general theory of defects in quantum solids [19].

In the consideration of Andreev and Lifshitz, a defect may be a vacancy, impurity or dislocation [19]. At low temperatures, where thermally activated motion is suppressed, a defect may still move via tunneling. The properties of the crystal and the defect define the tunneling probability and the bandwidth Δ of the tunneling motion. In a perfect crystal energies in neighboring sites are equal, leading to band motion and delocalization of defects in the crystal. Such defects are called defectons, and they may behave like an ideal gas in the crystal. It was suggested [19] that the defects might reach quantum degeneracy and become superfluid at low enough temperatures.

During the same time period several authors considered quantum effects in solid helium in successive works [114, 115, 116]. Chester showed that a Bose-Einstein condensation can occur in solid [114] and Leggett proposed to search for superflow by measuring the rotational inertia of the solid [115]. Below the transition temperature the condensed fraction should decouple from the motion of the rest of the sample. Guyer examined the problem on the basis of experimental data and concluded that BEC would occur at temperatures well below 0.1 mK [116].

An experimental observation of supersolidity in ^{4}He was claimed three decades later by Kim and Chan using a torsion oscillator [117, 118]. They observed a decrease in the mass taking part in the oscillation at $T \sim 100\,\mathrm{mK}$ and associated this with the decoupling of a superfluid component from the motion, often referred to as non-classical rotational inertia (NCRI). Since the observations of Kim and Chan there has been an explosive growth of experimental and theoretical work and the phenomenon has been confirmed by several groups. Anomalies have been observed also in the specific heat and elastic moduli of solid helium [119, 120]. So far the microscopic origin of the superfluidity remains unclear. One recent experiment suggests that the phenomenon could be related to a superglass phase [121] while other work questions the relation to superfluidity [122]. Reviews on the experiments and theory have been published for example in the refs. [123, 124, 125].

Although most experimental and theoretical efforts have been directed to helium, solid H_2 is also a good candidate to exhibit quantum effects [23]. Fast movement and clustering of o-H_2 impurities by quantum tunneling takes place in p-H_2 at $< 1\,\mathrm{K}$ [126]. The helium experiments motivated similar work on H_2 where also an anomaly was observed but it was attributed to movement of o-H_2 [127, 128]. Also new theoretical studies of H_2 have been conducted [129, 130, 131]. The conclusions do not seem to favor supersolidity but one should keep in mind that there also remains a good deal of controversy in the theory of supersolidity in helium.

In this work we study the system of H atoms embedded in solid H_2. Also H atom impurities can move in the H_2 matrix by tunneling [22, 132]. In the theory of Andreev and Lifshitz [19], H atoms can be considered as quasi-vacancies or impurities in H_2. Thus delocalization of the atoms by fast quantum tunneling might initiate quantum collective phenomena. Beneficial features of the system are the small mass of H and the possibility of direct studies by magnetic resonance. For Bose-Einstein condensed atoms changes in the ESR are expected. From the viewpoint of matrix isolation H in H_2 is one of the simplest among such systems.

First direct studies of H in H_2 at subkelvin temperatures are presented in this thesis. Already our initial work revealed interesting effects [P6]. Below 1 K the recombination rates were found slower than predicted by theory and at $< 0.2\,\mathrm{K}$ atoms were found to be stable for at least two weeks. The steady-state populations of the hyperfine states were found non-thermal and the relaxation time of the forbidden $a - c$ transition was found to be close to that of the allowed transitions. As an explanation it was argued that the H atoms could be Bose-Einstein condensed and this possibility was also considered by Hazzard and Mueller [133]. Unfortunately, there exist only a few theoretical studies of H in H_2. According to Danilowicz and Etters binding of H atoms to the H_2 lattice is stronger than binding of H_2 molecules [134]. H atoms induce also stress and distortions in the H_2 lattice [134, 135]. The mobility of H in H_2, which determines the possibility of superfluidity, was not considered in those works and remains still an open question. Future experiments are hoped to clarify the matter.

5.2 Historical overview of experiments with H in H_2

Trapping of radicals in a solid matrix was demonstrated by Lewis and Lipkin in 1942 [136] who split molecules in a solid to radicals and ions by photodissociation. Whittle *et al.* suggested the matrix isolation method for experimental studies of unstable species [137]. They produced samples by condensing a beam of unstable species and the stabilizing matrix species on a cold substrate. The solid matrix prevents trapped species from approaching and reacting chemically [4].

H atoms were first trapped in solid H_2 at liquid helium temperatures by Jen *et al.* [1] and shortly later in several noble gas matrices [2]. The samples were produced similarly to Whittle *et al.* [137] and diagnosed with ESR providing data on the spectroscopical constants. Adrian presented a general analysis of the results and deduced that H atoms in H_2 were located on substitutional sites [94]. Splitting of ESR lines for H in rare gas matrices was interpreted in terms of multiple trapping sites of H [94, 138].

Another method for obtaining H atoms in H_2 is dissociation of molecules *in situ* in the solid by irradiation. Brown *et al.* studied accumulation of atoms and small free radicals in molecular matrices including H_2 by gamma-ray irradiation [3]. Sharnoff and Pound used a different approach [139] where the β-decay of tritium impurities, mixed in small amounts to D_2, produced atoms by electron

impact dissociation. Later the method has been employed using different electron sources [140, P8].

The first studies of H in H_2 were motivated by the search for better chemical fuel and studies of the basic properties. Approximately 10% of H in H_2 is required to produce the same energy per mass unit by H recombination as by oxidation of H_2 [4, 141]. Although the realization of a rocket propellant containing atomic impurities seems vague and unprofitable, they have been considered even recently [141, 142]. Experiments of the groups of Lukashevich in Moscow and Miyazaki in Nagoya in the beginning of 1980's were motivated by quantum tunneling of atomic impurities in molecular matrices. The primary tool to study diffusion of H in H_2 was recombination of H. Although the two groups produced their samples by different methods, the Moscow group by flash condensing and the Nagoya group by γ- and x-ray irradiation, the properties of the H in H_2 samples were found similar [143, 144]. The maximum densities of H in H_2 achieved by these techniques were typically limited to $3 \times 10^{18}\,\mathrm{cm}^{-3}$ [143] and $1 \times 10^{17}\,\mathrm{cm}^{-3}$ [145]. Katunin *et al.* observed a change in the temperature dependence of the recombination rate for H in H_2 below 5 K [132] and inferred this as a crossover from thermally activated diffusion to quantum diffusion. Below 4 K the recombination rate was linear, in agreement with the theory of quantum diffusion in irregular crystals by Kagan *et al.* [146, 22]. The group of Gordon in Chernogolovka found the isotope exchange reaction $D + HD \rightarrow H + D_2$ in hydrogen-deuterium matrices [147]. The Nagoya group performed thorough studies of tunneling exchange reactions in hydrogen-deuterium solids [148, 149]. Later Kumada studied the mechanism of the motion of H in H_2 [150]. The observed insensitivity of the recombination rate to applied pressure suggesting that instead of physical exchange $H_2 \leftrightarrow H$ the atoms move via the chemical exchange reaction $H + H_2 \rightarrow H_2 + H$ similarly to HD [147, 148, 151].

Souers and coworkers were interested in the highest achievable densities of H in H_2 for a possible application of polarized target in a fusion reactor. In their first experiments they created H impurities by running an rf discharge in solid H_2 and observed signs of fast macroscopic diffusion of H atoms over a distance of 1 cm [152]. Later Souers *et al.* continued the work of Sharnoff and Pound [139] on the accumulation of atomic impurities in H_2, D_2 and in T_2 by the tritium β-decay. The highest density of H in H_2 they reached was of $\approx 7.2 \times 10^{18}\,\mathrm{cm}^{-3}$ (270 ppm) at 1.3 K [153]. However, the T_2 concentration was ~ 70 times larger than the concentration of H so that one cannot disregard the effects of T_2 on the sample properties.

Before our experiments the only H in H_2 work performed at temperatures below 1 K was reported by Webeler [154] who carried out calorimetric studies of H_2 with 0.1% T_2 down to 0.2 K. After storaging the samples for a period of time at $0.2 - 0.8\,\mathrm{K}$, an abrupt heat release was observed. This was attributed to a prompt recombination of hydrogen atoms once their density exceeded a critical value dependent on the storage temperature. On the basis of studies of the sample evolution Rosen [155] and Zeleznik [156] estimated that the maximum density

in the Webeler's experiments [154] had been 5×10^{17} cm^{-3} and predicted that densities over 10^{20} cm^{-3} could be stable at temperatures around 0.1 K. Despite these promising predictions, only one continuation experiment was reported suggesting densities close to 10^{20} cm^{-3} below 0.1 K [157]. Collins *et al.* observed similar heat releases in tritiated D_2 and in T_2 but not in tritiated H_2 [153, 158]. They performed the experiments at above 1 K, which seems to indicate that in the experiments of Webeler [154], the H atom densities were higher than 7×10^{18} cm^{-3} reported by Collins *et al.* [158, 153]. At present these analysis and predictions in refs. [155, 156, 157] look erroneous because the recombination of H was considered to be thermally activated. The quantum tunneling of H in H_2 was not considered at that time.

Kagan *et al.* developed a theory of quantum diffusion in irregular crystals [22, 146, 159]. If the energies of neighboring sites in crystal differ more than the band width of tunneling motion Δ, coherent tunneling, which would occur in perfect crystal, is destroyed. Lattice phonons may still mediate incoherent tunneling. Because the density of phonons depends on temperature, so does the rate of incoherent tunneling. In practice incoherent tunneling dominates at intermediate temperatures but at higher temperatures thermally activated diffusion takes place.

Kagan applied the theory to diffusion of ^{3}He in ^{4}He and recombination of H in H_2 [22]. The studies of ^{3}He in ^{4}He were performed in a wide range of impurity concentrations and temperatures [160]. At low density and low temperature diffusion exhibits the band character. At high density ^{3}He atoms become localized and the diffusion rate is significantly reduced. However, the systems H in H_2 and ^{3}He-^{4}He are different. It turned out to be impossible to measure pure spatial diffusion of H in H_2 [161, 162, 145]. The recombination loss rate was the quantity typically extracted from the measurements, but since the atoms have to approach close to each other in order to recombine, this cannot be used to characterize the pure spatial diffusion and to determine Δ.

A review on atomic impurities in H and D matrices, with an emphasis on experiments with impurity-helium condensates, has been published by Khmelenko *et al.* [163]. A review of the work by the Nagoya group has been published by Miyazaki [164].

5.3 Our experiments

In connection of our 2D H$\downarrow$ experiments we discovered a novel method for creating samples of H in H_2 at temperatures below 0.5 K [18, P6]. It turned out that H atoms were trapped in the H_2 layer covering the sample cell walls due to recombination in the gas phase. Direct studies of H in H_2 were found to be possible in the setup used for studies of gas phase H$\downarrow$. The lowest temperature was limited to 100 mK by the available refrigerator making it possible to reach lower temperatures in future experiments. The first experiments (exp. I) were performed in the SC (sec. 3.1) used for studies of 2D H [12, P1]. ESR lines of H in H_2 were found

already in the first thermal compression SC [40, 100] but they were too weak for systematic studies. In the second experiments (exp. II) we reached over 30 times higher H densities utilizing the electron impact dissociation of H_2 molecules *in situ* in solid [P7, P8].

In experiments with gas phase H a layer of H_2 is formed on the SC walls as a result of recombination. This layer helps to improve the stability of the H gas by reducing nuclear relaxation. It is usually deposited in the beginning of each experiment by directing the maximum available flux of atoms into the sample cell and letting the atoms recombine [12, 33]. Prior to our experiments with 2D H↓ [12] H atoms had never been observed in H_2 layers [37, 47]. In order to get atoms captured in the H_2 film, they must acquire enough energy ($\approx 40\,\mathrm{K}$) to penetrate through the helium film [15]. First we assumed that collisions of atoms with excited H_2 molecules in the gas phase provide such an energy [P6]. Later we concluded that this was not the case since in exp. II no H in H_2 was detected after similar coating procedures [P8].

The sample cell in exp. II did not have the thermal compression feature. Recombination occurred mainly via the two-body process, not via the three-body mechanism as before in exp. I. Therefore we suggested that the "third" atom in three-body recombination $b + b + b = H_2 + H$ gains enough energy to penetrate through the helium film. Later this assumption has been confirmed by the observation of H accumulated in H_2 as a result of compressions of 3D H↓ [110] where three-body recombination is again the main atom loss mechanism [15, 32].

Since there was no three-body recombination in exp. II, we had to find another method to obtain H atoms in H_2. We then tried electron impact dissociation of H_2 *in situ* in the solid [P7, P8]. We used the principle of cryogenic dissociators which employ low energy electrons to dissociate H_2 [45, 46]. This method has been employed previously to dissociate H_2 molecules into atoms in solid H_2. In tritiated hydrogen 5.7 keV electrons emitted in the tritium β-decay are already available inside the sample [139, 153, 154]. Also other sources with much higher energy electrons of 160 keV [140] and 40 MeV [165] have been used. In our method low-power cryogenic rf discharge yields much lower energies, of order 100 eV [P8].

5.4 Experimental cells

Experiment I was performed in the sample cell designed for the studies of 2D H (sec. 3.1). To measure the H_2 film thickness the bolometer was replaced with a quartz microbalance. For exp. II we built a new SC shown in fig. 5.1. The main features are similar to exp. I but the cold spot was removed and the size of the SC was increased. The larger SC diameter became possible due to the larger bore of a new superconducting magnet. Also the field homogeneity and stability of the new magnet are better.

The construction of the FPR in the new SC is similar to the previous experiments but the spacing between the two mirrors was increased to be able to fit

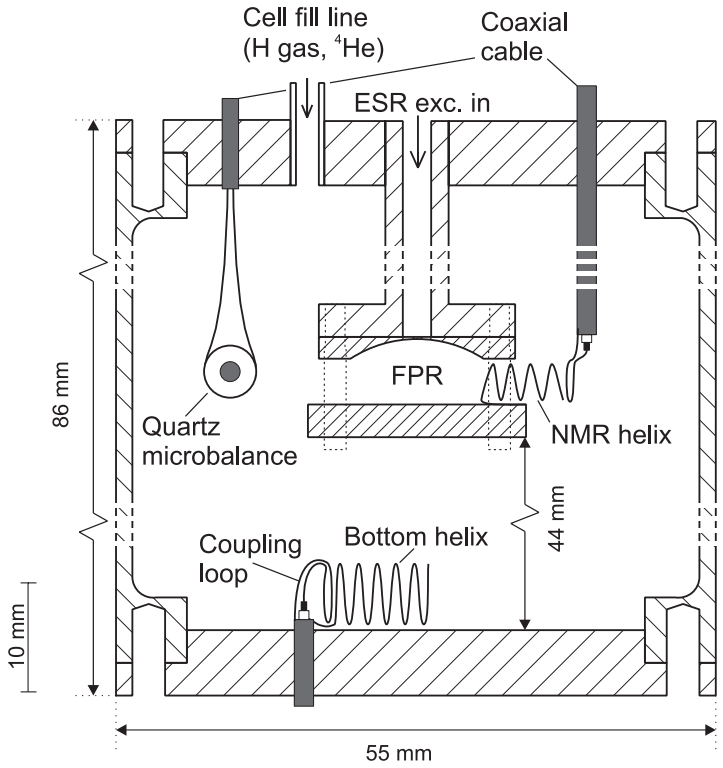

Figure 5.1: Sample cell in the experiment II.

the NMR helix. In exp. I the cold spot surface was Mylar while the spherical mirror was coated with Stycast 1266 epoxy [12]. H in H_2 samples were formed on both surfaces and their properties were found similar. In exp. II the spherical mirror was made of pure Cu and was left uncoated. A 10 μm Mylar foil was glued on the flat mirror in order to realize a smooth surface. The spherical mirror had presumably a much larger surface roughness than the flat mirror. Also embedded magnetic particles could remain in copper after machining [P8]. In contrast to exp. I, the properties of the H in H_2 samples located on each mirror were now found different (sec. 5.6.1) [P8].

In addition to the NMR helix we equipped the sample cell of exp. II with a second helical rf resonator placed on the SC bottom (bottom helix, fig. 5.1). Both helices were used to run rf discharges dissociating H_2 in the solid film covering the SC surfaces. As before, the thickness of the H_2 film was measured with a quartz microbalance.

5.5 Influence of solid matrix on magnetic resonance spectra

5.5.1 Change in hyperfine interaction

For impurity atoms in solids the change in the hyperfine interaction ΔA_{solid} is much larger than for H$\downarrow$ gas discussed before. This is due to the shorter distances of the atoms to the neighboring molecules. H atom impurities have been studied in a variety of solid matrices [2, 138, 166]. The sign of ΔA_{solid} was found to be sensitive to the type of the trapping site while the magnitude depends on both the host matrix and the trapping site [2, 94]. For interstitial impurities ΔA_{solid} is expected to be positive due to Pauli repulsion dominating over van der Waals attraction whereas for substitutional impurities the latter is larger and the shift is expected to be negative [94]. Splitting of ESR lines for H in rare gas matrices was interpreted to be due to occupation of several trapping sites [138, 167]. Because of the large hyperfine interaction change in solids and its sensitivity to atom's surroundings, the observed magnetic resonance (NMR) line width presumably reflects the quality of the solid [94]. In a disordered solid there is a broad distribution of possible hyperfine interaction values and this causes line broadening.

In addition to the atomic hyperfine interaction, there is an interaction of the electron with neighboring magnetic nuclei, known as superhyperfine interaction. Because the probability density for electron of an impurity atom at the neighboring nuclei is much smaller than at atom's own nucleus, the resulting hyperfine constant changes are smaller. Consequently the superhyperfine structure is superimposed on the hyperfine structure [166]. Splitting of the resonance lines due to superhyperfine interaction has not been observed in our experiments.

Table 5.1 summarizes the hyperfine interaction constants for H in H_2 obtained in different experiments. To illustrate the effect of matrix and lattice site we present the values for D in D_2, and for H in argon and krypton matrices. Adrian considered the effects of environment [94] but his analysis is rather qualitative and does not give accurate numbers. Kiljunen *et al.* [167] calculated hyperfine interaction constants for different lattice sites of H in rare gas matrices. To our knowledge, there are no similar calculations for H in H_2 where extra complications may appear due to the "softness" of H_2. Li and Voth argued that an interstitial H atom in H_2 has a local environment similar to a substitutional H atom [135].

The values $\Delta A_{solid} \approx -1.5\,\mathrm{MHz}$ [P6, P8] $-3.5\,\mathrm{MHz}$ [P8] obtained for H in H_2 in our experiments could be detected by both ESR and NMR. Because the hyperfine constant contribution to the resonance frequency is much larger for NMR than for ESR, the former is a more accurate tool to measure changes in A_h.

	A_h (MHz)	$\Delta A/A_h$ (%)	g_e	Ref.
free electron			2.002 319 304	[54]
free H	1420.405 751	0	2.002 284	[54]
H in H_2	1417.11(20)	-0.23	2.002 3	[2]
H in H_2	1418.6(4)	-0.13	2.002 2(2)	[139]
H in H_2	1419.09(1)	-0.093	-	[P6, P8]
H in H_2	1417.34(1)	-0.216	-	[P8]
free D	327.384 352	0	2.002 284	[54]
D in D_2	326.431	-0.29	2.002 202	[168]
H in Ar				
interstitial H	1436.24	1.15	2.001 61	[138]
substitutional H	1413.82	-0.46	2.002 20	[138]
H in Kr				
interstitial H	1427.06	0.47	1.999 67	[138]
substitutional H	1411.79	-0.59	2.001 79	[138]

Table 5.1: Hyperfine interaction constant and electron g-factor for H in different matrices. To illustrate the effect of matrix and trapping site the values for D in D_2 and for H in argon and krypton matrices are presented. We did not observe H in H_2 line shifts from the free gas line due to g_e change [P6, P8]. Note that the numbers for free H, D and electron do not represent full precision.

5.5.2 Change in g-factor

A modification of the electron g-factor g_e by the solid matrix can also cause line shifts [2, 94]. However, for H in H_2 this effect is expected to be negligible as there is no spin-orbit coupling for an electron associated with either a H atom or a H_2 molecule [94]. Experimental observations confirm this expectation [2, P8], on the contrary to noble gas matrices where the g-factor can be significantly changed [94]. Values of the g-factor for H in different systems are given in table 5.1.

5.5.3 Dipolar broadening and shift

In the system of H in H_2 one may expect both the dipolar broadening and shift of the resonance lines. The broadening can be caused by dipolar interactions with *ortho*-H_2 molecules and with other H atoms. Broadening due to dipolar interaction with o-H_2, which has been observed in several experiments [169, 145, P6, P8], depends on the o-H_2 concentration and may vary between 0.2 G and 1 G. In our experiments the influence of o-H_2 was observed as a narrowing of the ESR lines during the first days after creating of a new H_2 film. The maximum initial concentration of o-H_2 in the H_2 film might have been about 20% [P8], decreasing with time due to natural and stimulated *ortho-para* conversion processes [126, 161]. At H densities higher than $10^{18}\,\mathrm{cm}^{-3}$ we observed a density dependent broadening due to interactions between H atoms [P8], which at densities $> 10^{19}\,\mathrm{cm}^{-3}$ presented the main contribution to the line width.

In addition to broadening, we also observed shifts of the ESR lines due to the internal dipolar field. To account for the dipolar broadening and shifts of the H in H_2 lines we performed simulations for ESR line shape [P8]. For unlike atoms our results for the density dependent dipolar field and the broadening are respectively $-0.71 \times 10^{19} \times n\,\mathrm{G}\cdot\mathrm{cm}^3$ and $0.85 \times 10^{19} \times n\,\mathrm{G}\cdot\mathrm{cm}^3$. For like atoms these numbers should be multiplied by the factor 3/2 (sec. 2.3.3) [P8].

5.5.4 Influence of the H_2 matrix on the magnetic resonance spectrum: Summary

ESR:

The ESR line shifts from the free atom lines are given in eqs. (2.20) and (2.21). The change in the hyperfine constant ΔA_s shifts the $a-d$ and $b-c$ ESR lines in opposite directions while the dipolar field ΔB_{dip} has the same effect on both lines. From eqs. (2.20) and (2.21) follows that

$$\Delta A_s = g_e \mu_B \left(\Delta b_{bc} - \Delta b_{ad}\right), \tag{5.1}$$

$$\Delta B_{dip} = -\frac{\Delta b_{bc} + \Delta b_{ad}}{2}. \tag{5.2}$$

The ESR line shifts were measured as functions of the H density yielding the density dependence of ΔB_{dip}.

NMR:

The NMR frequency is mainly influenced by the change in the hyperfine constant. We evaluated the change in ΔA_s under the assumption that the nuclear g-factor is constant. The determination of both ΔA_s and the nuclear g-factor would require measurements on the both NMR transitions $a-b$ and $c-d$. Due to the large change $\Delta A_s \approx 1.5-3.5\,\mathrm{MHz}$, the value for ΔA_s is obtained from the exact equation (1.9).

5.6 Experiments

The first series of experiments (exp. I) was performed in 2005 and in early 2006, although preliminary studies had been done before in experiments which were focused on 2D H↓. In 2005 the quartz microbalance and the NMR resonator were installed to the SC. The highest H densities achieved in exp. I were $\lesssim 10^{18}\,\mathrm{cm}^{-3}$.

The second series of experiments (exp. II) began in late 2007 and were finished by the end of 2008. The densities up to about $3.5(5) \times 10^{19}\,\mathrm{cm}^{-3}$ were reached. Simulations of the dipolar interaction effects were performed after the experiments. An experimental run lasted typically 1-2 months. In the course of the experiments new methods were implemented for better creation and characterization of the samples. We tried two different methods for building thick H_2 film on the SC walls below 1 K. In one attempt we run discharge in the bottom helix resonator (fig. 5.1) partially embedded in solid H_2 on the SC bottom. In another attempt we blew a beam of ~ 5 K molecules into the sample cell. The beam was created by sublimating H_2 from a thermally insulated container attached to the SC bottom and filled with H_2 [P8]. Both methods were unsuccessful in creating thick H_2 layers on the FPR mirrors and the SC walls. Later we realized that a stronger axial field gradient was required to separate the lines originating from different mirrors. Such a capability was available only in the last experimental run, in which the maximum densities of H in H_2 were slightly smaller than in the previous experimental runs (sec. 5.6.2).

In exp. II atoms were produced in the solid H_2 films by running a discharge either in the bottom or NMR helical resonator [P7, P8]. An order of magnitude higher density of H in H_2 could be obtained using the NMR helix. This can be understood by the lower energy of bottom helix electrons which must experience at least one wall collision before reaching the FPR resonator. Also other differences were found between the bottom and NMR helix samples as discussed below.

5.6.1 ESR spectrum

Characteristic features of the ESR spectrum of H in H_2

Typical ESR spectra of H in the gas phase and in the solid H_2 matrix are presented in fig. 5.2. The ESR lines of the low density samples are shifted towards the center of the spectrum due to a decrease in hyperfine interaction. The ESR lines of high

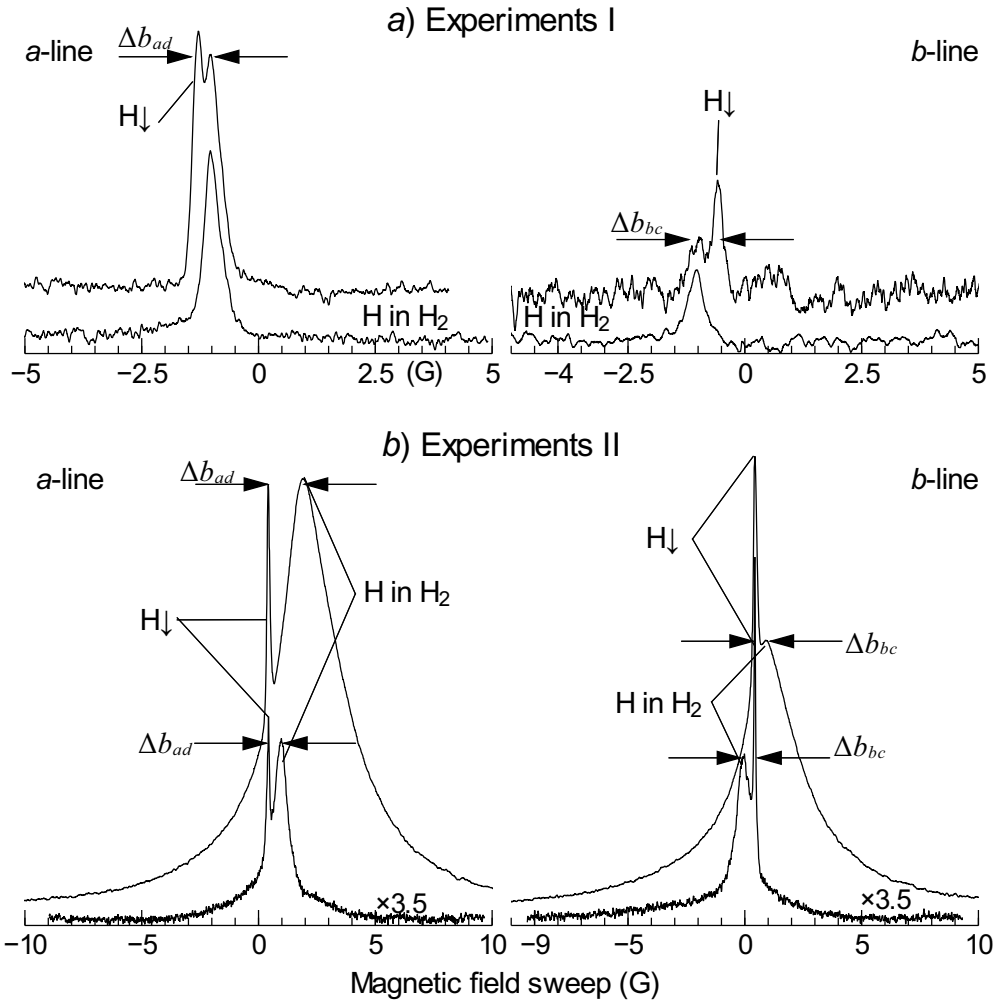

Figure 5.2: ESR spectra of atomic hydrogen in the gas phase and in the solid H_2 matrix in *a*) exp. I and *b*) exp. II, recorded with optimized field homogeneity. *a*) Low density ($n \sim 10^{17}\,\mathrm{cm}^{-3}$) sample with the ESR lines shifts corresponding to $\Delta b_{ad} = -\Delta b_{bc} = -\Delta A_s \,/\, 2g_e\mu_B \approx 0.25\,\mathrm{G}$. *b*) High and low density samples. The upper traces were recorded at $n \approx 2 \times 10^{19}\,\mathrm{cm}^{-3}$, the lower traces at $n \approx 6 \times 10^{17}\,\mathrm{cm}^{-3}$ and multiplied by factor 3.5. For the low density sample $\Delta b_{ad} = -\Delta b_{bc} = -\Delta A_s \,/\, 2g_e\mu_B \approx 0.5\,\mathrm{G}$. Δb_{ad} and Δb_{bc} indicate the shift of the H in H_2 line from the H↓ gas line respectively for the *a*- and *b*-lines.

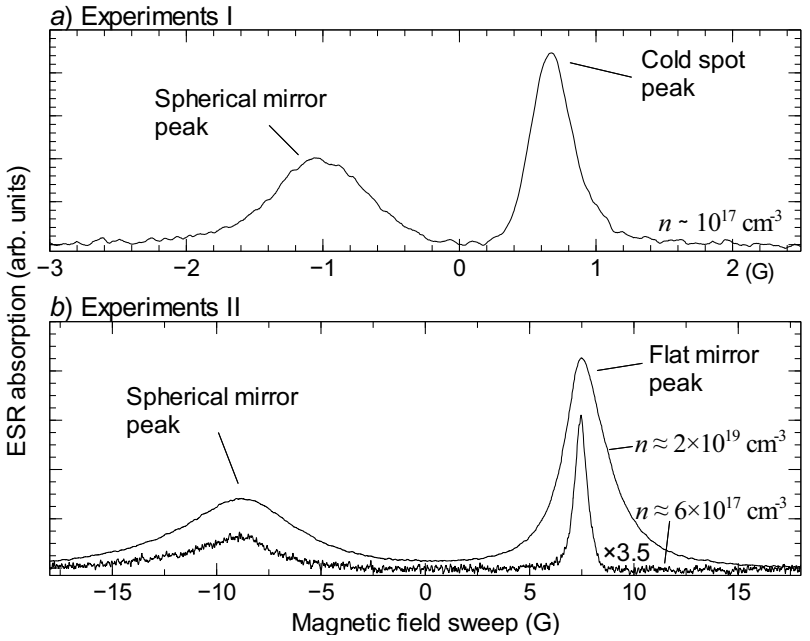

Figure 5.3: ESR $a-d$ transition spectra of H in H_2 in axial magnetic field gradient in the *a*) exp. I, gradient 5 G/cm, and in the *b*) exp. II, gradient 25 G/cm.

density samples are much broader and shifted from the H↓ lines to higher fields. For densities $\gtrsim 10^{18}\,\mathrm{cm}^{-3}$ the widths and positions of the H in H_2 lines depend on the H density. Density calibration of the ESR is presented in paper P8.

Fig. 5.3 shows the ESR lines of H in H_2 recorded in an axial magnetic field gradient which splits the lines into two peaks originating from different surfaces. In exp. I the samples were located on the cold spot (Mylar surface) and the spherical mirror (Cu surface coated with Stycast 1266). The ESR lines were inhomogeneously broadened for the samples on both surfaces. In exp. II the samples were on the spherical mirror (pure Cu surface) and on the flat mirror (Mylar surface). The ESR line widths of the spherical mirror samples were found to be ≈ 6 G and nearly independent of the H density. In contrast, the widths of the flat mirror sample lines were found to be proportional to the density (fig. 5.5). Also, now the flat mirror line was homogeneously broadened while the spherical mirror line was inhomogeneously broadened. We attributed these differences to the different properties of the substrates. The spherical mirror surface is polycrystalline copper and has larger roughnesses than the flat mirror [P8]. Below, we mainly consider the properties of flat mirror samples because they depend less on the substrate properties.

Shifts of the ESR lines of H in H_2

The ESR line shifts Δb_{ad} and Δb_{bc} (fig. 5.2) were analyzed with the help of eqs. (5.1) and (5.2) (sec. 5.5.4). In exp. I we found $\Delta A_s = -1.5\,\mathrm{MHz}$ while the g-factor was not affected (dipolar shift was negligible). In exp. II we found that ΔA_s is different for the samples created by the bottom and NMR helices. For the low density sample created by the bottom helix $\Delta A_s = -1.7(5)\,\mathrm{MHz}$ whereas for the high density NMR helix sample $\Delta A_s = -3.5(6)\,\mathrm{MHz}$. More accurate measurements of the ΔA_h are performed using ENDOR.

The extracted dipolar shift $-\Delta B_{dip}$ in exp. II as a function of H concentration is presented in fig. 5.4 together with the simulated results (sec. 5.5.3) [P8].

5.6.2 Dipolar interaction effects and highest densities in second experiments

In the second experiments we observed both the dipolar broadening and shifts of the ESR lines. Width of the H in H_2 line for optimized field homogeneity (fig. 5.2) and the flat mirror line width in an axial gradient (fig. 5.3) are presented in fig. 5.5. Both widths as well as the dipolar shift are proportional to the density. The dipolar broadening and shift are discussed in P8.

More data in the field of optimized homogeneity was collected in several runs, in which we could not separate the flat and spherical mirror lines. However, because the density dependences of the ESR line shift and broadening were constant for the studied film thicknesses [P8], the shift and broadening can be compared also between different experimental runs. Accordingly a shift vs. width plot must be linear and both quantities can be used for a density measurement.

Because of the unequal nuclear polarizations in the flat and spherical mirror samples (sec. 5.6.5), we restrict the line width study to the $a - d$ line at typical steady-state nuclear polarizations $P \approx 0$ and $P \approx 1/3$ for the spherical and flat mirror samples, respectively.

Fig. 5.6 shows a summary of the width and shift data for several experimental runs. The data for different experimental runs fall to a straight line. Density calibration for the width in the field of optimized homogeneity is obtained from fig. 5.5. The shift is converted to density by using the constant obtained from the simulations (sec. 5.5.3) [P8]. According to this data the highest densities obtained were $3.5(5) \times 10^{19}\,\mathrm{cm}^{-3}$.

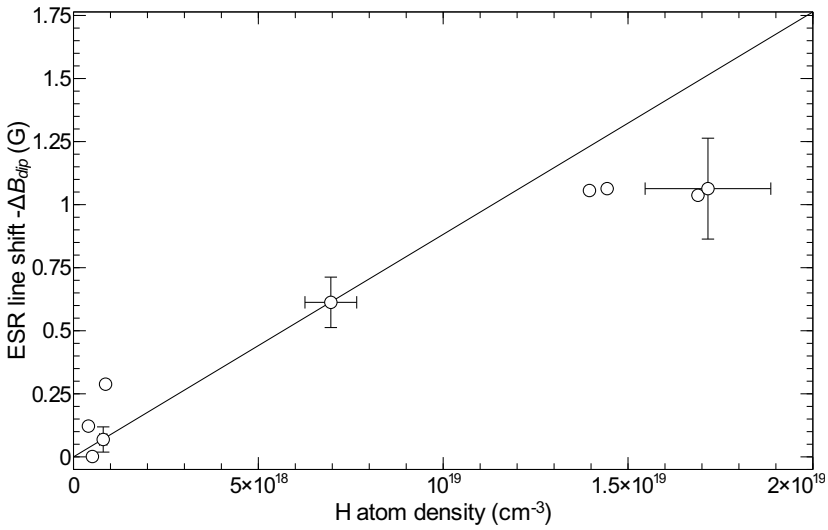

Figure 5.4: Density-dependent shift of the ESR lines in exp. II. The solid line is the result of simulation (sec. 5.5.3) [P8].

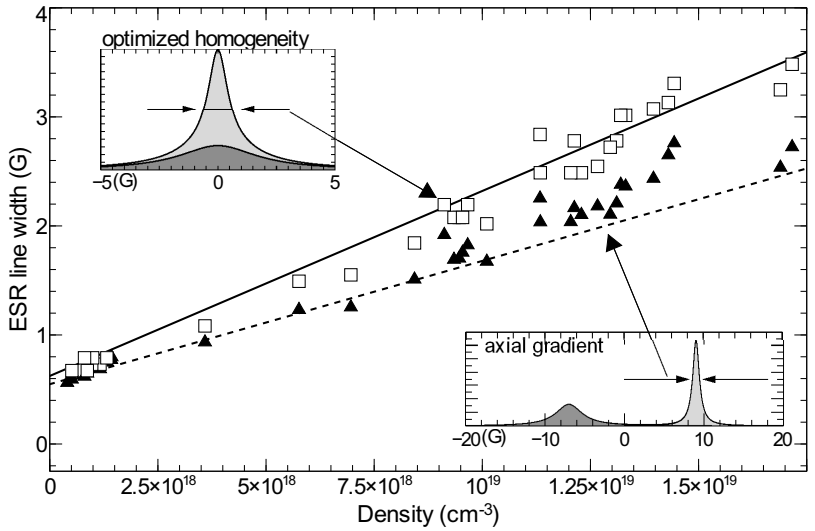

Figure 5.5: H in H_2 ESR line width in exp. II. □ = ESR a-line FWHM in field of optimized homogeneity. ▲ = Flat mirror a-line FWHM in axial gradient. The insets illustrate how the line is composed of the flat and spherical mirror components. The differently highlighted areas represent contributions of each mirror. The dashed line indicates broadening of the flat mirror line obtained from simulations (sec. 5.5.3) [P8]. The solid line is a fit to the □ data, later used for density calibration in fig. 5.6.

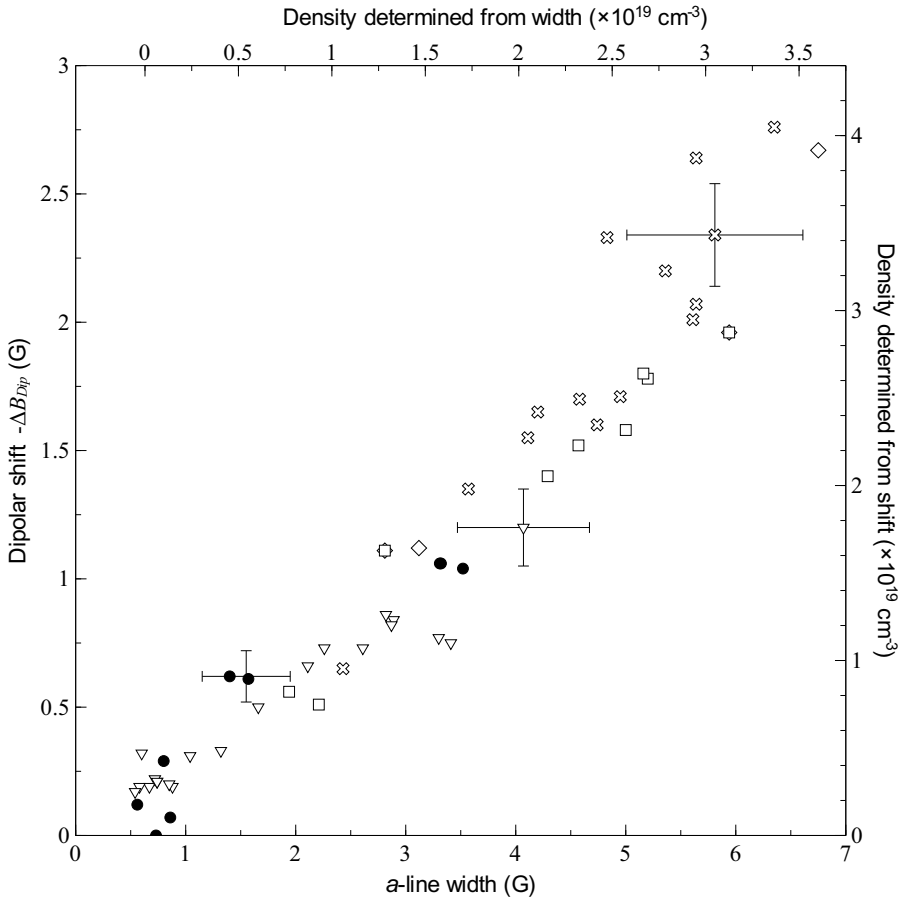

Figure 5.6: The ESR line width in field of optimized homogeneity plotted against the ESR line shift in several experimental runs in exp. II. The two density axes represent the density extracted from the ESR line shift (fig. 5.4) and the ESR line width (fig. 5.5).

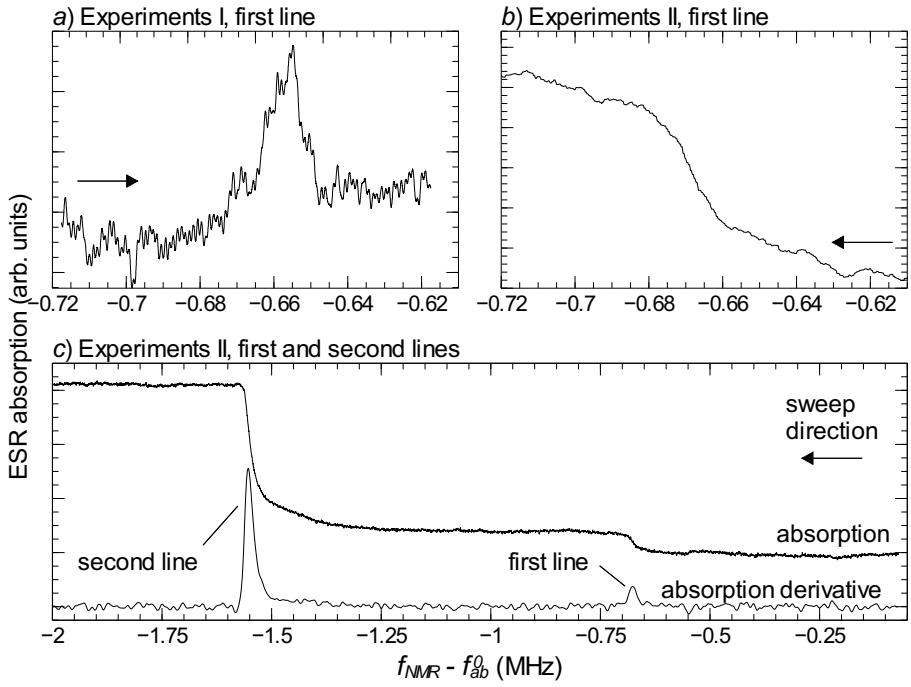

Figure 5.7: ENDOR spectra for H in H_2. *a*) In exp. I a single ENDOR line shifted by $\Delta f_{NMR} \approx -0.66\,\mathrm{MHz}$ was found, referred to as the first line. *b*) The first line in exp. II. *c*) In exp. II another ENDOR line was found at $\Delta f_{NMR} \approx -1.5\,\mathrm{MHz}$, referred to as the second line. The passage condition of *a*) is different from *b*) and *c*).

5.6.3 ENDOR spectra and hyperfine interaction changes

ENDOR spectra were recorded in the both series of experiments. In exp. II we were able to detect ENDOR from the flat mirror (Mylar substrate) sample only. Typical ENDOR spectra are presented in fig. 5.7.

The passage condition were different in exp. I and exp. II. In both cases, preceding the NMR frequency sweep the entire population of the *b*-state was driven into the *a*-state via the forbidden $a - c$ transition (sec. 1.6.5). The rate of the population transfer could be controlled by the ESR excitation power but was limited by the $a - c$ relaxation rate.

In exp. I the $a - c$ relaxation was fast enough compared to the $a - b$ transition rate. The a and b populations recovered to the steady-state quickly after inducing the NMR transition (sec. 1.6.4, condition 1). Thus the ENDOR spectrum reproduced the actual shape of the $a - b$ NMR transition (fig. 5.7*a*). In exp. II the $a - c$ relaxation was much slower and recording the true ENDOR spectrum would have required an extremely long time. Therefore, we utilized a rapid passage technique

where ENDOR spectra were recorded at a low ESR power when the $b \to c \to a$ transfer rate was negligible. When the NMR transition is excited, the b-state population increases and hence the $b-c$ ESR transition absorption increases (fig. 5.7*c*). The signal recorded as a function of the rf frequency represents the total number of atoms transferred from a to b since the beginning of the sweep. The actual ENDOR spectrum, *i.e.* the transition rate as a function of frequency, is obtained by taking the derivative of the recorded spectrum (fig. 5.7*c*).

In exp. I we observed a single transition shifted by about -660 kHz from the free atom frequency f_{ab}^0 (fig. 5.7*a*). In exp. II we observed also a second line shifted by $\approx -1.56\,\mathrm{MHz}$ (table 5.1). The first line was more intense for the low density samples created by the bottom helix whereas the second line was characteristic of the high density samples created by the NMR helix (fig. 5.7*c*).

5.6.4 Recombination

Recombination of H atoms in H_2 crystals is a two-body process, described by the second order rate equation

$$\frac{dn}{dt} = -2K_r n^2, \tag{5.3}$$

where K_r is the recombination rate constant and $n = n_a + n_b$ is the total H atom density. Consequently, the inverse density n^{-1} has a linear dependence on time with the slope $2K_r$. Electronic polarization of the atoms was found to have no effect on the recombination rate [143, P6]. In the present experiments [P8] even nuclear polarization had no effect on the recombination rates [143]. In all measurements the inverse density was found to be linear in time, in agreement with eq. (5.3).

A summary of the recombination rates obtained in exp. I and exp. II is presented in fig. 5.8. Generally, the recombination rates were found to be somewhat faster in exp. I than in exp. II. The recombination rate of the spherical mirror (Cu substrate) sample accumulated by the NMR helix coincided with that of the flat mirror (Mylar substrate) sample. However, a difference was found between the flat mirror samples created by the bottom and NMR helices. Already at 0.5 K recombination of the bottom helix sample was much faster than recombination rate of the NMR helix sample. This can be possibly explained by a larger number of defects and higher localization of impurity atoms in the samples created by the NMR helix.

An other interesting observation was the enhancement of recombination of H in H_2 during H_2 coating. It can be explained by a strong flux of phonons resulting from the H$\downarrow$ recombination propagating into the solid matrix. This process could also have been responsible for reaching only relatively low H densities in exp. I.

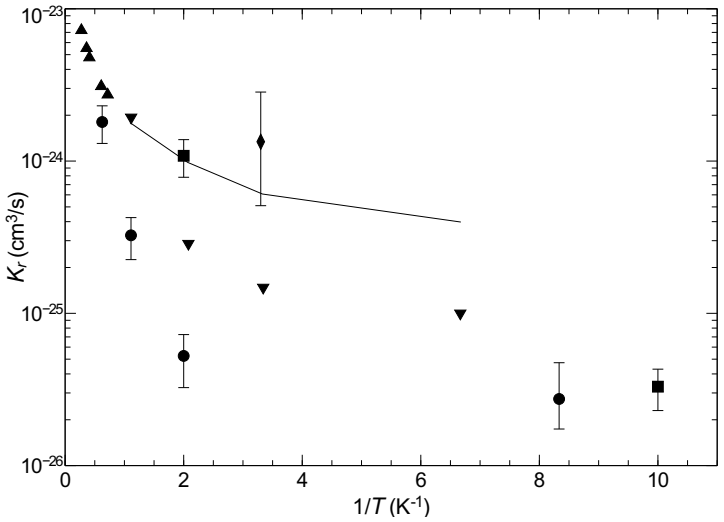

Figure 5.8: Recombination rate constants for H in H_2 from different experiments [P7]. ▼ = Exp. I [P6]. Exp. II, flat mirror samples [P7, P8]: ■ = low density bottom helix sample, • = high density NMR helix sample, ♦ = high density NMR helix sample under H_2 coating. ▲ = Flash condensed samples by Ivliev *et al.* [170] $T > 1\,\mathrm{K}$. Solid line shows theoretical result of Kagan *et al.* for $T \leq 1\,\mathrm{K}$ [22].

5.6.5 Nuclear relaxation

For a non-degenerate atomic system the populations of the hyperfine states a and b in thermal equilibrium are related via the Boltzmann factor $n_a/n_b = \exp(E_{ab}/k_B T)$, where $E_{ab} = 48$ mK is the energy difference between the two states in a magnetic field of 4.6 T. In exp. I we observed significant deviations from this law at the temperature of 150 mK [P6]. In exp. II we performed detailed studies of the steady-state nuclear polarization $P = (n_a - n_b)\,/\,(n_a + n_b)$ as a function of temperature.

The experiments were done by driving the system out of thermal equilibrium and then following its relaxation. Non-thermal hyperfine level populations were created by saturating the $a-b$ transition by the NMR ($P \to 0$, sec. 1.6.2) leading to an excess of b atoms with respect to the Boltzmann factor or saturating the $b-c$ transition with subsequent transfer of b-state atoms into the a-state via the "forbidden" $a-c$ transition ($n_a \gg n_b$, $P \to 1$, sec. 1.6.5).

A summary of the results of exp. I and exp. II are presented in fig. 5.9. The deviation from thermal equilibrium was largest in exp. I, and for flat mirror samples in exp. II. For the NMR helix sample in exp. II the deviation was found to be smaller. The spherical mirror samples in exp. II were observed to relax to the Boltzmann distribution.

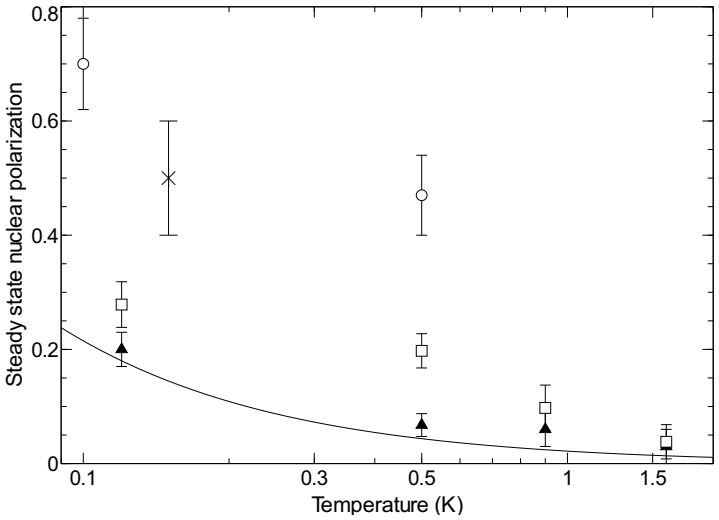

Figure 5.9: Steady-state nuclear polarizations in exp. I (×) and exp. II [P8]. Exp. II: ◯ = low density flat mirror sample created by bottom helix (Mylar substrate), □ = high density flat mirror sample sample created by NMR helix (Mylar), ▲ = spherical mirror sample created by NMR helix (copper substrate). The solid line corresponds to the Boltzmann distribution.

5.7 Future prospects for reaching higher H densities

5.7.1 Current method and possible improvement

Our experiments provided information which allows to suggest an improved sample preparation method and to estimate the feasibility of reaching higher densities of H in H_2. The sample preparation methods realized in exp. I [P6] and exp. II [P8] have disadvantages regarding the sample quality and highest densities. In both experiments the H_2 film was formed by recombination from the H↓ gas. Such films are rather thin and there was no possibility of a direct study of the crystal quality. H_2 films built by recombination of H↓ also contain high concentrations of *ortho*-H_2, up to 20% in freshly prepared samples. These problems could be avoided by condensing the H_2 from vapor during precooling and accumulating H in H_2 by dissociating H_2 molecules *in situ* in the solid. Preliminary experiments utilizing such a technique have been carried out by Järvinen *et al.* at Cornell University [171]. However, dissociation of the H_2 molecules *in situ* in the solid, *e.g.* via electron bombardment or via irradiation, is not an optimum solution due to the extra defects created in the lattice. Moreover, when considering highest achievable H densities in H_2, a large heat is released to the H_2 film in the bombardment and irradiation processes catalyzing fast hopping and recombination of H in H_2. As to the excess heat the recombination method is even worse (sec. 5.7.2).

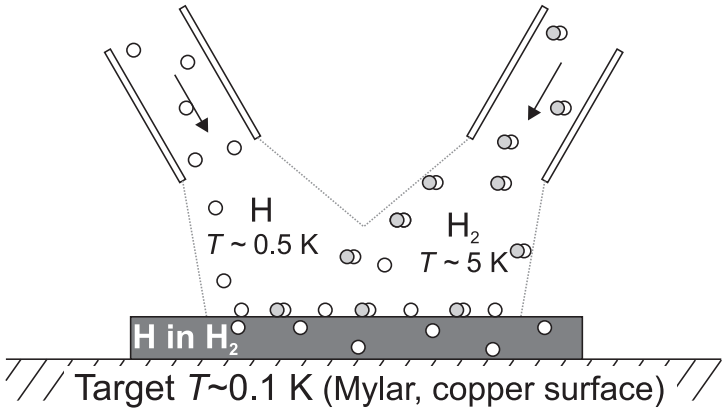

Figure 5.10: Illustrating the cold atom and molecule epitaxy.

As a solution to the above mentioned problems we propose to create the samples by cold atomic and molecular beam epitaxy. The main difference compared to the other methods is that the H in H_2 sample is built from cold ground state atoms and molecules. This would allow to avoid heat generated in the SC due to relaxation of rovibrationally excited H_2 molecules. We recall that the recombination heat in the H_2 coating process catalyzes recombination of H in H_2 (sec. 5.6.4) [P8]. The extra heat, at least 3.2 eV per atom released in dissociation of H_2 molecules by the electron impact [139, 155], must catalyze a similar effect. The epitaxy method would also enable diffusion studies if we deposit a layer of H in H_2 between pure H_2 layers.

In principle, the beam epitaxy method is similar to that used by Jen *et al.* [2] and by Lukashevich and coworkers [143, 161], but we propose to implement it at lower temperatures and to use pure H and H_2 beams. In previous experiments the beams had a high temperature and the heat released in the process limited the temperature of the target. We believe that the quality of the solid would be better in our case due to the slow speed of the sample growth. Beams of cold $< 0.5\,\mathrm{K}$ H atoms are readily available in experiments with H↓ [12] and H_2 molecules of a few K can be obtained by sublimation from the solid phase. However, a problem is how to transfer the beams to the cold ($< 0.5\,\mathrm{K}$) target. Production and transfer of H requires helium coating of the walls but the target for H in H_2 sample must be free of helium. This will require a careful design of the sample cell and techniques to cut the superfluid helium film. The samples will be very pure because only few elements can penetrate to the sample cell at 1 K temperatures and the o-H_2 concentration can be controlled. However, the low temperatures also limit the method to H because D cannot be handled easily below 1 K.

5.7.2 Estimates of the feasibility of reaching higher H densities in H_2

Here we assume that excessive heat limits the highest densities for each method. Extra heat in the form of lattice phonons stimulates faster diffusion (hopping) of atoms in the crystal and catalyzes recombination.

We separate the sample preparation heat into two parts, one is due to the deposition of H_2 molecule (Q_{H_2}) and the other of H atom (Q_H). The heat released in forming an H in H_2 sample of volume V is then given by

$$Q = V n_{H_2} \left(Q_{H_2} (1 - x) + Q_H x \right), \tag{5.4}$$

where x is the relative concentration of H atoms and n_{H_2} is the density of H_2 crystal, for hcp structure $n_{H_2} \approx 2.6 \times 10^{22}\,\mathrm{cm}^{-3}$ [23]. The H atoms are assumed to occupy substitutional sites in the lattice.

In the following we analyze the amount of heat generated by different methods and a summary is given in table 5.2. We demonstrate a significant decrease of the heat released in sample preparation using the method of cold atomic and molecular beam epitaxy. According to our estimates, densities as high as or even higher than with electron impact dissociation can be achieved with epitaxy method. However, optimization of the method for reaching the highest densities may require careful control of the experimental parameters.

Recombination method In this method the H_2 film with H atoms is formed by recombination in H↓. Large heat is released in the process, $Q_{H_2} = 52000\,\mathrm{K}$ per H_2 molecule. Capturing of H atoms is enabled by the recombination process, so no extra heat is needed. The heat released in the deposition of H atom or H_2 molecule on solid H_2 is negligible compared to the recombination heat. When $x \ll 1$ in eq. 5.4, $Q \approx V n_{H_2} Q_{H_2}$.

Disadvantages of this method are the impossibility to control the density of H in H_2 and generally low densities $n \lesssim 10^{18}\,\mathrm{cm}^{-3}$ ($x \lesssim 5 \times 10^{-5}$) limited by the heat release in the process. Also the rate of the H in H_2 film growth is very slow, a couple of H_2 monolayers per hour. Once the sample is destroyed, a new sample must be built by repeating the whole lengthy procedure.

Electron impact dissociation of H_2 In this method the H_2 matrix is formed in advance, implying $Q_{H_2} = 0$. However, the dissociation process is quite ineffective as electrons excite and ionize H_2 molecules besides dissociating them [172]. In addition, each atom resulting from a dissociation event carries at least 3.2 eV (37000 K) extra energy [139, 155]. Leach studied the accumulation of H in H_2 at 4 K with 160 keV electrons [140]. He measured that on the average 0.2 atoms were formed by 100 eV of ionizing radiation. Souers presents data for electron energy loss processes ionization, dissociation and excitation in H_2 vapor [172]. The efficiency of producing atoms is found to be highest for low energy electrons.

Table 5.2: Heat release in different accumulation methods. In the two last columns the quantity $Q\,/\,Vn_{\mathrm{H_2}}$ (eq. 5.4) is evaluated for densities [1] $n_{\mathrm{H}} = 10^{19}\,\mathrm{cm}^{-3}$ and [2] $n_{\mathrm{H}} = 4\times10^{19}\,\mathrm{cm}^{-3}$ to compare the methods.

Method	$Q_{\mathrm{H_2}}$ (K)	Q_{H} (K)	Q/Vn (K)[1]	Q/Vn (K)[2]
Recombination growth	52000	0	52000	52000
Molecular/atom beam epitaxy	100	100	100	100
Electron impact dissociation				
Theoretical minimum [139, 155]	0	3.7×10^4	14	57
16.2−130 eV electrons [172]	0	$7.7\times10^4 - 3\times10^5$	$30-120$	$120-460$
160 keV electrons [140]	0	3×10^6	1.2×10^3	4.6×10^3

In the case of the low temperature rf discharge used in our work, the characteristic energy of electrons $\sim 100\,\mathrm{eV}$ favors highest possible densities. However, low-energy electrons cannot penetrate deep into the H_2 film, which may limit our method to thin H_2 films [171].

Drawbacks are that the electron impact dissociation produces defects to the H_2 crystal and too much heat is liberated in the dissociation process.

Epitaxy The heat released in molecular epitaxy is solely composed of the condensing heat and the kinetic energy of atoms and molecules. The condensation heat for single H_2 molecule is 90 K (sublimation heat in the zero temperature limit [23]), and of the same order for H atoms [173]. The average thermal energies are $< 1\,\mathrm{K}$ and $< 10\,\mathrm{K}$ for H and H_2, respectively. We obtain $Q_{\mathrm{H_2}} \approx Q_{\mathrm{H}} \approx 100\,\mathrm{K}$ and altogether $Q \approx Vn_{\mathrm{H_2}} \times 100\,\mathrm{K}$.

The condensing heat (100 K / H or H_2) is small but not negligible. However, similar amount of heat 165 K per o-H_2 molecule is released in the *ortho-para* conversion in the current samples [23]. Thus it appears that the condensing heat will not catalyze recombination at least at the densities $n{\sim}10^{19}\,\mathrm{cm}^{-3}$ of current experiments. In future experiments preparation of pure p-H_2 solids will allow one to avoid the conversion heat.

However, in epitaxy the fluxes of H and H_2 to the target will be needed to be carefully regulated. In the method of electron impact dissociation the average heating power per unit area was $\approx 0.25\,\mu\mathrm{W/cm}^2$ ($40\,\mu\mathrm{W}$ power released in the whole SC) [P8]. Taking this as an upper limit for the heat which can be released during accumulation, we estimate that with epitaxy a monolayer ($\approx 8.8\times10^{14}\,\mathrm{molecules/cm}^2$) can be formed within a few seconds.

5.8 Discussion

Our experiments demonstrated the feasibility of studies of H in H_2 in the 100 mK temperature range. The samples showed higher stability than those in earlier experiments which were performed above 1 K. We reached the record high density of $3.5(5) \times 10^{19}$ cm^{-3} (0.2%) of H in H_2 below 0.5 K using the method of electron impact dissociation of H_2 *in situ* in the solid (exp. II). Alternatively, H atoms were captured in the H_2 film due to three-body recombination of gas phase atoms (exp. I) but then the highest densities were limited to 10^{18} cm^{-3}. However, both methods suffer from some disadvantages which can be overcome with an improved sample preparation method. The quality of present thin H_2 film samples grown by recombination of gas phase H$\downarrow$ has not been studied directly and the *ortho*-H_2 concentration ($< 20\%$) cannot be controlled. In an improved experiment we suggest to implement the method of cold molecular and atomic beam epitaxy to grow H in H_2 films. In addition to the better quality of the samples, also the heat release is substantially smaller than for the present methods and this is expected to lead to further increase in the density of H in H_2.

The magnetic resonance methods serve as powerful tools for the characterization of samples. In exp. II we observed dipolar broadening and shifts of the ESR lines at densities $> 10^{18}$ cm^{-3}. Numerical simulations of the line shape and shift coincide well with the experimental observations and further substantiate our density measurement. ENDOR measurements revealed two sharp transitions shifted to the red from the free atom transition, implying that there exist two kinds of atoms in our samples. The first transition, due to the first kind of atoms, corresponding to a $\Delta A_h \approx -1.3$ MHz change in the hyperfine constant, was observed mainly in the exp. I and in low density ($n_H \lesssim 3 \times 10^{18}$ cm^{-3}) samples of exp. II. The second much stronger transition at $\Delta A_h \approx -3.1$ MHz was characteristic of samples with higher H atom densities in exp. II. The accumulation of the low density samples is characterized by lower energy of the electrons compared to high density sample accumulation. The two ENDOR transitions point to two possible H atom occupation sites in the H_2 lattice. The negative sign of the transition shift implies that the atoms are located in substitutional positions. However, in a hcp lattice the environment of every substitutional site is equivalent. One explanation is stronger coupling of the second kind of atoms to vacancies or dislocations. We expect a large amount of defects created in the electron impact dissociation of H_2 molecules in the solid. However, this is in contradiction with the small widths of the observed ENDOR transitions implying a homogeneous crystalline field experienced by the atoms. Some measurements for the hyperfine constant exist [2, 139] but it seems difficult to compare those with our results. Temperatures, sample preparation methods and the *ortho*-H_2 concentrations were quite different.

By studying recombination of H in H_2 we found faster recombination of the first kind of atoms, indicating their higher mobility. This observation supports the ENDOR measurement, implying that the second kind of atoms are more strongly

coupled to the lattice than atoms of the first kind.

The most intriguing observation in both experiments is the significant deviation of the steady-state nuclear polarization from the value determined by the Boltzmann distribution. This behavior has been also observed in thick H_2 films condensed from the vapor phase [171]. In exp. II we found that the deviation is larger for the first kind of atoms than for the second kind of atoms. The experiments revealed a weak temperature dependence of the steady-state nuclear polarization. The deviation from Boltzmann behavior seems to grow gradually when the temperature is lowered. Since the population of the lower energy (ground) state is enhanced, we suggested that this phenomenon can be related to Bose-Einstein condensation (BEC) of the impurity atoms. However, the average densities obtained so far are not high enough to reach BEC at the temperatures of the experiment, even assuming that the effective mass of the impurity atoms is close to the H bare mass. Different candidate theories are considered in ref. [133].

Bibliography

[1] C. K. Jen, S. N. Foner, E. L. Cochran, and V. A. Bowers, Phys. Rev. **104**, 846 (1956).

[2] C. K. Jen, S. N. Foner, E. L. Cochran, and V. A. Bowers, Phys. Rev. **112**, 1169 (1958).

[3] Daniel W. Brown, Roland E. Florin, and Leo A. Wall, J. Phys. Chem. **66**, 2602 (1962).

[4] A. P. Bass and H. P. Broida, *Formation and Trapping of Free Radicals* (Academic Press, New York and London, 1960).

[5] Charles E. Hecht, Physica **25**, 1159 (1959).

[6] Isaac F. Silvera and J. T. M. Walraven, Phys. Rev. Lett. **44**, 164 (1980).

[7] M. H. Anderson, J. R. Ensher, M. R. Matthews, C. E. Wieman, and E. A. Cornell, Science **269**, 198 (1995).

[8] K. B. Davis, M. O. Mewes, M. R. Andrews, N. J. van Druten, D. S. Durfee, D. M. Kurn, and W. Ketterle, Phys. Rev. Lett. **75**, 3969 (1995).

[9] Dale G. Fried, Thomas C. Killian, Lorenz Willmann, David Landhuis, Stephen C. Moss, Daniel Kleppner, and Thomas J. Greytak, Phys. Rev. Lett. **81**, 3811 (1998).

[10] A. I. Safonov, S. A. Vasilyev, I. S. Yasnikov, I. I. Lukashevich, and S. Jaakkola, Phys. Rev. Lett. **81**, 4545 (1998).

[11] A. Fukuda, H. Takenaka, T. Ohmi, and T. Mizusaki, J. Low Temp. Phys. **126**, 127 (2002).

[12] J. Järvinen, J. Ahokas, and S. Vasiliev, J. Low Temp. Phys. **147**, 579 (2007).

[13] Kurt Gibble and Steven Chu, Phys. Rev. Lett. **70**, 1771 (1993).

[14] B. V. Svistunov and N. V. Prokof'ev, private communication.

[15] I. F. Silvera and J. T. M. Walraven, *Spin-polarized atomic hydrogen*, in *Prog. in Low Temp. Phys.*, edited by D. F. Brewer (North-Holland, Amsterdam, 1986), vol. X, p. 139.

[16] I. F. Silvera, Phys. Rev. B **29**, 3899 (1984).

[17] K. E. Kürten and M. L. Ristig, Phys. Rev. B **31**, 1346 (1985).

[18] S. Vasilyev, J. Järvinen, V. V. Khmelenko, and D. M. Lee, AIP Conf. Proc. **850**, 81 (2006).

[19] A. F. Andreev and I. M. Lifshitz, Sov. Phys. JETP **29**, 1107 (1969).

[20] A. Sen, S. Chakraborty, and A. S. Ghosh, Europhys. Lett. **76**, 582 (2006).

[21] M. J. Jamieson, A. S. C. Cheung, and H. Ouerdane, Eur. Phys. J. D **56**, 181 (2010).

[22] Yu. Kagan and L. A. Maksimov, Sov. Phys JETP **57**, 459 (1983).

[23] Isaac F. Silvera, Rev. Mod. Phys. **52**, 393 (1980).

[24] J. T. M. Walraven, *Atomic hydrogen and liquid helium surfaces*, in *Fundamental systems in quantum optics*, edited by J. Dalibard, J. M. Raimond, and J. Zinn-Justin (Elsevier Science Publishers, Amsterdam, 1992), vol. 1, p. 487.

[25] A. I. Safonov, S. A. Vasiliev, A. A. Kharitonov, S. T. Boldarev, I. I. Lukashevich, and S. Jaakkola, Phys. Rev. Lett. **86**, 3356 (2001).

[26] J. Järvinen, J. Ahokas, S. Jaakkola, and S. Vasilyev, Phys. Rev. A **72**, 052713 (2005).

[27] Yu. Kagan, G. V. Shlyapnikov, I. A. Vartan'yants, and N. A. Glukhov, JETP Lett. **35**, 447 (1982).

[28] D. S. Petrov, D. M. Gangardt, and G. V. Shlyapnikov, J. Physique IV **116**, 14 (2004).

[29] L. Philip H. de Goey, Henk T. C. Stoof, J. M. Vianney A. Koelman, Boudewijn J. Verhaar, and Jook T. M. Walraven, Phys. Rev. B **38**, 11500 (1988).

[30] B. V. Svistunov, T. W. Hijmans, G. V. Shlyapnikov, and J. T. M. Walraven, Phys. Rev. B **43**, 13412 (1991).

[31] A. Matsubara, T. Arai, S. Hotta, J. S. Korhonen, T. Suzuki, A. Masaike, J.T.M. Walraven, T. Mizusaki, and A. Hirai, Physica B **194-196**, 899 (1994).

[32] T. Tommila, E. Tjukanov, M. Krusius, and S. Jaakkola, Phys. Rev. B **36**, 6837 (1987).

[33] B. W. Statt, A. J. Berlinsky, and W. N. Hardy, Phys. Rev. B **31**, 3169 (1985).

[34] A. Abragam, *Principles of Nuclear Magnetism* (Oxford University Press, 1961).

[35] G. Breit and I. I. Rabi, Phys. Rev. **38**, 2082 (1931).

[36] B. W. Statt, W. N. Hardy, A. J. Berlinsky, and E. Klein, J. Low Temp. Phys. **61**, 471 (1985).

[37] S. A. Vasilyev, A. Ya. Katunin, A. I. Safonov, A. V. Frolov, and E. Tjukanov, Appl. Magn. Reson. **3**, 1061 (1992).

[38] B. Yurke, J. S. Denker, B. R. Johnson, N. Bigelow, L. P. Lévy, D. M. Lee, and J. H. Freed, Phys. Rev. Lett. **50**, 1137 (1983).

[39] M. Mertig, E. Tjukanov, S. A. Vasilyev, A. Ya. Katunin, and S. Jaakkola, J. Low Temp. Phys. **100**, 45 (1995).

[40] S. Vasilyev, J. Järvinen, E. Tjukanoff, A. Kharitonov, and S. Jaakkola, Rev. Sci. Instr. **75**, 94 (2004).

[41] L. Kevan and L. D. Kispert, *Electron Spin Double Resonance Spectroscopy* (John Wiley and Sons, 1976).

[42] S. A. Vasilyev, A. Ya. Katunin, E. Tjukanov, and I. I. Lukashevich, JETP Lett. **48**, 140 (1988).

[43] A. Ya. Katunin, I. I. Lukashevich, S. T. Orosmamatov, V. V. Sklyarevskii, V. V. Suraev, V. V. Filippov, N. I. Filippov, and V. A. Shevtsov, Phys. Lett. A **87**, 483 (1982).

[44] M. O. Scully and M. S. Zubairy, *Quantum Optics* (Cambridge University Press, Cambridge, 1997).

[45] J. Helffrich, M. Maley, M. Krusius, and J. C. Wheatley, J. Low Temp. Phys. **66**, 277 (1987).

[46] R. van Roijen, J. J. Berkhout, B. Hebral, and J. T. M. Walraven, A cryogenic dissociator for atomic hydrogen. University of Amsterdam, unpublished (1989).

[47] I. Shinkoda and W. N. Hardy, J. Low Temp. Phys. **85**, 99 (1991).

[48] T. Peltonen, E. Tjukanoff, J. Järvinen, and S. A. Vasilyev, Proc. ESA WPP-212 p. 447 (2003).

[49] J. C. Collingwood and J. W. White, J. Sci. Instrum. **44**, 509 (1967).

[50] L. Bruschi, G. Delfitto, and G. Mitsura, Rev. Sci. Instr. **70**, 153 (1999).

[51] T. Lahaye, C. Menotti, L. Santos, M. Lewenstein, and T. Pfau, Rep. Prog. Phys. **72**, 126401 (2009).

[52] Sumana Chakraborty, A. Sen, and A. S. Ghosh, Eur. Phys. J. D **45**, 261 (2007).

[53] Leslie E. Ballentine, *Quantum Mechanics: A Modern Development* (World Scientific, 1998).

[54] J. Vanier and C. Audoin, *Quantum Physics of Atomic Frequency Standards* (Adam Hilger, Bristol, 1989).

[55] M. Morrow, R. Jochemsen, A. J. Berlinsky, and W. N. Hardy, Phys. Rev. Lett. **46**, 195 (1981).

[56] R. Jochemsen, M. Morrow, A. J. Berlinsky, and W. N. Hardy, Phys. Rev. Lett. **47**, 852 (1981).

[57] Harald F. Hess, Greg P. Kochanski, John M. Doyle, Thomas J. Greytak, and Daniel Kleppner, Phys. Rev. A **34**, 1602 (1986).

[58] M. D. Hürlimann, W. N. Hardy, A. J. Berlinsky, and R. W. Cline, Phys. Rev. A **34**, 1605 (1986).

[59] Ronald L. Walsworth, Isaac F. Silvera, H. P. Godfried, C. C. Agosta, Robert F. C. Vessot, and Edward M. Mattison, Phys. Rev. A **34**, 2550 (1986).

[60] B. J. Verhaar, J. M. V. A. Koelman, H. T. C. Stoof, O. J. Luiten, and S. B. Crampton, Phys. Rev. A **35**, 3825 (1987).

[61] J. M. V. A. Koelman, S. B. Crampton, H. T. C. Stoof, O. J. Luiten, and B. J. Verhaar, Phys. Rev. A **38**, 3535 (1988).

[62] M. E. Hayden, M. D. Hürlimann, and W. N. Hardy, Phys. Rev. A **53**, 1589 (1996).

[63] S. J. J. M. F. Kokkelmans and B. J. Verhaar, Phys. Rev. A **56**, 4038 (1997).

[64] M. A Lombardi, T. P Heavner, and S. R Jefferts, The Journal of Measurement Science Vol **2** (2007).

[65] E. G. M. van Kempen, S. J. J. M. F. Kokkelmans, D. J. Heinzen, and B. J. Verhaar, Phys. Rev. Lett. **88**, 093201 (2002).

[66] B. Zygelman, A. Dalgarno, M. J. Jamieson, and P. C. Stancil, Phys. Rev. A **67**, 042715 (2003).

[67] C. J. Pethick and H. T. C. Stoof, Phys. Rev. A **64**, 013618 (2001).

[68] M. Ö. Oktel, T. C. Killian, D. Kleppner, and L. S. Levitov, Phys. Rev. A **65**, 033617 (2002).

[69] D. M. Harber, H. J. Lewandowski, J. M. McGuirk, and E. A. Cornell, Phys. Rev. A **66**, 053616 (2002).

[70] G. K. Campbell, M. M. Boyd, J. W. Thomsen, M. J. Martin, S. Blatt, M. D. Swallows, T. L. Nicholson, T. Fortier, C. W. Oates, S. A. Diddams, N. D. Lemke, P. Naidon, P. Julienne, Jun Ye, and A. D. Ludlow, Science **324**, 360 (2009).

[71] Kurt Gibble, Phys. Rev. Lett. **103**, 113202 (2009). and references therein.

[72] Chad Fertig and Kurt Gibble, Phys. Rev. Lett. **85**, 1622 (2000).

[73] S. Gupta, Z. Hadzibabic, M. W. Zwierlein, C. A. Stan, K. Dieckmann, C. H. Schunck, E. G. M. van Kempen, B. J. Verhaar, and W. Ketterle, Science **300**, 1723 (2003).

[74] Tomoya Akatsuka, Masao Takamoto, and Hidetoshi Katori, Nature Phys. **4**, 954 (2008).

[75] C. W. Chou, D. B. Hume, J. C. J. Koelemeij, D. J. Wineland, and T. Rosenband, Phys. Rev. Lett. **104**, 070802 (2010).

[76] E. P. Bashkin, Sov. Phys. JETP **3**, 547 (1984).

[77] S. J. J. M. F. Kokkelmans, B. J. Verhaar, K. Gibble, and D. J. Heinzen, Phys. Rev. A **56**, R4389 (1997).

[78] Thomas C. Killian, Dale G. Fried, Lorenz Willmann, David Landhuis, Stephen C. Moss, Thomas J. Greytak, and Daniel Kleppner, Phys. Rev. Lett. **81**, 3807 (1998).

[79] A. C. Maan, H. T. C. Stoof, and B. J. Verhaar, Phys. Rev. A **41**, 2614 (1990).

[80] M. Morrow and A. J. Berlinsky, Can. J. Phys. **61**, 1042 (1983).

[81] S. Vasilyev, J. Järvinen, A. I. Safonov, A. A. Kharitonov, I. I. Lukashevich, and S. Jaakkola, Phys. Rev. Lett. **89**, 153002 (2002).

[82] S. A. Vasiliev, J. Järvinen, A. I. Safonov, and S. Jaakkola, Phys. Rev. A **69**, 023610 (2004).

[83] A. Safonov, I. Safonova, and I. Lukashevich, JETP Letters **87**, 23 (2008).

[84] A. I. Safonov, I. I. Safonova, and I. S. Yasnikov, Phys. Rev. Lett. **104**, 099301 (2010).

[85] B. Yurke, D. Igner, E. Smith, B. Johnson, J. Denker, C. Hammel, D. Lee, and J. Freed, J. Phys. Colloq. **41**, C7 177 (1980).

[86] I. Svare and G. Seidel, Phys. Rev. **134**, A172 (1964).

[87] N. Bloembergen, E. M. Purcell, and R. V. Pound, Phys. Rev. **73**, 679 (1948).

[88] G. W. Parker, Am. J. Phys. **38**, 1432 (1970).

[89] G. Van Gorp and A. Stesmans, Phys. Rev. B **45**, 4344 (1992).

[90] J. H. Van Vleck, Phys. Rev. **74**, 1168 (1948).

[91] C. P. Slichter, *Principles of Magnetic Resonance* (Springer-Verlag, 1990).

[92] G. W. Canters and C. S. Johnson, J. Mag. Res. **6**, 1 (1972).

[93] D. A. Drabold and P. A. Fedders, Phys. Rev. B **37**, 3440 (1988).

[94] F. J. Adrian, J. Chem. Phys. **32**, 972 (1960).

[95] M. E. Hayden and W. N. Hardy, J. Low Temp. Phys. **99**, 787 (1995).

[96] L. Pollack, S. Buchman, and T. J. Greytak, Phys. Rev. B **45**, 2993 (1992).

[97] M. Morrow and W. N. Hardy, Can. J. Phys. **61**, 956 (1983).

[98] W. N. Hardy, M. D. Hürlimann, and R. W. Cline, Japan. J. Appl. Phys. **26S3**, 2065 (1987).

[99] L. Pollack, S. Buchman, Y. M. Xiao, H. F. Hess, G. P. Kochanski, and T. J. Greytak, Phys. Rev. B **34**, 461 (1986).

[100] J. Järvinen, Studies of two-dimensional atomic hydrogen gas with electron-spin resonance, Ph.D. thesis, University of Turku (2006).

[101] S. A. Vasiliev, E. Tjukanoff, M. Mertig, A. Ya. Katunin, and S. Jaakkola, Europhys. Lett. **24**, 223 (1993).

[102] V. Ivanov, L. Mazzola, O. Vainio, S. Vasiliev, and K.-A. Suominen. University of Turku, unpublished (2010).

[103] Kaden R. A. Hazzard and Erich J. Mueller, Phys. Rev. Lett. **101**, 165301 (2008).

[104] A. Safonov, I. Safonova, and I. Yasnikov, JETP Letters **90**, 8 (2009).

[105] B. Yurke, Experiments on spin polarized quantum fluids, Ph.D. thesis, Cornell University (1983).

[106] Craig T. Van Degrift, Rev. Sci. Instrum. **46**, 599 (1975).

[107] M. Iino, M. Suzuki, and A. J. Ikushima, J. Low Temp. Phys. **61**, 155 (1985).

[108] D. K. Cheng, *Fundamentals of Engineering Electromagnetics* (Addison-Wesley, 1993).

[109] B. R. Johnson, J. S. Denker, N. Bigelow, L. P. Lévy, J. H. Freed, and D. M. Lee, Phys. Rev. Lett. **52**, 1508 (1984).

[110] O. Vainio, S. Novotny, and S. Vasiliev. University of Turku, unpublished (2010).

[111] J. de Boer, Physica **14**, 139 (1948).

[112] J. H. Hetherington, Phys. Rev. **176**, 231 (1968).

[113] R. A. Guyer, R. C. Richardson, and L. I. Zane, Rev. Mod. Phys. **43**, 532 (1971).

[114] G. V. Chester, Phys. Rev. A **2**, 256 (1970).

[115] A. J. Leggett, Phys. Rev. Lett. **25**, 1543 (1970).

[116] R. A. Guyer, Phys. Rev. Lett. **26**, 174 (1971).

[117] E. Kim and M. H. W. Chan, Nature **427**, 225 (2004).

[118] E. Kim and M. H. W. Chan, Science **305**, 1941 (2004).

[119] James Day and John Beamish, Nature **450**, 853 (2007).

[120] X. Lin, A. C. Clark, and M. H. W. Chan, Nature **449**, 1025 (2007).

[121] B. Hunt, E. Pratt, V. Gadagkar, M. Yamashita, A. V. Balatsky, and J. C. Davis, Science **324**, 632 (2009).

[122] John D. Reppy, Phys. Rev. Lett. **104**, 255301 (2010).

[123] Mark W. Meisel, Physica B **178**, 121 (1992).

[124] Nikolay Prokof'ev, Adv. Phys. **56**, 381 (2007).

[125] Sebastien Balibar, Nature **464**, 176 (2010).

[126] H. Meyer, Can. J. Phys. **65**, 1453 (1987).

[127] A. C. Clark, X. Lin, and M. H. W. Chan, Phys. Rev. Lett. **97**, 245301 (2006).

[128] A. Clark, Z. Cheng, M. Bowne, X. Lin, and M. Chan, J. Low Temp. Phys. **158**, 867 (2010).

[129] Francesco Operetto and Francesco Pederiva, Phys. Rev. B **75**, 064201 (2007).

[130] Fabio Mezzacapo and Massimo Boninsegni, Phys. Rev. A **75**, 033201 (2007).

[131] Long Dang, Massimo Boninsegni, and Lode Pollet, Phys. Rev. B **79**, 214529 (2009).

[132] A. Ya. Katunin, I. I. Lukashevich, S. T. Orozmamatov, V. V. Sklyarevskii, V. V. Suraev, V. V. Filippov, N. I. Filippov, and V. A. Shevtsov, JETP Lett. **34**, 357 (1981).

[133] Kaden R. A. Hazzard and Erich J. Mueller, Phys. Rev. B **82**, 014303 (2010).

[134] R. L. Danilowicz and R. D. Etters, Phys. Rev. B **19**, 2321 (1979).

[135] Daohui Li and Gregory A. Voth, J. Chem. Phys. **100**, 1785 (1994).

[136] Gilbert N. Lewis and David Lipkin, J. Am. Chem. Soc. **64**, 2801 (1942).

[137] E. Whittle, D. A. Dows, and G. C. Pimentel, J. Chem. Phys. **22**, 1943 (1954).

[138] S. N. Foner, E. L. Cochran, V. A. Bowers, and C. K. Jen, J. Chem. Phys. **32**, 963 (1960).

[139] Mark Sharnoff and R. V. Pound, Phys. Rev. **132**, 1003 (1963).

[140] R. K. Leach, A paramagnetic resonance study of hydrogen atom production and recombination in solid H_2 from 1.4 to 8 K, Ph.D. thesis, University of Wisconsin (1972).

[141] Bryan Palaszewski, AIAA Journal 1998-3736 (1998).

[142] Bryan Palaszewski, AIAA Journal 2000-3855 (2000).

[143] A. V. Ivliev, A. Ya. Katunin, I. I. Lukashevich, V. V. Sklyarevskii, V. V. Suraev, V. V. Filippov, N. I. Filippov, and V. A. Shevtsov, Sov. Phys. JETP **62**, 1268 (1985).

[144] Tetsuo Miyazaki, Nobuchika Iwata, Kwang Pill Lee, and Kenji Fueki, J. Phys. Chem. **93**, 3352 (1989).

[145] T. Kumada, M. Sakakibara, T. Nagasaka, H. Fukuta, J. Kumagai, and T. Miyazaki, J. Chem. Phys. **116**, 1109 (2002).

[146] Yu. Kagan, L. A. Maksimov, and N. V. Prokof'ev, JETP Lett. **36**, 253 (1982).

[147] E. B. Gordon, A. A. Pel'menev, O. F. Pugachev, and V. V. Khmelenko, JETP Lett. **37**, 282 (1983).

[148] Haruyuki Tsuruta, Tetsuo Miyazaki, Kenji Fueki, and Naoto Azuma, J. Phys. Chem. **87**, 5422 (1983).

[149] Tetsuo Miyazaki and Kwang Pill Lee, J. Phys. Chem. **90**, 400 (1986).

[150] Takayuki Kumada, Phys. Rev. B **68**, 052301 (2003).

[151] A. V. Ivliev, A. S. Iskovskikh, A. Ya. Katunin, I. I. Lukashevich, V. V. Sklyarevskii, V. V. Suraev, V. V. Filippov, N. I. Filippov, and V. A. Shevtsov, JETP Lett. **38**, 379 (1983).

[152] J. H. Constable, J. R. Gaines, P. E. Sokol, and P. C. Souers, J. Low Temp. Phys. **58**, 467 (1985).

[153] G. W. Collins, J. L. Maienschein, E. R. Mapoles, R. T. Tsugawa, E. M. Fearon, P. C. Souers, J. R. Gaines, and P. A. Fedders, Phys. Rev. B **48**, 12620 (1993).

[154] R. W. H. Webeler, J. Chem. Phys. **64**, 2253 (1976).

[155] Gerald Rosen, J. Chem. Phys. **65**, 1735 (1976).

[156] F. J. Zeleznik, J. Chem. Phys. **65**, 4492 (1976).

[157] G. Rosen and R. W. H. Webeler, Lett. Nuovo Cimento **26**, 579 (1979).

[158] G. W. Collins, E. M. Fearon, J. L. Maienschein, E. R. Mapoles, R. T. Tsugawa, P. C. Souers, and J. R. Gaines, Phys. Rev. Lett. **65**, 444 (1990).

[159] Yu. Kagan and N. V. Prokof'ev, *Quantum Tunnelling Diffusion in Solids*, in *Quantum tunnelling in condensed media*, edited by Yu. Kagan and A. J. Leggett (North-Holland, Amsterdam, 1992), vol. 34, pp. 37–143.

[160] V. A. Mikheev, V. A. Maidanov, and N. P. Mikhin, Solid State Commun. **48**, 361 (1983).

[161] V. Shevtsov, A. Frolov, I. Lukashevich, E. Ylinen, P. Malmi, and M. Punkkinen, J. Low. Temp. Phys. **95**, 815 (1994).

[162] T. Kumada, S. Mori, T. Nagasaka, J. Kumagai, and T. Miyazaki, J. Low. Temp. Phys. **122**, 265 (2001).

[163] V. V. Khmelenko, E. P. Bernard, S. A. Vasiliev, and D. M. Lee, Russian Chemical Reviews **76**, 1107 (2007).

[164] T. Miyazaki, *Atom Tunneling Reactions in Quantum Solid Hydrogen*, Atom Tunneling Phenomena in Physics, Chemistry and Biology, edited by T. Miyazaki (Springer-Verlag, Berlin, 2004).

[165] L. H. Piette, R. C. Rempel, H. E. Weaver, and J. M. Flournoy, J. Chem. Phys. **30**, 1623 (1959).

[166] J. L. Hall and R. T. Schumacher, Phys. Rev. **127**, 1892 (1962).

[167] Toni Kiljunen, Jussi Eloranta, and Henrik Kunttu, J. Chem. Phys. **110**, 11814 (1999).

[168] E. P. Bernard, R. E. Boltnev, V. V. Khmelenko, V. Kiryukhin, S. I. Kiselev, and D. M. Lee, Phys. Rev. B **69**, 104201 (2004).

[169] A. S. Iskovskikh, A. Ya. Katunin, I. I. Lukashevich, V. V. Sklyarevskii, and V. A. Shevtsov, JETP Lett. **42**, 30 (1985).

[170] A. V. Ivliev, A. Ya. Katunin, I. I. Lukashevich, V. V. Sklyarevskii, V. V. Suraev, V. V. Filippov, N. I. Filippov, and V. A. Shevtsov, JETP Lett. **36**, 472 (1982).

[171] J. Järvinen, V. V. Khmelenko, D. M. Lee, J. Ahokas, and S. Vasiliev, J. Low Temp. Phys., to be published (2010).

[172] P. C. Souers, *Hydrogen Properties for Fusion Energy* (University of California Press, Berkley, CA., 1986).

[173] S. B. Crampton, J. J. Krupczak, and S. P. Souza, Phys. Rev. B **25**, 4383 (1982).